Development of robust modelling methods for a quick evaluation of biomass pyrolysis performance and its transient behaviour at a particle level

Teresa Martí Rosselló

University of Strathclyde
Department of Chemical and Process Engineering

Submitted for the degree of Doctor of Philosophy
December 2019

Declaration

This thesis is the result of the authors original research. It has been composed by the author and has not been previously submitted for examination which has led to the award of a degree.

Teresa Martí Rosselló
Glasgow, December 2019

Acknowledgements

I would like to express my sincere gratitude to my thesis supervisors Dr Jun Li and Dr Leo Lue.

I would also like to thank my family, specially my mother, as well as my partner, friends and colleagues for their support.

Abstract

Biomass is organic matter that can be used as an energy resource by means of conversion technologies, such as pyrolysis. To assess pyrolysis performance of various biomass materials under different operating conditions and improve the process efficiency of biomass pyrolysis, the development of accurate, fast and robust modelling methods is desirable. The main objective of this thesis is to develop and assess modelling methods to obtain a deeper insight into the physico-chemical processes affecting a biomass subjected to pyrolysis, more specifically its (1) kinetics, and (2) mass and (3) heat transfer at a particle level. The kinetics of biomass pyrolysis have been studied for biomass in the thermally thin regime, and a novel method to obtain the kinetics parameters has been developed. This method can successfully provide a rapid and accurate estimation of the relative contributions of cellulose, hemicellulose, and lignin to the volatile yield, as well as their kinetic parameters. The method offers a simple way to obtain the kinetics parameters directly from thermogravimetric data and saves computing time by providing sensible initial values and bounds to the parameters. Wheat straw pellets have been used to study biomass pyrolysis in the thermally thick regime. The heat and mass transfer mechanisms that take place inside the pellet during pyrolysis have been analized using a single particle model. As a result, the changes inside a biomass pellet can be predicted at any given inner position and time during pyrolysis, and the inner gradients can be observed. It is concluded that the inner temperature distribution of the pellet depends mainly on the properties of the solid phase, but the final product distribution is also linked to the flux of the vapour phase, due to potential additional pyrolysis reactions that could take place if the volatiles generated are not quickly removed from the particle. All the models implemented are validated against experimental data.

Publications

- Martí-Rosselló, T., Li, J., Lue, L., Karlström, O., and Brink, A. (In preparation). "Single particle model of the pyrolysis of a wheat straw pellet".
- Martí-Rosselló, T., Li, J., Lue, L., Karlström, O., and Brink, A. (Accepted/In press). "Heat transfer behaviour of a wheat straw pellet undergoing pyrolysis". Paper presented at ICAE2019: The 11th International Conference on Applied Energy, Västerås, Sweden.
- Martí-Rosselló, T., Li, J., and Lue, L. (2018). "Quantitatively modelling kinetics through a visual analysis of the derivative thermogravimetric curves: application to biomass pyrolysis". *Energy Conversion and Management*, 172, 296-305.
- Martí Rosselló, T., Li, J., and Lue, L. (2016). "Kinetic models for biomass pyrolysis". *Archives of Industrial Biotechnology*, 1(1), 4-7.

<u>Contributions</u>

- Martí-Rosselló, T., Li, J., and Lue, L. (2017). "Kinetic analysis of biomass pyrolysis with a peak temperature method". Poster session presented at The 25th European Biomass Conference and Exhibition, Stockholm, Sweden.
- Cao, W., Martí-Rosselló, T., Li, J., and Lue, L. (2019). "Prediction of potassium compounds released from biomass during combustion". *Applied Energy*, 250, 1696-1705.
- Cao, W., Li, J., Martí-Rosselló, T., and Zhang, X. (2018). "Experimental study on the ignition characteristics of cellulose, hemicellulose, lignin and their mixtures". *Journal of the Energy Institute*, 92(5), 1303-1312.

Nomenclature

Symbols

α	extent of conversion
α_T	thermal diffusivity, m^2 s^{-1}
β	heating rate
ϵ	emissivity
κ	permeability, m^2
μ	dynamic viscosity, Pa s
$\nu_{r,i}$	stoichiometry of the species i in the reaction r
ψ	test function
ρ	density, kg m^{-3}
σ	Stefan-Boltzmann constant, W m^{-2} K^{-}4
σ_w	sigma related to width, K
τ	dimensionless time
τ^*	time constant in analytical solution
τ_{SUPG}	stabilization parameter
τ_{asy}	asymmetry parameter
θ	height fraction
ε	porosity
ξ_r	extent of reaction, kg

Letters

A	pre-exponential factor, s^{-1}
CL	characteristic length, m
C_p	heat capacity, J kg^{-1} K^{-1}

D	diffusivity, $\mathrm{m^2\,s^{-1}}$
E	activation energy, $\mathrm{J\,mol^{-1}}$
P	pressure, Pa
P_{atm}	atmospheric pressure
R	gas constant, $\mathrm{J\,mol^{-1}\,K^{-1}}$
T	temperature, K
T_E	activation energy temperature, K
T_∞	reactor temperature, K
T_p	peak temperature, K
ΔH_r	heat of reaction, $\mathrm{J\,kg^{-1}}$
λ	thermal conductivity, $\mathrm{W\,m^{-1}\,K^{-1}}$
$\mathbf{u}$	velocity, $\mathrm{m\,s^{-1}}$
$\mathbf{v}_{N_2}$	carrier gas velocity, $\mathrm{m\,s^{-1}}$
d_{pore}	pore diameter, m
d_p	particle diameter, m
$f(\rho)$	reaction model
h	heat transfer coefficient, $\mathrm{W\,m^{-2}\,K^{-1}}$
k	rate constant, $\mathrm{s^{-1}}$
n	reaction order
x_i	fraction of the component i
CELL	cellulose
DAEM	distributed activated energy model
DTG	derivative thermogravimetry
EGH	exponential-Gaussian hybrid
FC	fixed carbon
FEM	finite element method
FWHM	full width at half maximum
H	height of the peak
HCE	hemicellulose
HHV	higher heating value, $\mathrm{MJ\,kg^{-1}}$
HR	heating rate
L	particle length
MW	molecular weight, $\mathrm{kg\,mol^{-1}}$
RMS	root mean square

SPM	Single Particle Model
SUPG	Streamline-upwind Petrov/Galerkin
TG	thermogravimetric
TGA	thermogravimetric analysis
VM	volatile matter
W_+	width to the right, K
W_-	width to the left, K
lignin	lignin
r	reaction

Subscripts

∞	surrounding condition
0	initial condition
B	biomass (wheat+activated wheat)
C	char
G	gas
T	tar
adv	advection
i	species in the solids or volatiles
p	peak
r	reaction
s	solids (biomass+char)
trans	transient
v,V	vapour, volatiles (gas+tar)

Contents

List of Tables

List of Figures

Chapter 1

Introduction

Nowadays, the use of fossil fuels raises global concerns because they negatively impact the environment and are a non-renewable resource [1], which means that we cannot keep relying on them indefinitely. It is because of the aforementioned reasons that there is a growing trend towards the use of renewable fuels [2]. However, it is believed that securing renewable fuel substitutes to the current uses of fossil fuels is not so easy in the near term [1], which justifies intensive research on improving the technologies related to renewable energy.

Biomass is organic matter that can be used as a material and energy resource [3]. It has stored solar energy through the process of photosynthesis [3], and the stored energy can be later utilized via various conversion technologies [4]. A conversion technology is a type of treatment that is applied to biomass in order to obtain other useful products. The most basic conversion technology to obtain energy from biomass is combustion, but other more advanced conversion technologies to transform biomass are also available, and research in these technologies is necessary to achieve a highest degree of process efficiency and sustainability [5].

Biomass pyrolysis is potentially one of the cheapest routes towards renewable liquid fuels [6]. It is a promising application at a small scale and at an industrial scale, although the number of commercial pyrolysis plants at an industrial scale is currently still limited. The commercialisation of biomass pyrolysis technology is a multi-scale challenge [6], from the quality and availability of feedstock and the efficiency of the process, to the final use of the energy products generated.

Experiments and mathematical models can be used to study the process of biomass pyrolysis, and both are necessary. Experiments allow to study the process for given materials and operating conditions, and a model, validated with experimental data, can predict the pyrolysis behaviour for a range of materials and operating conditions without the need to perform experiments for all scenarios, which would be time-consuming and also expensive. A model can also help in optimizing the operating conditions for the desired products, which would save time and reduce costs.

Pyrolysis kinetic models describe how the reactions proceed with respect to temperature or time, but when biomass is in the form of a large particle, the heat and mass transfer phenomena in the particle need to be taken into account, and the spatial dimension becomes relevant. Figure 1.1 shows the type of possible modelling approaches to study the process of biomass pyrolysis. The models in the upper levels include the models in the lower levels in some

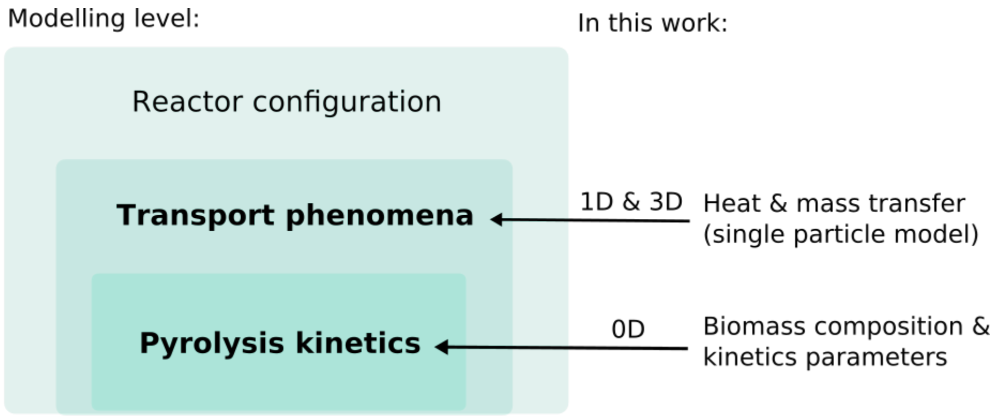

Figure 1.1: Context of the pyrolysis models developed/applied in this work.

way, even if it is just by making a simplification assumption, although each individual model can be very complex on its own. The pyrolysis kinetics models are always zero-dimensional and refer to the reaction mechanism. Biomass characterization is not specific for pyrolysis, but the biomass properties are required in all pyrolysis models. The pyrolysis kinetics can be coupled with a model that includes transport phenomena, like a single particle model, which renders the changes in temperature and mass across the biomass particle, and depending on the level of detail required it can be one, two or three-dimensional. The one-dimensional model renders changes only along one direction inside the particle, therefore it is used with the assumption of a symmetric particle such as an sphere or an infinite cylinder, a two-dimensional model allows changes across two axis inside the particle, reducing the required symmetry level of the particle, and finally a three-dimensional model is compatible for any given particle shape. In the diagram there is also a model for reactor configuration, which could combine multiple single particle models to see how biomass particles interact amongst them, or lump all biomass particles as a continuous solid and see how it changes in a given reactor set up.

Another possible model that would encompass all the previously mentioned, is a supply chain model. This model is not so focused on the process of pyrolysis itself, but on the overall life cycle, including the harvesting and biomass collection, pre-processing, storage and transportation, and making sure that the process is cost-effective and taking into account the environmental impacts [7].

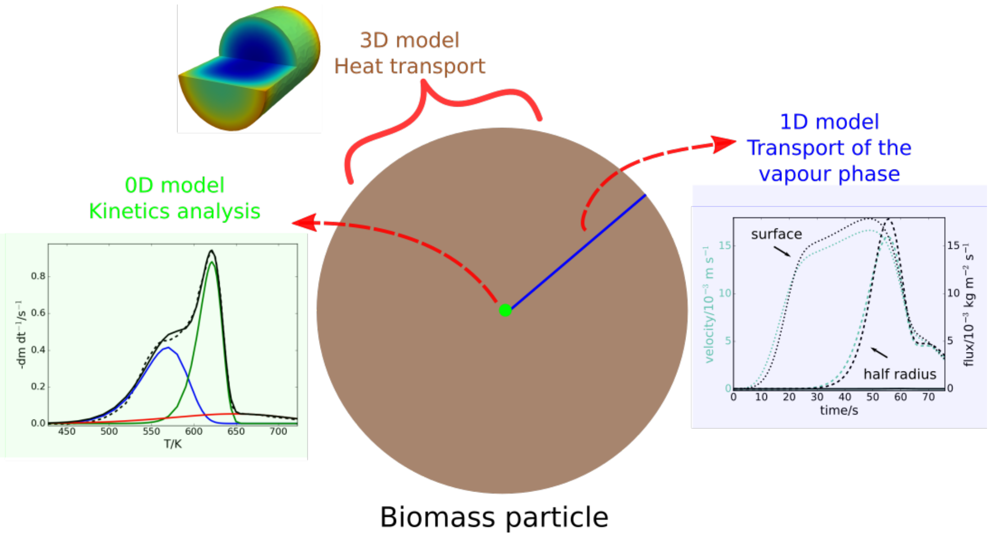

Figure 1.2: Biomass particle with the scope of the contributions of this work.

The overall purpose of this work is to contribute to the field of renewable energy, focusing on the process of biomass pyrolysis, which is generally used to obtain energy and chemicals from biomass. The specific contributions of this work are illustrated schematically in Fig. 1.2. The zero-dimensional model describes pyrolysis at a kinetics level and the spatial dimensions of the biomass particle are irrelevant, since the particle is assumed to be very small. In this work a novel analytical method to determine the biomass composition and pyrolysis kinetics from experimental data of biomass pyrolysis is developed to simplify and reduce the fitting time with respect to traditional fitting methods. In pyrolysis reactors, biomass is typically ground/shredded but the particles are not fine and they can have diverse sizes and shapes. At the particle level, the potential impact of the shape and size of the biomass particle on the pyrolysis performance is taken into account with a one-dimensional and a three-dimensional single particle models. In this work a one-dimensional model, assuming a spherical particle shape, has been used to study the pyrolysis of a wheat straw pellet, more specifically the process of volatiles transport inside the particle and other processes relevant to biomass pyrolysis. A three-dimensional model with a cylindrical shape, closer to the shape of a biomass pellet, has been used to also study the pyrolysis of a wheat straw pellet but with special emphasis on the heat distribution in the pellet, along with other relevant pyrolysis processes.

The remainder of this thesis is structured as follows. Chapter 2 reviews the concepts of biomass, the process of pyrolysis, and the most common experimental and mathematical techniques used to study biomass pyrolysis. In Chapter 3 the kinetics are studied with thermogravimetric analysis at a thermally thin regime and an analytical method for its determination is developed. This method is different from the previous ones in that it is based on observable properties and gives information about the meaning of kinetic parameters. The objective addressed in Chapters 4, 5, 6, and 7 is to understand which are the influencing parameters in heat and mass transfer processes across a biomass particle, because the transport processes are key in the determination of the properties and quality of the pyrolysis products. To that end, biomass pyrolysis is studied at a thermally thick regime, the influence of the transport processes that take place inside the biomass particle are taken into account and studied with a single particle model. Chapter 4 explains the experimental procedure and the results of the pyrolysis of a biomass single particle, in this case in the form of a wheat straw pellet. It also serves as the basis for comparison with the single particle model developed and implemented in the remaining of this thesis. Chapter 5 presents the governing equations of the single particle model, as well as a dimensional analysis and a model validation. Chapter 6 presents the one-dimensional model results and Chapter 7 presents the three-dimensional model results. Finally, Chapter 8 summarizes the main findings from each chapter and the thesis overall conclusions.

Chapter 2

Review

The concepts of biomass and pyrolysis are fundamental in this thesis, for that reason in this chapter the necessary background related to them is given. First, biomass is described in detail, including its main defining characteristics and common uses. Then the process of pyrolysis and its operating conditions are explained, along with the potential products of biomass pyrolysis. Finally, thermogravimetric analysis, which is the most common method of experimentally studying biomass pyrolysis, is explained, along with the mathematical expression that is typically used to reproduce the thermogravimetric results, as well as to model pyrolysis and make predictions.

2.1 Biomass

Biomass is organic material derived in its major part from plants, although it could come from any recently living organism. In this work when biomass is mentioned, it will refer to biomass derived from plants. This resource can be readily available, but the growth and harvest cycles of biomass should be sustainably managed to avoid consuming it too quickly before it has time to regrow. It is considered a renewable resource, because once harvested it can be replaced with new growth at a human time-scale [8], as opposed to fossil fuels that take millions of years [9]. It is also generally presumed to be a carbon neutral fuel, the assumption made to exclude the carbon emissions is that the amount of carbon dioxide released during combustion is the same amount that was absorbed by the plant, and therefore the net carbon emissions are zero [10]. The carbon neutrality assumption however, might not always be true, because in the calculation of the carbon footprint from biomass utilization for energy, the impact of deforestation, the change of land-use and the carbon emissions derived from biomass combustion are not always included [10]. Nevertheless, it is true that the carbon dioxide released from a biomass conversion treatment, could potentially be absorbed again by a new plant, that is why a sustainable growing and harvesting of biomass is essential, along with the exploitation of residual biomass from food crops or waste biomass from construction.

2.1.1 Utilization

According to a report from the Food and Agriculture Organization of the United Nations (FAO) on access to fuel, currently near 3 billion people rely on traditional biomass as the main energy source for heat and cooking, using wood, charcoal or animal waste as a fuel [11]. Traditional biomass, also known as 'traditional biomass energy use', makes reference to the direct combustion of biomass in open fires and cooking ovens. It is mainly used in rural areas of developing countries, and it is often performed in very inefficient ways, which might lead to health problems and to an unsustainable collection of wood [12].

The use of traditional biomass might carry environmental and health risks [11][5]. Biomass combustion emissions can be generated from households and industry. The emissions released indoors are especially detrimental to the human health due to the high concentration of pollutants in an enclosed space, and the emissions released outdoors apart from having an impact on the human health, also affect the environment contributing to the greenhouse effect [5]. The most toxic pollutant from biomass combustion on the human health is the particulate matter which can affect the respiratory system [13], other toxic pollutants are hydrocarbons, carbon monoxide and nitrogen dioxide [13]. The modern technologies of biomass conversion strive to increase sustainability and efficiency [14].

In relation to the global energy consumption in 2016, 18.2% was from renewable energy, complemented with 79.5% from fossil fuels, and 2.2% from nuclear energy [12]. This 18.2% of renewable energy is build up with 7.8% of traditional biomass and 10.4% of modern renewables. The modern renewables are formed by wind, solar, geothermal, ocean power, hydropower and biomass. The biomass included in modern renewables makes reference to the use of modern biomass technologies excluding the traditional biomass use, however, it could also include the controlled combustion in reactors. In 2016, biomass from modern renewables contributed with 5% of the total energy consumption, which was used towards heating in industry, heating in buildings, electricity and transport [12].

The degree of efficiency of a given conversion technology influences the degree of efficiency of producing energy from biomass. A summary of the main conversion technologies for biomass is given later in Section 2.1.4. But efficiency not only depends on the conversion technology, it also depends on other aspects related to the supply chain [15]. For instance, the high moisture content of biomass might cause self-degradation during storage, with the added risk of self-ignition due to an increase in temperature caused by the activity of microorganisms [16], and the low bulk density of biomass means that it will occupy a great deal of space in the transportation trucks and in storage facilities, translating also into an increased cost [17]. The seasonality of biomass might make it difficult to use just a few types of biomass, therefore the conversion facilities should be able to cope with the variation of the feedstock type [18]. Also due to the seasonal characteristic of biomass, large storage capacities might be required to ensure a continuous feedstock flow in conversion plants [19]. The costs of biomass conversion might also increase if the costs of biomass collection from spatially scattered and remote areas are included [20].

2.1.2 Types of biomass

Biomass contains edible and non-edible components. The major non-edible component from biomass is lignocellulose, which consists of cellulose, hemicellulose and lignin [21], these components will be explained in detail in next section. Biomass with high levels of lignocellulose is preferred for material and energy feedstock, and biomass with high content of edible components such as oils, proteins, carbohydrates and sugar [22] is preferred for food.

Some species of herbaceous biomass and trees are preferred for energy conversion due to their high content of lignocellulose, these are called energy crops and energy forestry, respectively. Energy crops are specifically grown for fuel, they are perennial so they do not need to be replanted every year, they give more biomass output per hectare than regular crops, and they could also use soil of poorer quality, because they have a lower need of nutrients and water [23], which is beneficial to avoid competition for the use of land with food crops. Examples of energy crops are switchgrass, miscanthus, sweet sorghum and wheat grass [23]. Energy forestry (or woody energy) has similar advantages as energy crops, in addition of no need for fertilizers or pesticides [23]. Examples of energy forestry are poplar, willow and eucalyptus [23]. The aim of this work is to study the process of pyrolysis to obtain useful products from biomass, like chemicals and energy, therefore lignocellulosic biomass is preferred.

When biomass is grown and harvested from the fields, their removal from the soil should ideally be compensated with new biomass growth, to avoid deforestation and to help absorb carbon dioxide from the atmosphere, but in terms of time scales, it is much quicker to harvest a plant than to plant and grow it. It is essential then, to have a sustainable crop/forest management, that is why plants of rapid growth like energy crops are attractive in that respect. Another aspect to take into account is the nutrient depletion of the soil in the long term if the nutrients are not replaced with appropriate soil management techniques. Indeed, the sustainability of the use of biomass as fuel is critical, and a life cycle assessment of the process is indispensable [21].

Organic waste from construction, industry and households could also be used as a feedstock for conversion to energy. This would contribute to a good residue management, and it would help to avoid biomass over-harvesting, which means taking more biomass than what can be replaced in the short term. In the case of organic waste coming from households, also called municipal solid waste, it would be difficult to control the pyrolysis conversion process, because this type of biomass does not necessarily have a major content of lignocellulose, its composition keeps changing depending on the consumption trends of the households, and it might have a high content of moisture. Instead, solid municipal waste is usually processed with biological treatments [24]. Wood residues from construction or forestry, crop residues from agriculture or lignocellulosic residues from other industries could still be used with the majority of biomass conversion technologies.

2.1.3 Composition

Biomass can be characterized in terms of its major chemical components (cellulose, hemicellulose and lignin), its elemental composition (ultimate analysis), and its products when heated under specific conditions (proximate analysis).

The relative proportion of the main chemical components of biomass varies across the different types of biomass. According to herbaceous [25] and wood samples [26] analysed, biomass generally consists of cellulose (30-50%), hemicellulose (20-30%) and lignin (10-20%), with a remaining content of extractives (proteins, acids, etc.) and inorganic compounds (10-30%). Hemicellulose is a branched polymer usually represented by the molecule xylan ($C_5H_8O_4$). It should also be noted that the structure of hemicellulose could significantly vary in different types of biomass [27]. Cellulose is the most abundant organic compound on Earth, and it can be represented as an unbranched polymer of glucose ($C_6H_{10}O_5$) [27]. Lignin is an amorphous and complex polymer, which does not have a general chemical formulation to represent it. In some studies it is represented as $C_{11}H_{12}O_4$, or as a combination of different types of lignin: hydrogen-rich lignin ($C_{22}H_{28}O_9$), oxygen-rich lignin ($C_{20}H_{22}O_{10}$) and carbon-rich lignin ($C_{15}H_{14}O_4$) [28] [29]. Faravelli et al. [29] related the biomass content of hydrogen and carbon to the corresponding relative composition of hydrogen-rich lignin, oxygen-rich lignin and carbon-rich lignin. Figure 2.1 shows the chemical structures of each component as reported in the literature. The experimental determination of the biomass chemical composition can be done by a diversity of conventional methods of chemical analysis; Some of the most used procedures are the TAPPI, NREL and SCAN methods [30]. The experimental extraction mechanisms have the risk of interfering with the sample during the extraction process [31], therefore different methods could lead to different results.

The proximate analysis gives the product composition of a biomass sample that is heated in specific conditions; It characterizes the biomass in terms of its contents of fixed carbon, volatile matter, moisture and ash. Each product is experimentally determined by given standards, except for the fixed carbon that is calculated by difference assuming that the sum with the remaining components is 100%. The fixed carbon is the carbonaceous material that remains after

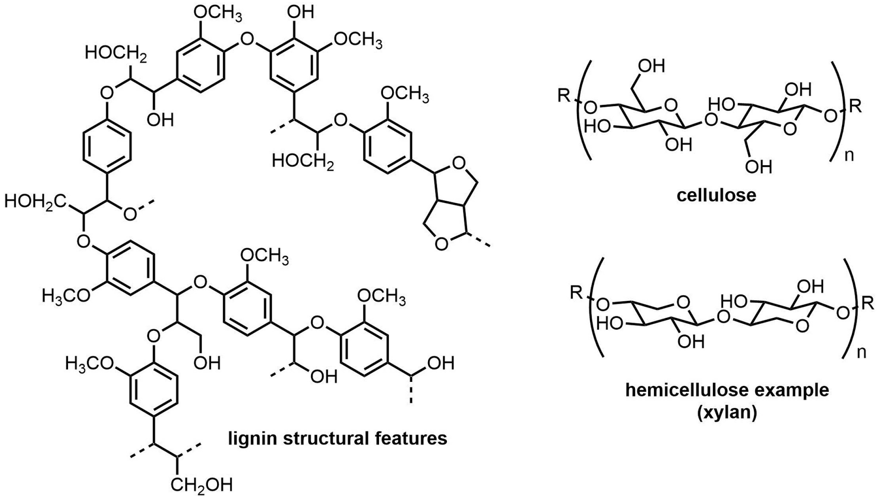

Figure 2.1: Chemical structure of the biomass components, from [32] as in [33]

all the volatile matter has been released after heating the biomass, without including ash, and ash is the inorganic components in biomass such as alkali metals. A collection of the standard methods used can be found in the literature [27]. The composition can be given in 'as received' basis, 'dry' basis, and 'dry ash-free' basis. The 'dry ash-free' basis consists of the sum of all the organic elements, the 'dry' basis consists of the sum of the organic elements and ash, and the 'as received' basis consists of the sum of the organic elements, ash and moisture. Common 'as received' values for the proximate analysis of lignocellulosic biomass, taking into account the results of the proximate analysis from multiple biomass samples [34], are about 5-10% moisture, less than 5% of ash, 10-20% fixed carbon, and 70-80% of volatile content.

The elemental composition estimates the amount of carbon, hydrogen and oxygen, other possible elements that could be included in the analysis are nitrogen, sulphur and chlorine. The elemental composition of biomass is determined by the ultimate analysis. A summary of the experimental standards used in this analysis can be found in the literature [27]. Each element is experimentally determined except for oxygen, which is calculated by difference. As in the proximate analysis, the results of the ultimate analysis can be given in different basis. The ash and the moisture are the same as in the proximate analysis. A typical elemental composition for woody biomass is 50% carbon, 6% hydrogen and 44% oxygen [35]. The same elemental composition is reported for miscanthus (as an example of herbaceous biomass), obtained as an average from 58 samples from the European Commission database containing the composition of different biomass types [36].

The Van Krevlen diagram is useful to compare different types of biomass in terms of their respective oxygen/carbon and hydrogen/carbon ratios. In Fig. 2.2 an example of such diagram taken from the literature can be found; this diagram compares several types of fossil fuels with biomass. The figure also indicates how the heating value changes according to the elemental ratios. The lower heating value (LHV) of a fuel decreases with increasing oxygen content, but it increases with increasing hydrogen content [37]. The calorific values of the materials in the diagram could be ordered from major calorific value to lower calorific value as anthracite (35-37 MJ kg^{-1}), coal (33-35 MJ kg^{-1}), lignite (26 MJ kg^{-1}), peat (22 MJ kg^{-1}) and biomass (18-19 MJ kg^{-1}) [38]. Anthracite and lignite are types of coal.

The results from the experimental characterization of biomass have been used in empirical correlations to obtain other biomass properties. There are correlations that predict the elemental composition from the proximate analysis [39][40][41], and correlations that predict the heating value of the biomass

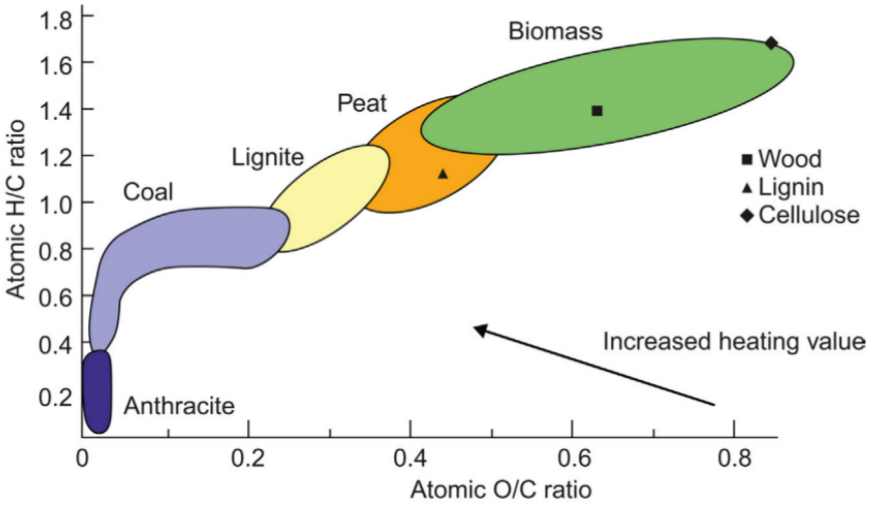

Figure 2.2: Classification of biomass and some fossil fuels according to the Van Krevelen diagram taken from [27].

from the information of the proximate analysis [42] and from the elemental analysis [43]. Some correlations are specific for given heating conditions, like a correlation to predict the product composition for the process of slow pyrolysis from the elemental analysis [44].

2.1.4 Conversion technologies

The available technologies to convert biomass into energy products are diverse and can be catalogued into physical, thermo-chemical and bio-chemical, most of them still being developed and improved to gain in process and cost efficiency. Figure 2.3 is a diagram of the available biomass conversion technologies.

Physical conversion involves only physical changes like drying, grinding (reduction of the particle size) and pelletization, and its final product is a solid fuel which could be burned for energy or used in a subsequent conversion process. Drying and grinding are usually required pretreatments before a thermochemical conversion process to obtain energy [45]. The moisture in the biomass affects the heating process and slows down the thermochemical conversion [46]. Moisture might be beneficial for biological conversion processes, where an increase in moisture translates into an increase in microbial activity [47]. Grinding makes the biomass more manageable, and it also increases the surface area [48], which means that small particles in thermal processes are going to heat more quickly in comparison with large particles [49]. It should be noted that pretreatments are only feasible as long as they still make the overall conversion process cost-efficient [48]. Pelletization is useful when biomass is transported or stored because it increases its bulk density [50].

The biochemical conversion path involves the use of microorganisms to degrade the biomass and digest it, generating other products [51], and as already mentioned, it is recommendable for biomass with a high moisture content, like the municipal solid waste [52]. The process can be aerobic (with the presence of oxygen) or anaerobic (in the absence of oxygen). An example of aerobic conversion is composting, which yields a solid product that can be used as a soil amendment [53]. Anaerobic conversion on the other hand, can yield liquid and gas energy products. Hydrolysis-fermentation and anaerobic digestion are both biochemical conversion processes in the absence of oxygen that yield a liquid energy product and a gas energy product respectively. Anaerobic digestion produces carbon dioxide and methane [27], and its stages are hydrolysis, fermentation, acetogenesis and methanogenesis [54]. Hydrolysis-fermentation

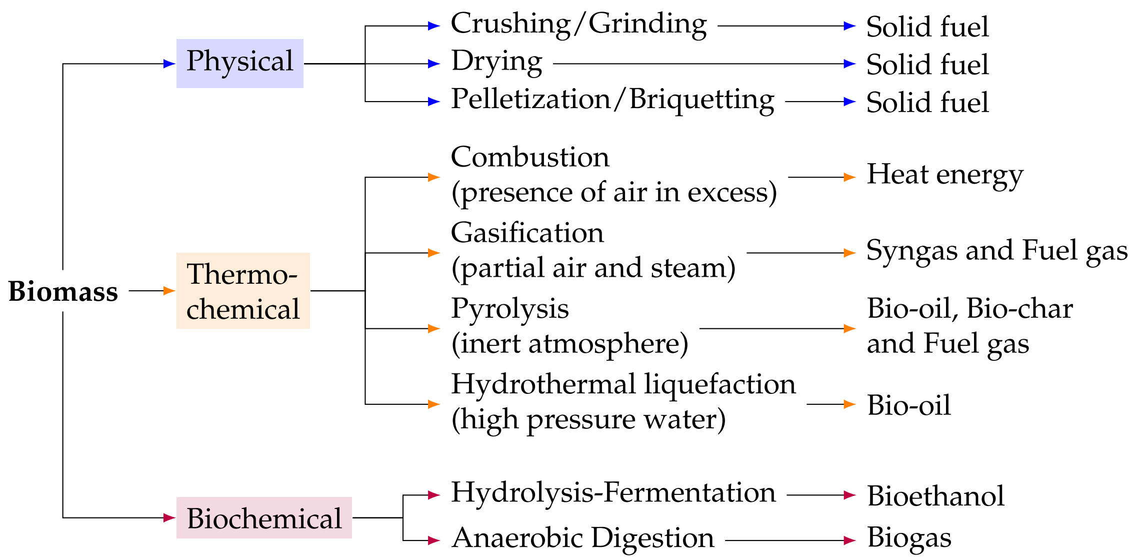

Figure 2.3: Biomass conversion pathways [57].

is similar to the first two steps of anaerobic digestion. In the hydrolysis step, biomass is degraded into sugars using acid or enzymes, and then the sugars are fermented producing ethanol [55]. Fermentation is currently commercially successful only for biomass with high content of edible components, and not for lignocellulosic biomass [27].

The thermochemical route involves the decomposition of the biomass material with the use of increased temperatures. This decomposition can take place in hot pressurized water (hydrothermal liquefaction), yielding bio-oil as a liquid product [56]; In air or in oxygen enriched atmospheres (combustion), generating heat instead of energy products; In an inert atmosphere (pyrolysis), producing solid, liquid and gas products; Or with a semi-oxidative atmosphere and the presence of additives (gasification), which yields a gas product. Pyrolysis is one of the most versatile thermal process because it can be optimized to target the three types of possible products.

2.2 Pyrolysis

Pyrolysis is a thermo-chemical technology that when applied to biomass, a range of products of interest can be obtained. Pyrolysis consists of heating the biomass feedstock in the absence of oxygen in order to obtain solid (char), gas and liquid products (tar, bio-oil), with the products distribution depending on the operating conditions. The next section describes the pyrolysis products, after that, the process of pyrolysis is going to be explained in more detail in relation to its operating conditions and the desired end products, and finally, the common experimental and mathematical methods used to study pyrolysis are introduced.

2.2.1 Products of biomass pyrolysis

The process of biomass pyrolysis is able to yield solid, liquid and gas products. However, the desired product from pyrolysis is usually bio-oil (liquid product), because it is easier to store and transport [58]. Bio-oil consists mostly of a high number of oxygenated compounds and water [59]. It can contain between 15 to 50 wt% water. If the initial biomass feedstock had a maximum of 10 wt% moisture, that would translate into 25 wt% water in the bio-oil, including the water resulting from the pyrolysis reactions [59]. The major compound groups are water, lignin fragments, aldehydes, carboxylic acids, carbohydrates, phenols, furfurals, alcohols and ketones [27]. All pyrolysis products could be directly burned to obtain heat, as the original biomass feedstock, but the advantage of transforming biomass into other products is the possibility to use them in other more valuable ways. Bio-oil could be used to obtain chemicals after a process of extraction, to obtain transportation fuel after a process of upgrading, or it could be used directly in turbines or boilers to produce electricity [58].

Char is the solid material that remains after biomass pyrolysis. The char is made of carbon in its major part, and low contents of hydrogen, oxygen and minerals [60]. The char product could be used as a soil amendment, as activated carbon, in the steel industry, or to produce carbon-based nanomaterials [61]. The characteristics of the resulting char might not be suitable for all the applications mentioned, but for each case, the pyrolysis operating conditions can be adjusted in order to obtain the required char quality. Char can be used as soil amendment but it also behaves as a carbon storage and sequestration material [62], which helps decrease the amount of carbon that is returned to the atmosphere once the biomass is decomposed. When the char has a high level of particle porosity and therefore an increased surface area [63], after a catalytic pre-treatment it can become activated carbon [64], and the activated carbon can be used as a filter to remove pollutants from the water and the air [65], or it could be used for energy storage purposes [66]. Other applications of char from biomass are in the metallurgical industry [67], and as feedstock for carbon-based nanomaterials [68].

The main species in the gas phase are hydrogen and carbon monoxide, with smaller contents of carbon dioxide, water, nitrogen and a range of hydrocarbons [69]. The gas product could be used directly in turbines, engines or boilers to produce electricity, or it could be upgraded via FischerTropsch synthesis to produce transportation fuel [70]. The energy required for pyrolysis could be supplied from burning part of the char/gas/bio-oil products [59]. The percentage of the produced energy that would be necessary to keep the pyrolysis plant working might depend on the scale of the plant [69].

2.2.2 Physico-chemical processes in pyrolysis

The main process during biomass pyrolysis is the chemical transformation of biomass into other products through decomposition. The chemical reactions in pyrolysis become active when there is enough temperature, hence the biomass heating has a direct impact on how pyrolysis progresses. Figure 2.4 is a diagram of the possible physico-chemical processes in pyrolysis. The chemical reactions transform the raw biomass into other materials (pyrolysis products). The heat transfer takes place when the biomass particles receive heat from the reactor environment, first the surface of the particle is heated and then the heat travels across the particle towards its center. The mechanisms of surface heating are thermal convection and thermal radiation, and the mechanism to transfer heat across the particle is by thermal conduction [71]. There is a fourth heating mechanism which is the enthalpy of reaction [71]. The pyrolysis reaction might take heat from the particle or generate heat to the particle depending on their characteristic enthalpy of reaction.

Apart from the chemical reactions and the heat transfer, the process of mass transfer could also take place during pyrolysis. When biomass decomposes, it releases volatiles, which are in a vapour state and can move across the solid biomass particle until they are released through the particle surface. The mechanisms of mass transfer are mass diffusion, when the volatiles generated move through the particle pores, and mass advection, when the volatiles are released from the particle through the particle surface [71]. When the particles are very small, the most dominant process is the chemical reactions (kinetics) [72], but when the particle increases in size, the heat transfer and the mass transfer can influence the pyrolysis performance. The influence of the particle size on pyrolysis is reviewed later in Section 2.2.3. In a pyrolysis model, the kinetics is the only process that always has to be included, the heat and the mass transfer might be more or less significant depending on the pyrolysis operating conditions and biomass characteristics.

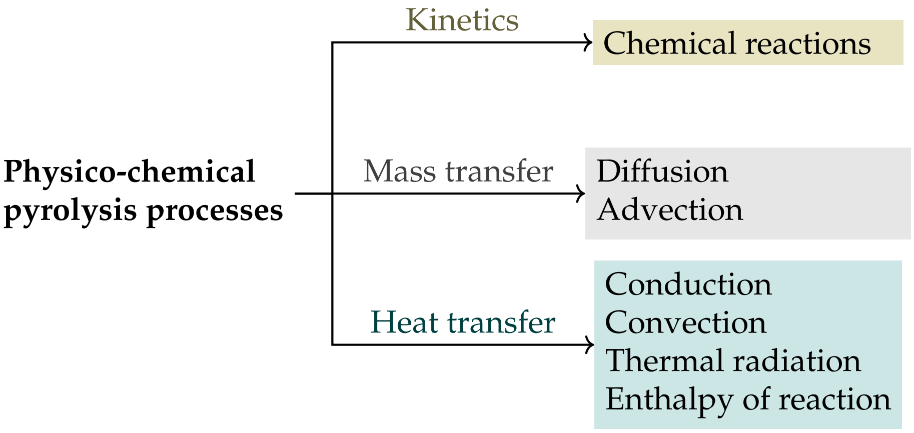

Figure 2.4: Physico-chemical pyrolysis processes.

Once the volatiles are generated, if not removed from the reaction zone (where they are at elevated temperatures), they might react and decompose further or combine to favour gas yield over bio-oil [73]. The secondary reactions involving the volatiles generated from the primary biomass decomposition are called secondary pyrolysis. The time that a volatile released spends near the particle in the reaction area is called the volatile residence time. In the reaction area, the volatiles could undergo secondary pyrolysis due to the high temperatures.

The volatile residence time is not to be mistaken with the solid residence time, which is the time that the solid biomass spends in the reactor. Figure 2.5 shows that, when the volatiles are quickly removed from the reaction area, they can be subsequently condensed, separating the bio-oil from the gas, bio-oil being the major fraction [27]. However, if the volatiles are not quickly removed from the reaction area, they might decompose further or even react with the char, transforming high-density volatiles (bio-oil) into low-density volatiles (gas) [74]. When the volatiles are condensed after undergoing secondary pyrolysis, the gas fraction has increased to the detriment of the bio-oil phase [75]. The order of magnitude of the recommended residence times is discussed later in Section 2.2.3.

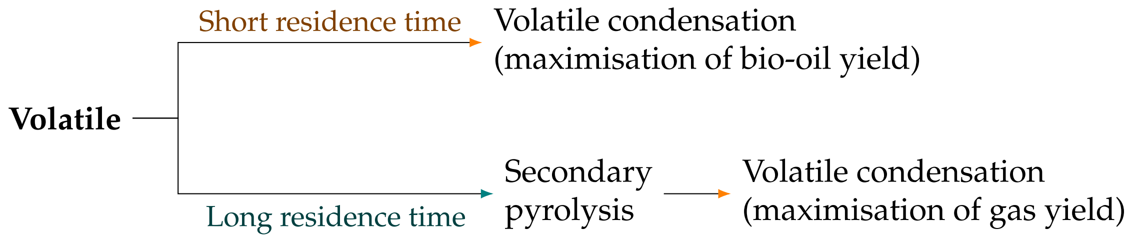

Figure 2.5: Impact of the residence time of the volatiles on the product yields.

2.2.3 Conditions affecting pyrolysis performance

The operating conditions of pyrolysis and the biomass characteristics will determine which are the dominant physico-chemical processes and also the yield and composition of the pyrolysis products. There is extensive experimental work on biomass pyrolysis that consists on adjusting operating conditions or using different biomass samples to see how it translates into the product yield distribution and composition. In this section the most relevant findings in this area are reviewed. The main operating conditions are the temperature program and the volatiles residence time [27], and the main biomass characteristics that can influence pyrolysis are the biomass composition and the shape and size of the biomass particles.

Biomass can be subjected to different **temperature programs**, but it is usually heated with a slow/fast constant heating rate and then held at a final pyrolysis temperature for a certain period of time. The pyrolysis reactions proceed when the biomass reaches a required minimum temperature, which is different for each of the biomass components. It is possible that the temperature of the reactor environment is not the same as the temperature of the biomass. As already mentioned, if the particles are small, they are going to rapidly heat, and it could be assumed that they are at the same temperature as the reactor environment. For large particles, the biomass might have a different inner heating rate that corresponds to how quickly or slowly the heat travels from the biomass surface to its center. Experimental studies comparing different temperature programs for biomass pyrolysis can be found in the literature [76, 77, 78]. Their goal is generally to link the temperature conditions to the product yield distribution. The results of such studies are only representative of the type of reactor used and also of the type and size of biomass.

The **volatile residence time** is the time that the vapour phase spends in the reaction area where the temperature is high. It is an important parameter to take into account if we are interested in optimizing the pyrolysis conditions to get specific species in the bio-oil or gas yield. If the volatiles are quickly removed from the reaction zone and quenched to separate the bio-oil and the gas phase, the bio-oil and the gas yield will have a characteristic composition. If on the other hand the volatiles are not quickly removed, they might have time to decompose further, or react amongst them or with the char, yielding a product composition different from the expected with a short residence time.

The biomass properties that have a major impact on the pyrolysis behaviour are the biomass composition and the shape and the size of the biomass particles. The **biomass composition** can be described in several ways. As already mentioned, the main components of biomass are cellulose, hemicellulose and lignin. The relative composition of the biomass three main components translates into a different pyrolysis behaviour [79]. Each biomass main chemical component undergoes a different decomposition reaction due to their particular chemical structures, and therefore their degradation occurs in distinct temperature ranges. Hemicellulose starts decomposing between 150 and 350°C, cellulose between 275 and 350°C, and lignin between 250 and 500°C [27]. It is also acknowledged that interactions between the components can affect their decomposition [80, 81, 82], but the effect of this interaction is typically assumed not to be significant [79]. Other components that might affect the performance, are the moisture, ash and extractives. The initial moisture in the biomass affects the pyrolysis behaviour and the composition of the bio-oil product [83]. The extractives are minor organic components in biomass like fats, proteins, resins, etc., and they could make up between 5 and 10%wt of the dry biomass [84]. For instance, higher lignin and extractives content favour the char yield, and higher holocellulose (cellulose + hemicellulose) content favours the volatiles yield [85]. Ash represents the inorganic components in biomass. The alkali metals in particular might act as a catalyser and interfere with the pyrolysis reactions [86]. The presence of mineral matter might decrease the decomposition temperature and rate, inhibiting also the volatile generation, more specifically, the liquid fraction [87]. The thermophysical properties of biomass also influence the pyrolysis behaviour, but at the same time the biomass properties change with temperature.

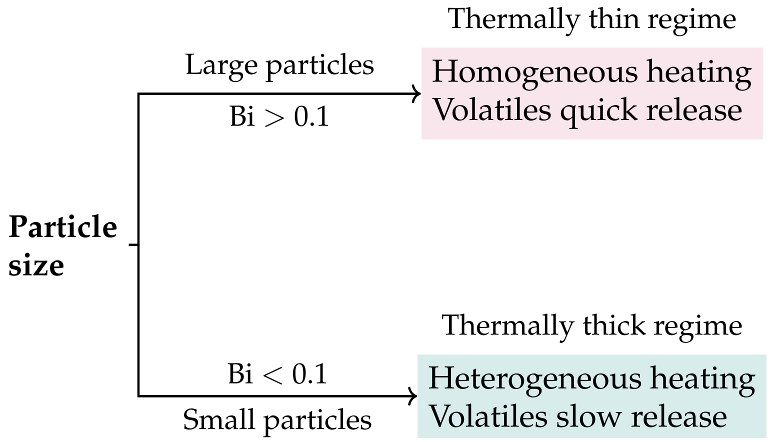

Figure 2.6: Particle thermal regime depending on the particle size.

The **shape and the size** of the biomass particles can influence the pyrolysis behaviour. Figure 2.6 is a diagram that distinguishes the thermal regime corresponding to either small or large particles. The Biot number is defined as $\frac{h\,CL}{\lambda}$, being h the heat transfer coefficient, CL the particle characteristic length, and λ the thermal conductivity coefficient. When Bi is smaller than 0.1, it can be assumed that the particle will heat homogeneously without internal temperature gradients [88]. Small particles are considered to be in the kinetically controlled regime, because the reactions occur homogeneously across the particle [72]. Because of the small size of the particle, the volatiles generated can be quickly released from the particle to the reactor environment. The reactions in large particles do not happen homogeneously across the particle because they depend on the particle inner temperature gradient, and the volatiles generated are released more slowly than with small particles because the volatiles have to travel across the particle porosity [72]. Koufopanos et al. suggested that the pyrolysis process for particles below 1 mm is controlled by the kinetic rate, and for particles larger than 1 mm is controlled by both kinetics and transport processes [79]. Other maximum particle sizes have been reported in the literature depending on the conditions of the experiments performed, but they are generally in the order of 1 mm or below [89]. In terms of product yields, pyrolysis of small particles contribute to an increase in the liquid yield [75, 90].

Different particle shapes and sizes have been considered in pyrolysis studies [91, 71]. Lu et al. [71] compared the pyrolysis of biomass particles of different shapes. The selected shapes were a flat plate, a cylinder and a sphere. They found that the pyrolysis time is higher for spherical particles, and that they also yield less oil than the other particle shapes. The reason is that the spherical particles have a much lower surface area-to-mass ratio in comparison with the other shapes [71]. They also found that the impact of the particle shape on pyrolysis is accentuated with increasing particle size.

According to the pyrolysis operating conditions and the particle size, pyrolysis can be classified as slow (conventional) pyrolysis, fast pyrolysis, and flash pyrolysis [69]. Slow pyrolysis conditions favour the char yield [64], and fast pyrolysis conditions favour the volatile (gas + liquid) yield [27]. Table 2.1 shows a classification of the main pyrolysis types, they are named according to how quickly the biomass is heated. Slow pyrolysis requires a medium final temperature, a slow heating rate, a large particle size, and the process might take in the order of minutes maximizing the char yield. Fast pyrolysis requires a medium high temperature, a medium heating rate, a small particle size, and a short volatile residence time. Flash pyrolysis requires a higher final temperature than fast pyrolysis, a higher heating rate, a smaller particle size and a smaller volatile residence time. The difference between fast pyrolysis and flash pyrolysis is that flash pyrolysis maximizes the bio-oil fraction over the gas fraction in the product yield. Basically, to preserve as many high molecular weight volatiles (bio-oil) as possible, the residence time needs to be very short. However, depending on the desired species in the bio-oil, conditions different from those given in the table might be required.

Table 2.1: Types of pyrolysis according to their operating conditions, adapted from [75, 64, 27].

Operating condition	Slow	Fast	Flash
Pyrolysis temperature (K)	550-950	850-1250	1050-1300
Heating rate (K s^{-1})	0.1-1	10-200	$>$1000
Particle size (mm)	5-50	$<$1	$<$0.2
Solid residence time (s)	$\sim$600	0.5-10	$<$0.5
Volatile residence time (s)	$\sim$600	$<$2	$<$1
Main products	char, gas	bio-oil, gas	bio-oil

At a particle level, other factors that might affect the heat and mass transfer and the extent of reaction, and are usually neglected in the particle models, are swelling, shrinking and changes in the internal particle structure like fragmentation or pore size changes. Shrinkage is believed to influence pyrolysis of particles in the thermally thick regime, because the volatiles generated will have to travel a shorter length through the particle when they are released from it, and it would also reduce the insulation layer between the environment and the center of the particle [92]. The breakage of the particles during biomass pyrolysis is suggested to favour the bio-oil yield, because it reduces the particle size. The breakage is observed to happen at the end of the pyrolysis period when most of the particle is already char; It could happen at medium temperatures caused by a weakened internal structure, or at high temperatures caused by an elevated internal pressure [93].

The desired pyrolysis conditions can be achieved using different reactor configurations. Each reactor has its own biomass capacity and its own heating mechanism, that is why the results from experiments using a specific reactor might not be comparable to the results obtained from a different reactor, despite using similar biomass samples and pyrolysis conditions. The reactor dimension is not in the scope of this thesis, but experimental data from a thermogravimetric analyser and from a single particle reactor are used. In Chapter 3, the experimental data used is taken from the literature, and it was obtained using thermogravimetric techniques to minimize the impact of the heat and mass transfer phenomena. In Chapter 4, the experimental data is obtained by using a single particle reactor, with the aim of studying the biomass pyrolysis at a particle level, including the effect of heat and mass transfer across the biomass, but without having to consider the impact of the reactor configuration and interactions amongst particles.

2.3 Experimental investigation of biomass pyrolysis

When performing experiments of biomass pyrolysis in order to elucidate which are the possible reaction mechanisms, it is important to make sure that the experiments are performed in a kinetically controlled regime, as already discussed in Section 2.2.3, which requires the use of small biomass particles. In that case, it can be assumed that the temperature of the biomass is the same as the temperature of the reactor environment.

Thermogravimetric analysis (TGA) is a widely used standard approach for the analysis of solid-state kinetics [94], including the study of the thermal decomposition of biomass. Thermogravimetric data can be used to estimate a kinetic mechanism configuration, and also to estimate the values of the kinetic parameters that describe each reaction in the kinetic mechanism. In TGA, a sample is subjected to a temperature program, and changes in the weight of the sample are recorded. The plotted curve that describes the weight loss with time or temperature is the thermogravimetric (TG) curve. From the first derivative of the TG curve, the derivative thermogravimetric (DTG) curve is obtained. The DTG curve describes the mass loss rate of the sample (rate of reaction) with temperature or time. A DTG curve from biomass pyrolysis typically features several peaks, each of them corresponding to the individual decomposition of each chemical component [95].

Figure 2.7 is an example of experimental data obtained from thermogravimetric analysis, featuring a TG and a DTG curve with temperature. The mass loss curve starts from a fraction of 1 and decreases about 80 %, with only 20% of the initial weight remaining as char. The DTG curve shows a hint of where the three different reaction peaks, belonging to hemicellulose, cellulose and lignin, could be placed. Each individual peak has a different height (H), a different peak temperature (T_p) and a different width. In this case, peak temperature should not be mistaken with the maximum temperature that is reached during pyrolysis, the peak temperature in this case is the temperature at which the highest point of an individual DTG curve is placed. The width of peak 1 and peak 3 is more difficult to observe because the individual peaks are overlapped. The DTG curve reaches an absolute maximum at a temperature around 630 K, when the mass loss curve displays a steep decrease.

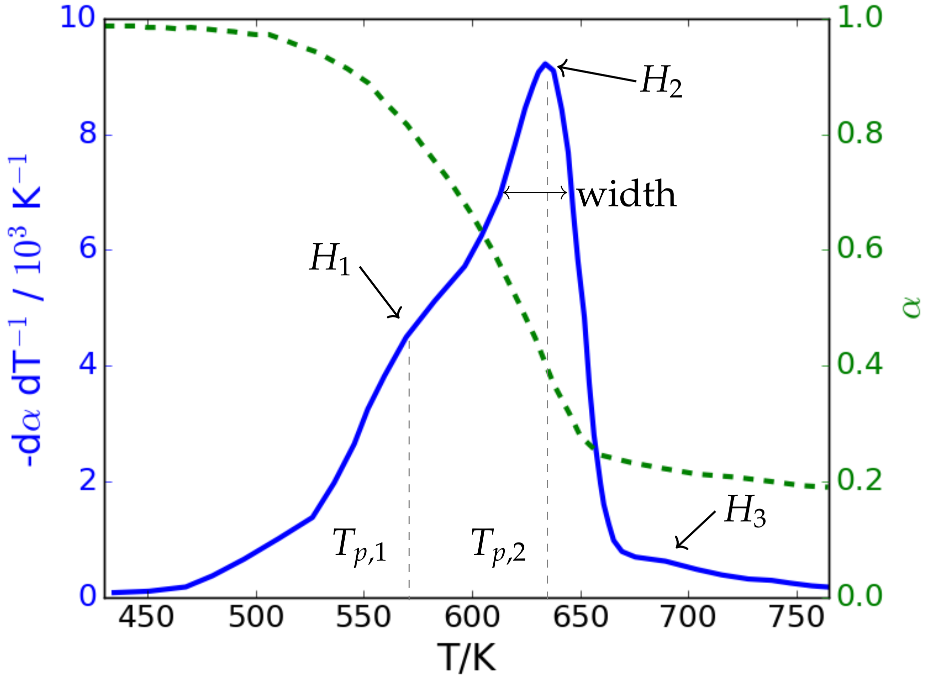

Figure 2.7: Pyrolysis of a wood sample at 10 K min^{-1} [96]. TG curve (green line) and DTG curve (blue line); T_p is the peak temperature, H is the peak height, and the numerical subscript refers to the individual peak.

Either of the two curves could be used to estimate possible reaction mechanisms and kinetics parameters. To do so, some assumptions in terms of reaction model and reaction mechanism need to be made, and in the end it can be assessed how good the initial assumptions were. From the DTG curve, rather than from the TG curve, it is easier to distinguish the different reactions corresponding to the different components, because each peak represents the reaction of a different component, therefore the DTG data might be more meaningful in terms of estimating a reliable kinetic mechanism. TGA is usually performed with small samples of up to 20 mg and a particle size no larger than 100 μm [79]. In TGA, the temperature of the reaction environment can be set constant in order to perform isothermal analysis or set into a dynamic mode, usually consisting of a constant heating rate of up to 100 $\mathrm{K\,min^{-1}}$ [28].

Experiments that seek to study biomass pyrolysis in conditions closer to industrial applications use biomass particles of diverse sizes and shapes, because grounding biomass to fine particles is an expensive process [97] and it would not always be economically feasible. Still, some level of cutting/grinding of the biomass is required as a pre-treatment before entering the pyrolysis reactor [97], resulting in irregular shapes and sizes [98]. Large biomass particles display an internal temperature gradient, as opposed to fine particles that heat instantaneously. From experimental data it has been observed that different pyrolysis temperatures yield a different volatile composition [99], therefore different heating rates also yield different species in the volatile product [100]. Having a large particle with internal temperature gradients is similar to having a fine particle with an external heating rate, because the particle does not heat instantaneously to the final pyrolysis temperature. The size of the particle and its thermophysical properties determines how the internal gradient of temperature is going to be, but different particle sizes also contribute to different volatile species because for large particles there might be volatiles temporarily trapped in the pores, and additional homogeneous and heterogeneous reactions involving the volatiles might take place.

The pyrolysis of large biomass particles can be studied with single particle reactors, or with pyrolysis reactors that have large biomass capacities, but in the latter the particles individual behaviour cannot be discerned. Studies involving pyrolysis reactors of different configurations are very useful to design or optimize the implementation of biomass pyrolysis at both small and large scale, which is the next step after studying the individual behaviour of biomass particles. In this work a single particle reactor is used to experimentally analyse the process of biomass pyrolysis under different operating conditions such as reactor temperature and reactor atmosphere, keeping constant other conditions as the biomass type and pellet size.

The reactor atmospheres used are nitrogen and a combination of nitrogen and oxygen (oxidative pyrolysis). As previously mentioned, there are other thermal processes that can be applied to biomass, such as gasification and combustion. In gasification and combustion there is an oxidative atmosphere, and therefore studies on oxidative pyrolysis are useful to gain a fundamental understanding on the role of oxygen in biomass thermal processes. Furthermore, small amounts of oxygen can be used in order to achieve auto-thermal pyrolysis [101].

2.4 Modelling approaches of biomass pyrolysis

The interest in modelling the process of biomass pyrolysis comes from the need to be able to quickly predict the quantity and quality of the product yields for different types of biomass, and also to be able to optimize the process conditions in order to favour the desired product yields.

2.4.1 Configuration of reaction mechanisms

Kinetic analysis is often used to elucidate the reaction mechanisms of biomass pyrolysis. A good reaction mechanism should be able to predict the pyrolysis behaviour for a wide range of operating conditions and biomass types, in order to be coupled with transport models and thus, scale up the process for industrial purposes. There is not a single way to describe the pyrolysis reactions [102], but in this section the most typical ways of describing them are summarized. A reaction mechanism describes step by step the reactions that take place in a chemical process. The first type of reaction mechanisms that were determined for biomass pyrolysis describe biomass as a single homogeneous component, which is not true, but is an assumption that simplifies a great deal the determination of its decomposition kinetics. An example of the most simple pyrolysis mechanism can be found in Fig. 2.8, which consists of a single first-order reaction (r_1), and can describe the decomposition of biomass, but it does not predict different types of products.

This single-component kinetic scheme can comprise more than a single reaction, and they can be parallel and/or consecutive reactions. Parallel reactions

$$\text{Biomass} \xrightarrow{\mathbf{r}_1} \text{Products}$$

Figure 2.8: Single-component and single-step kinetic scheme.

are competing reactions with a shared reactant, and consecutive reactions are reactions that use the product of a reaction as a reactant for a successive reaction. Each reaction can be described with a set of kinetic parameters such as the activation energy and the pre-exponential factor. A review of the values of the kinetic parameters for single-component mechanisms and for different species of wood can be found in the work of Blasi [103], where some of the mechanisms consist of a single decomposition reaction, but most of them consist of a three-step scheme of configuration similar to the scheme in Fig. 2.9. The value of the pre-exponential factors reported in the literature by Blasi range between 2.4×10^4 and 1.11×10^{11} s^{-1}, and the value of the reported activation energies range between 69 and 177 kJ mol^{-1}. In Fig. 2.9, the decomposition of wood is rendered with three parallel reactions (r_1, r_2, r_3) yielding three types of product, and each product is described in a general manner, independent of the specific species comprised in them.

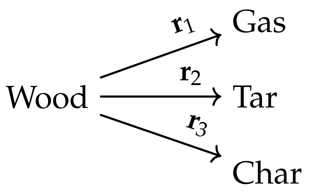

Figure 2.9: Single-component and three-step scheme of wood pyrolysis.

Thermogravimetric data from similar types of biomass can be analysed collectively to obtain a single reaction mechanism that is generalizable to biomass groups, like hardwood or softwood. Kinetic mechanisms can also be specific to one biomass component. Cellulose is the most studied biomass component, and the same type of scheme configurations as in wood pyrolysis have been used to describe cellulose pyrolysis. Figure 2.10 shows an example of a kinetic scheme for cellulose pyrolysis. This scheme is different in that an intermediate step is included, in which cellulose first transforms into active cellulose before transforming into the final products. Active cellulose is not a product in itself, but this intermediate step is a practical approach to render an observed delay in the decomposition of the solid, of which the cause is unknown or difficult to model.

Figure 2.10: Cellulose kinetic scheme [104].

Up to this point, we have seen kinetic mechanisms suitable for specific types of biomass, but they are not generalizable to other biomass types. A practical approach to increasing the applicability of the determined kinetic mechanisms to a wider range of biomass types, is to assume that the overall decomposition of a biomass sample can be described as a sum of the individual decomposition of its main chemical components (cellulose, hemicellulose and lignin) [95]. This assumption is corroborated by the presence of multiple peaks in the DTG curve; If there was a single reaction, there would be only one peak in the DTG curve. A second assumption that is usually made, is that there are no significant interactions between the biomass components [79], otherwise the overall pyrolysis behaviour of a biomass could not be rendered just by adding the individual pyrolysis behaviour of its components, it would also have to take into account potential reactions amongst them, that modify the overall decomposition rate and the products yield distribution. Components interactions are generally considered not to have a significant impact on the overall decomposition process, but some experimental studies have shown that in some cases, the possible interactions of the biomass components might have an impact on the pyrolysis behaviour. For instance, at high temperature, lignin and cellulose interaction has been found to reduce the generation of levoglucosan, increasing the yield of low molecular volatiles [105]. At this point in time, reaction mechanisms for biomass pyrolysis that include the effect of the interactions amongst components have not yet been described in the literature.

A multi-component kinetic mechanism comprises the individual decomposition behaviour of each component. Sometimes other components could be taken into consideration, like water and extractives. Each reaction scheme can comprise a series of single-step reactions and/or consecutive reactions. In this way, the kinetic parameters are estimated for each biomass component, and what determines the pyrolysis behaviour and the product yields of the different biomass types, is their different relative amounts of each component.Two examples of such multi-component mechanisms can be found in Fig. 2.11, both of them yielding three types of product, bio-oil, char and gas. Both mechanisms consist of three first order reactions, two of them yielding products. The difference between the two mechanisms is the way in which they group the products. In the mechanism from Miller et al. [106], the char and the gas are yielded from the same reaction, but in different amounts, given by the fraction x. In the mechanism from Koufopanos et al. [79], is the bio-oil and the gas that are yielded from the same reaction. The way in which these mechanisms lumped the products was perhaps due to the lack of data about the final product characterization.

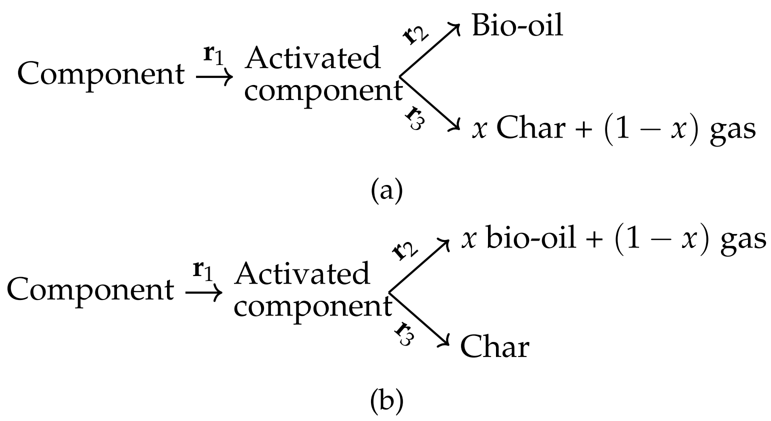

Figure 2.11: Two examples of a biomass component pyrolysis scheme as a part of a multi-component mechanism, (a) from Miller et al. [95] and (b) from Koufopanos et al. [79].

Kinetics mechanisms proposed for biomass pyrolysis have been changing and increasing in complexity and detail with the development of new computational and experimental techniques. The multi-component reaction mechanisms could become more complex if instead of having three types of products (gas, liquid and solid), the reactions would predict the specific species in the gas and in the bio-oil phases. More recently, Ranzi et al. [107, 108] developed a multi-component detailed mechanism using sample molecules for hemicellulose, cellulose and lignin, and yielding specific species in the bio-oil and gas products. Their mechanism combines parallel and consecutive reactions and includes a large number of species. The information required to apply this mechanism is the atomic composition of each component/species involved, and as any other multi-component mechanism, information about the composition of the raw biomass. Kinetic mechanisms that render secondary reactions are also available in the literature [95]. Secondary pyrolysis might happen when volatiles are not removed from the reacting zone, and therefore heterogeneous reactions between the volatiles released and the remaining biomass, and homogeneous reactions in the vapour phase might take place. Some mechanisms for the primary pyrolysis already take into account the possibility to add extra reactions of tar decomposing further [95].

In the case of biomass pyrolysis, reaction mechanisms are specially difficult to elucidate because of the very heterogeneous composition of biomass and the complexity of the pyrolysis reactions. Some mechanisms might only be able to render the process for similar types of biomass and for similar operating conditions to the experiments used to determine the reaction kinetics. In the next section several methods to determine the reaction kinetics from thermogravimetric data are reviewed.

2.4.2 Determination of the kinetic parameters

A pyrolysis model describes how the raw biomass transforms into the pyrolysis products with time or temperature. The basic parts required to build a pyrolysis model are a rate equation and a kinetic mechanism. The rate equation usually consists of the Arrhenius constant and a rate law. The rate law describes how the rate of reaction changes according to temperature and to the remaining mass left. The Arrhenius constant already has a defined expression but assumptions have to be made for the rate law and the kinetic mechanism. Once a kinetic mechanism has been selected, the values of its kinetics parameters need to be determined. Additionally to the kinetics parameters, if the kinetic mechanism is based on a multi-component approach, the corresponding biomass composition also needs to be determined, either experimentally or by the same mathematical techniques used to determine the kinetics parameters.

The determination of biomass composition and biomass pyrolysis kinetics is an ongoing research topic, due to the lack of a quick and reliable method to analyse the biomass composition, and also to the lack of a definitive kinetic mechanism able to render the complexity of the biomass pyrolysis kinetics for any type of biomass. Wet chemistry techniques are usually employed for the determination of biomass composition, although it is known to be costly, time consuming, and the fractions may be altered in the process. Near infrared (NIR) spectroscopy has been reported as an alternative approach to determine biomass composition, however, this technique requires sophisticated equipment and can result in overlapping absorption peaks, making the identification of components more difficult [109]. Deconvolution (or fitting) of TGA data from biomass pyrolysis is another approach that has been studied to obtain the biomass composition [110, 111, 112, 113], and it can also be used to study the pyrolysis kinetics. In this case the calculated composition accounts for the volatile fractions of each component in biomass, having biomass over 80 wt% of volatile matter on a dry, ash-free basis [114]. The biomass composition found through deconvolution of a DTG curve is suitable to use in combination with a multi-component kinetic mechanism, because the mechanism describes how the volatile fraction of the biomass is released from the solid.

The kinetic parameters can be determined from thermogravimetric data. Ideally, the values of the parameters should be as generalizable to other types of biomass and to other pyrolysis conditions as possible, which is challenging because of the natural heterogeneity of biomass composition. Several methods can be used to determine the kinetics parameters from the derivative thermogravimetric data, in this chapter a new method has been developed (peak shape method [115]). Table 2.2 shows a summary of the most popular methods. In the model-free methods it is assumed that the rate depends on a reaction model $f(\alpha)$, but for the calculation of the reaction kinetics the model does not need to be defined, as opposed to model-fitting methods. In isoconversional methods the calculated activation energy is different depending on the extent of conversion α, as opposed to the other methods in which the value of the activated energy is assumed to be constant during the whole pyrolysis process. The rate equation, that describes the DTG curve, can be used in the differential or integral form, and the thermogravimetric data can be experimentally obtained with a linear temperature program, either isothermal or with a constant heating rate, or with a non-linear program. Only the numerical integration methods are suitable for any temperature program and for mechanisms with consecutive reactions. All methods, except the numerical integration and the peak shape method, are based on linear regression procedures that might lead to oversimplifications [116].

Model-fitting is used in this work to determine the values of the kinetic parameters and also to get an estimated biomass composition, both of them according to a given multi-component kinetic mechanism. The individual component reactions can be distinguished from the DTG curve, and the different characteristic reaction peaks need to be deconvolved using model-fitting. A deconvolution based on a reaction kinetics model normally requires an optimization algorithm and an initial estimate of the model parameters; in addition, the rel-

Table 2.2: Selection of methods to calculate the kinetics parameters from thermogravimetric data. MFI: Model-free isoconversional, MFNI: Model-free non-isoconversional, and MF: model-fitting.

Method	Type	Equation	Temperature
Friedman [117]	MFI	differential	isothermal/const. heating rate
FWO [118, 119]	MFI	integral	const. heating rate
KAS [120, 121]	MFI	integral	const. heating rate
Kissinger [120]	MFNI	integral	const. heating rate
Coats-Redfern [122]	MF	integral	const. heating rate
Peak shape method	MF	integral	isothermal/const. heating rate
Numerical integration	MF	differential	any

ative contribution of the biomass components is needed if a multi-component mechanism is used. If the model is complex or has numerous adjustable parameters, for many algorithms the initial estimates of the parameters should not be too different from their optimal values; therefore, a good initial estimate of the parameters is paramount to achieve a meaningful fit. These initial values would normally be estimated using the results from previous fits or from literature data when available. When a good initial estimate of the parameters is not available, evolutionary optimization algorithms, like differential evolution, genetic algorithms [123] or particle swarm optimization [124] can be used. Evolutionary algorithms do not require good starting values to find a global optimum and are typically initialized randomly; however, these optimization algorithms can be very time consuming.

In this work efforts have been made to relate the basic features of a DTG curve directly to parameters of reaction kinetics models. Previous work has studied how changes in the order of reaction, activation energy, pre-exponential factor and heating rate affect the shape of the mass loss and DTG curves [119]. The peak temperature is a parameter in the Van-Krevelen approximation for the exponential integral of the Arrhenius equation [125], and it is also central in the widely used model-free Kissinger method, able to extract kinetic parameters from DTG data at different heating rates [126]. A method to calculate the kinetic parameters from a single DTG curve was developed by Kim et al. [127], first using the peak temperature and the height of peak, later improved by adding a third shape parameter, which is the conversion at the peak temperature, to determine the reaction order assuming an *n*th-order reaction mechanism [128]. The effect on the DTG curves of different reaction mechanisms was analyzed and described by Dollimore et al. [129] in terms of their width at half-height and conversion at the peak temperature to obtain a correlation between the shape of the DTG curve and kinetic mechanism. Farjas et al. [130] developed an approximate analytical solution for non-isothermal thermogravimetric data, and applied it to the decomposition of calcium carbonate and to the crystallization of amorphous silicon. Their expressions are based on the peak temperature and use an approximation to solve the temperature integral. Most of the previous work in the literature that relates the shape of the DTG curve with reaction kinetics relies on numerical analysis. The approach of this work is entirely analytical and provides a direct link between shape and reaction kinetics. Other analytical attempts developed to solve the mathematical expression that renders the rate of reaction are suitable to be used with a single-component kinetic mechanism, and require data from multiple DTG curves with non-isothermal heating conditions. The present method takes into account all possible shape parameters of the DTG curve, it can be applied with either single-component or multi-component kinetic mechanisms, and it can use experimental data from single or multiple DTG curves that had been obtained in isothermal or non-isothermal heating conditions.

Once the values of the kinetic parameters for a pyrolysis model have been determined with the help of experimental data, ideally the pyrolysis model could be used to predict the pyrolysis behaviour with operating conditions different from the experimental ones, but the model might not be flexible enough to do that. If a model flexible enough to change the operating conditions is desired, a possible solution is to simultaneously evaluate the thermogravimetric data from different TG/DTG curves. With a simultaneous evaluation of multiple experimental data, the idea is to obtain one or more shared kinetic parameters amongst them. The simultaneous evaluation of thermogravimetric data becomes more complex when instead of assuming a single-component mechanism a multi-component mechanism is used, and it can be carried out in several ways. For example, Grønli et al. [131] simultaneously fitted DTG curves from different types of biomass using the same heating rate, and determined a single activation energy for all samples but different pre-exponential factors and component fractions. In contrast, Branca et al. [132] used DTG data from the same type of biomass at different heating rates, and determined a single set of kinetic parameters but different initial component fractions depending on the heating rate. When dealing with multi-component and/or multi-step mechanisms with overlapping reactions, simultaneous non-linear fitting of data from different heating programs is advisable [133].

2.4.3 Combination of kinetics with transport phenomena

The pyrolysis of large biomass particles, as opposed to small biomass particles, cannot be rendered with a zero-dimensional kinetics model, it also requires to capture the effects of how the heat and the mass are transferred across the particle.

Single particle models (SPMs) study the heat and mass transfer inside a large biomass particle, and how they affect the final product yields of pyrolysis. Some of the common assumptions in the SPMs found in the literature are that (1) the particle is a solid with a void fraction (porosity), (2) both the solid and the vapour phase are in thermal equilibrium, (3) the particle does not shrink or break, (4) the heat is transferred from the reactor environment to the particle by thermal radiation and thermal convection, the heat travels through the particle by conduction, and that (5) the volatiles generated behave like an ideal gas and (6) are released from the particle driven by a pressure gradient (mass convection), but their diffusion is neglected. Most of them are based on woody biomass, they are solved with one-dimensional models assuming a spherical particle shape, where the heat and transfer processes happen symmetrically, and they are numerically solved with the finite volume method, which is the method implemented in most of the commercial fluid dynamics software.

SPMs combine kinetics with heat and mass transfer mechanisms. Different type of kinetics mechanisms are used in the SPMs, some studies even compare them to see which assumption of kinetics would be best according to their experimental data [134], but practically all of them use mechanisms that assume that the products are lumped in groups according to their phase (vapour phase or solid phase), or at most the separation of the vapour phase into bio-oil and gas. Also, all SPMs tend to show how the center temperature of the particle increases during pyrolysis, and give information related to the mass loss of biomass and the generation of the pyrolysis products. But with the surge of more advanced computational methods, some assumptions and type of outputs can be revisited. Next some SPMs found in the literature are reviewed, pointing out if they make unusual assumptions or give different kind of results.

Corbetta et al. [135] implemented a detailed kinetic mechanism into a SPM, including secondary pyrolysis reactions. The kinetic mechanism is based on the one previously published by Ranzi et al. [107] in which the biomass components and the pyrolysis products are given in the empirical formula of their representative molecule. Shrinkage was included in the model from Anca-Cuoce et al. [136] and in the model from Babu et al. [92], using a correlation for shrinking that depends on the degree of mass loss and solving the model equations with the finite volume method and the finite difference method respectively. Park et al. [93] experimentally studied the breakage of woody particles undergoing pyrolysis, and to that end they used a SPM to report information related to the distribution and evolution of the particle inner pressure and the char yield. Ciesielski et al. [137] used a three-dimensional SPM that they solved with the finite element method. The reason for using a three-dimensional model is to capture the particle microstructure with its irregular pore sizes and directions of the porosity channels. Solving all the typical heat and mass transfer processes of biomass pyrolysis with such a complex geometry carries an increase of computational workload, therefore they only included the heat transfer with the process of heat conduction, and the mass transfer with the process of mass diffusion, excluding chemical reactions. Some studies have not made the assumption of thermal equilibrium between the gas phase and the solid phase [138, 139], but the reasons or potential gain in accuracy have not been discussed. Ghabi et al. [138] have used a two-dimensional SPM to simulate a fixed bed reactor, potentially all SPM could also depict a fixed bed reactor because both the particle and the biomass in the fixed bed reactor, consist of a solid phase with a void fraction. As they mention, the surface of exchange between the solid and the gas phase in a fixed bed reactor is the same as the pore surface in a single particle. Other studies have used a SPM to study the performance of biomass particles in a reactor by using some operating conditions characteristic of the given reactor types. Di Blasi et al. [140] and Anca-Cuoce et al. [136] coupled a one-dimensional SPM with typical heat transfer coefficients for fixed and fluidised bed reactors, and Anca-Cuoce et al. also compares the computational time required using different time-steps characteristic of different reactors, and an external heat transfer model from a fluidized bed reactor.

The single particle model has parameter unknowns that are difficult to determine from the experiments and their values are usually assumed from the literature. The most sensitive parameters, at least at low-temperature pyrolysis, are the enthalpy of formation of char and tar, the heat transfer coefficient, the thermal conductivity of the biomass and the rate of char formation [141].

2.5 Conclusions

To use biomass as an alternative to fossil fuels, research on the kinetics and transport phenomena of its thermochemical conversion technologies is needed to achieve high energy efficiency. Research on biomass pyrolysis is currently focused on both fundamental and practical aspects of the process, including intrinsic reaction kinetics, and heat and mass transfer at particle and reactor scales. The kinetics and the transport phenomena are the main controlling processes to take into account for reactor and process design, and for the prediction of the product yields. Biomass pyrolysis has a lot of potential but is not yet fully implemented at an industrial scale. Research on biomass thermal treatments at different levels, with the aim of improving the operability of the pyrolysis plants with a diverse range of biomass types, and obtaining a more detailed prediction of the product yields is required.

Thermogravimetric analysis is used to identify a suitable reaction mechanism for biomass pyrolysis, and single particle reactors or reactors with larger biomass capacities are used to investigate the influence of the particle size on the pyrolysis performance. For individual biomass types, a single-component mechanism might successfully describe its pyrolysis behaviour, but when a kinetic mechanism is intended for multiple biomass types, a multi-component mechanism is more capable of rendering different pyrolysis behaviour according to the different biomass compositions. There is a diversity of mathematical methods to obtain the value of the kinetic parameters corresponding to the reaction mechanisms, the election of the best method depends on the level of accuracy desired, the type of reaction mechanism, and the mathematical tools available.

Once a kinetic mechanism and the kinetic parameters have been assumed or determined, to study the pyrolysis behaviour for large biomass particles, a single particle model or a reactor model are necessary to include the processes of heat and mass transfer that take place inside the biomass particle (single particle model), or amongst the biomass particles at different positions inside a reactor (reactor model).

Part of the contribution of this thesis is related to the direct determination of the kinetic parameters for the process of biomass pyrolysis from thermogravimetric data, which is given in the next chapter (Chapter 3), and the other part is related to the investigation of the transport processes that take place inside the biomass particles during pyrolysis (Chapters 4, 5, 6 and 7).

Chapter 3

Development of an analytical solution for a lumped pyrolysis model

In this chapter, a method to estimate the parameters of a reaction kinetics model directly from the features of a DTG curve is developed, in particular, the peak temperature, height, width, skewness, as well as the conversion at the peak temperature. This method is different from the previously reported in the literature in that it is based on parameters observable from the experimental data, it saves computing time by reducing the number of iterations needed to fit experimental DTG data and by providing sensible initial values and constraints to model parameters, independently of the optimization method used and without the need of previous kinetic information of the process. In this case the method is applied to the pyrolysis of biomass and compared with literature data, but it could also be applied to the pyrolysis of a biomass of which there is no previous information in the literature or to any type of polymer decomposition process of which thermogravimetric data can be obtained. Furthermore, it can be used with any reaction model, as long as the number of model parameters does not exceed the number of measurable shape parameters. In this case, a high number of shape parameters are included in the method and can be used in any combination, although the expressions become increasingly complex. In addition, it also allows a simple manner to screen reaction models to determine their applicability.

Explicit expressions are given for single-step nth-order reactions with rate constants given by the Arrhenius equation.

3.1 Kinetics analysis with model-fitting

The purpose of model-fitting or curve-fitting is to determine the values of the kinetics or other model parameters of a given mathematical model of biomass pyrolysis by comparing the calculated results with experimental data. The mathematical model used describes the rate of reaction and the experimental data used is the derivative thermogravimetric data. As previously mentioned, the rate of reaction of biomass pyrolysis is experimentally rendered by the TG/DTG curves (see Fig. 2.7). The DTG curve is preferred for the determination of the kinetics parameters instead of the TG curve because it gives more information about the kinetic mechanism. In the mathematical description of the DTG curve, the decomposition of biomass is often expressed as a function of conversion $\alpha = \frac{m_0 - m_t}{m_0 - m_f}$, where m_0 is the sample initial weight, m_t is the weight at a time t, and m_f refers to the remaining mass when the process has finished. The mathematical expression is

$$\frac{d\alpha}{dt} = k(T)\, f(\alpha), \tag{3.1}$$

where $\frac{d\alpha}{dt}$ is the rate of reaction, $f(\alpha)$ represents the reaction model, T is the biomass temperature, and $k(T)$ is the rate constant, which is usually given by the Arrhenius equation

$$k(T) = A\, e^{\frac{-E}{RT}} \tag{3.2}$$

where A is the pre-exponential factor, E is the activation energy, and R is the universal gas constant.

Several reaction models may be used [94], the simplest one is a first order reaction model $f(\alpha) = \alpha$, where the rate of reaction depends only on the temperature and the amount of remaining unreacted sample.

For non-isothermal analysis at a constant heating rate, the temperature varies with time according to

$$T = \beta t + T_0 \tag{3.3}$$

where β is the heating rate, and T_0 is the temperature of the biomass at the beginning of the process, usually room temperature. Including the expression of the temperature in Eq. (3.1), gives a rate of reaction that changes with temperature

$$\frac{d\alpha}{dT} = \frac{1}{\beta} k(T) f(\alpha). \tag{3.4}$$

In decomposition reactions that occur in a kinetically controlled regime, it is reasonable to assume that the temperature of the biomass sample is uniform and equal to the temperature of the environment. For non-isothermal TG experiments we need to fit the experimental data to a model in order to determine the kinetic parameters. The fitting method is based on the least squares minimization of the difference between the experimental and calculated data. To calculate the reaction rate, we integrate Eq. (3.4):

$$g(\alpha) = \frac{A}{\beta} \bar{p}(T) \tag{3.5}$$

where the functions $g(\alpha)$ and $\bar{p}(T)$ are defined as

$$g(\alpha) = \int_0^{\alpha} \frac{d\alpha'}{f(\alpha')} \tag{3.6}$$

and

$$\bar{p}(T) = \frac{1}{A} \int_{T_0}^{T} dT' \, k(T'). \tag{3.7}$$

In general, the integral $\bar{p}(T)$ cannot be evaluated analytically and must be approximated or determined numerically.

In this work the library LMFIT [142] (non-linear least-squares minimization and curve-fitting) from Python has been used to perform the model-fitting. It requires an objective function, the definition of the model parameters, and depending on the fitting method, also the parameters constraints. The model parameters are usually the activation energy and the pre-exponential factor, but additional parameters related to the rate law or to the biomass composition can also be determined. The parameters constraints are the possible minimum and maximum values of the defined parameters. The objective function is the sum of the residuals between the calculated and the experimental data

$$residual(i) = (x_{sim}(i) - x_{exp}(i))^2 \tag{3.8}$$

where x is the value of the rate of reaction at a given i, and i refers to a given time or temperature.

There is a range of fitting methods available in the LMFIT library. In this work the Levenverg-Marquardt and the differential evolution methods are used. The Levenverg-Marquardt is quick but requires good initial values of the model parameters and parameters constraints, and the differential evolution method is not sensitive to the the parameters values and constraints, but it is extremely time-consuming.

The method developed in the next section will use model parameters different from the activation energy and the pre-exponential factor to fit the data, but the fitting procedure remains the same.

3.2 Peak shape method

Key features that characterize the shape of a peak in a DTG curve are the location of the peak T_p, the height of the peak H_p (see Fig. 2.7 and 3.1), the width from the center to the left of the peak W_-, and from the center to the right of the peak W_+ at a fraction θ of its height (see Fig. 3.1). Given these quantitative measures, the peak can be accurately represented mathematically by the exponential-Gaussian hybrid (EGH) model [143], which is defined as

$$\alpha'_{EGH}(T) = \begin{cases} H_p \exp\left(-\frac{(T-T_p)^2}{2\sigma_w^2+\tau_{asy}(T-T_p)}\right) & \text{if } 2\sigma_w^2 + \tau_{asy}(T-T_p) > 0 \\ 0 & \text{if } 2\sigma_w^2 + \tau_{asy}(T-T_p) \leq 0 \end{cases} . \quad (3.9)$$

where $\alpha' = \frac{d\alpha}{dT}$ is the rate of reaction. This model was originally developed to deconvolve the wide variety of peak shapes that occur in chromatography experiments. The parameters σ_w and τ_{asy} are related to the widths W_- and W_+ as

$$\sigma_w^2 = -\frac{W_+ W_-}{2\ln\theta} \quad (3.10)$$

$$\tau_{asy} = -\frac{W_+ - W_-}{\ln\theta}. \quad (3.11)$$

For a symmetric peak, $W_+ = W_-$, $\tau_{asy} = 0$, and the EGH model reduces to a

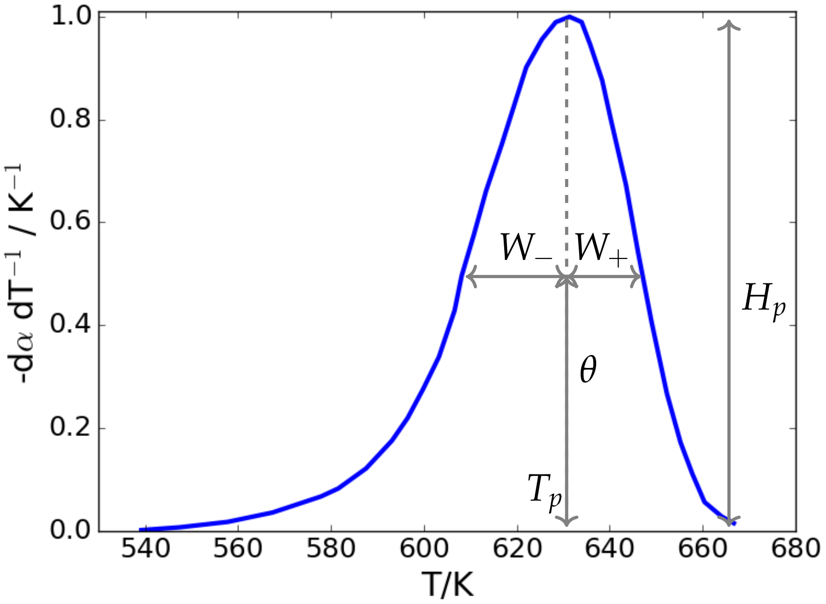

Figure 3.1: Pyrolysis of cellulose at 10 K min^{-1} [144]; W is the width from the center to the side of the peak.

Gaussian peak model; in this case, the full width at half maximum (FWHM) is equal to $2\,(2\ln 2)^{1/2}\sigma_w \approx 2.35\,\sigma_w$, where σ_w would be the equivalent to the standard deviation of a Gaussian distribution with the same curvature at the peak. In the EGH model, the value of σ_w depends on the chosen height fraction of the peak according to Eq. (3.10). When W_- is larger than W_+, the curve is skewed to the left, and τ_{asy} is negative.

In order to relate the characteristics of the peak shape to the parameters of a reaction kinetics model, a Taylor series expansion of the natural logarithm of the reaction rate $\ln\alpha'(T)$ around the peak temperature T_p is performed

$$\ln\alpha'(T) \approx [\ln\alpha'(T_p)] + \frac{1}{2}[\ln\alpha'(T_p)]''(T-T_p)^2 + \frac{1}{3!}[\ln\alpha'(T_p)]'''(T-T_p)^3 + \cdots\,, \tag{3.12}$$

and the resulting expression is compared to the corresponding Taylor series expansion of the exponential-Gaussian hybrid $\ln \alpha'_{EGH}(T)$

$$\ln \alpha'_{EGH}(T) \approx \ln H_p - \frac{(T-T_p)^2}{2\sigma_w^2} + \frac{\tau_{asy}}{4\sigma_w^4}(T-T_p)^3 + \cdots . \tag{3.13}$$

Matching the expressions order by order, a set of relationships between the derivatives of the reaction rate at the peak temperature and the parameters that characterize the shape of the peak are obtained

$$\ln \alpha'(T_p) = \ln H_p \tag{3.14}$$

$$[\ln \alpha'(T_p)]' = 0 \tag{3.15}$$

$$[\ln \alpha'(T_p)]'' = -\sigma_w^{-2} \tag{3.16}$$

$$[\ln \alpha'(T_p)]''' = \frac{3}{2}\frac{\tau_{asy}}{\sigma_w^4}. \tag{3.17}$$

The conversion at the peak temperature (α_p) can be determined from the relation

$$g(\alpha_p) = \frac{A}{\beta}\bar{p}(T_p). \tag{3.18}$$

Equations (3.14)–(3.18) provide the required constraints on the parameters of the reaction kinetics that need to be satisfied in order to reproduce the peak height H_p, the peak temperature T_p, the width of the peak σ_w, the peak skewness τ_{asy}, and peak conversion α_p, respectively.

Figure 3.2 compares the Gaussian, EGH, and n-order reaction kinetics models for the same peak temperature and the same values of σ_w to show the dif-

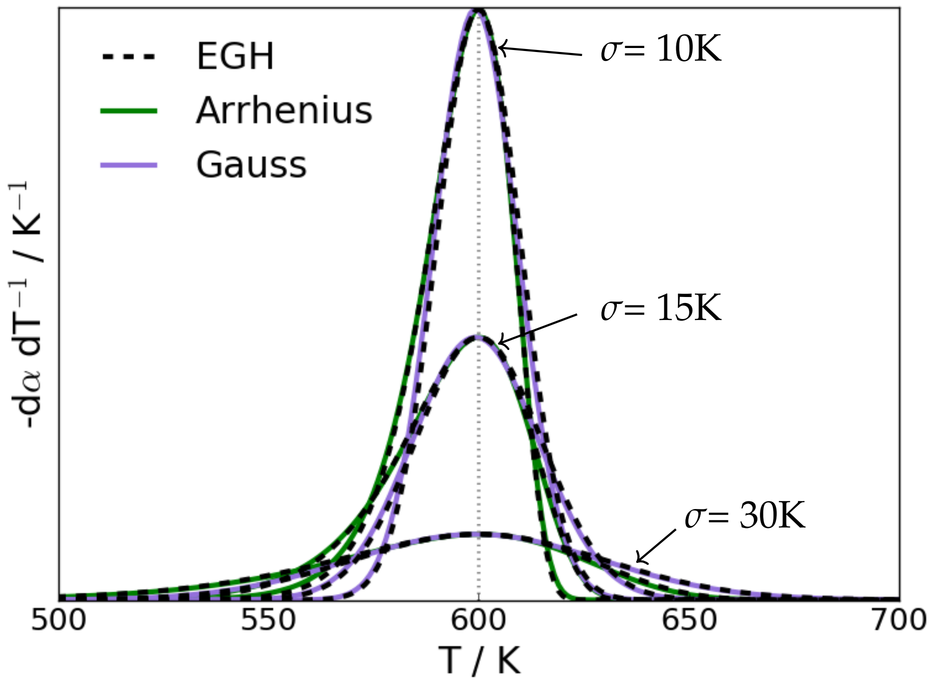

Figure 3.2: Peaks comparison at $T_p = 600\,\text{K}$ and at different values of σ_w. The Arrhenius parameters are $E = 300.0\,\text{kJ mol}^{-1}$, $A = 9.5 \times 10^{23}\,\text{s}^{-1}$ and its similarity with the Gaussian curve is RMS = 0.06% ($\sigma_w = 10$ K), $E = 200.0\,\text{kJ mol}^{-1}$, $A = 1.3 \times 10^{15}\,\text{s}^{-1}$ and RMS = 0.03% ($\sigma_w = 15$ K), $E = 100.0\,\text{kJ mol}^{-1}$, $A = 1.3 \times 10^{6}\,\text{s}^{-1}$ and RMS = 0.0% ($\sigma_w = 30$ K). The EGH model parameter corresponding to the Gaussian distribution is $\tau_{asy} = 0$ for all the sigma values, and the EGH model parameters corresponding to the Arrhenius model are $\tau_{asy} = -6$ K and RMS = 0.01% ($\sigma_w = 10$ K), $\tau_{asy} = -8.6$ K and RMS = 0.01% ($\sigma_w = 15$ K), and $\tau_{asy} = -14.6$ K and RMS = 0.01% ($\sigma_w = 30$ K).

ference between the skewness of the Gaussian curves and the curves derived from the Arrhenius expression, displaying the latter an asymmetric peak, and how well the EGH model can reproduce both models. A Gaussian model only requires the peak temperature and the value of sigma. The error has been calculated with the root mean square as RMS = $\frac{\sum_i^n (y1_i - y2_i)^2}{n}$, where $y1$ and $y2$ are the values compared from two different curves, i denotes the value at a given time and n is the total number of values. The Arrhenius parameters have been determined from the Gaussian curves, and the EGH model parameters have been determined for both, the Gaussian curves and the Arrhenius curves. The Arrhenius curves are distinct from the Gaussian because they are intrinsically asymmetric, as opposed to the Gaussian curves. The EGH model on the other hand, can reproduce well both the Gaussian and the Arrhenius model, because the EGH model incorporates a parameter τ_{asy} related to the asymmetry of the curves which can be set to zero for symmetrical curves. The skewness to the left of the Arrhenius DTG curve is common in non-isothermal reactions where the reaction rate increases with time until the unreacted mass is too small to keep increasing and drops, and a skewness to the right would be characteristic of isothermal conditions [145].

The derivatives in Eq. (3.12) can be calculated for a given choice of rate constant $k(T)$, even if the rate constant was not given by the Arrhenius expression, and a given choice of reaction model $f(\alpha)$,

$$\ln \alpha'(T_p) = \ln k(T_p) + \ln f(\alpha_p) \tag{3.19}$$

$$[\ln \alpha'(T_p)]' = [\ln k(T_p)]' + [\ln f(\alpha_p)]'\alpha'(T_p) \tag{3.20}$$

$$[\ln \alpha'(T_p)]'' = [\ln k(T_p)]'' + [\ln f(\alpha_p)]''[\alpha'(T_p)]^2 \tag{3.21}$$

$$[\ln \alpha'(T_p)]''' = [\ln k(T_p)]''' + \sigma_w^{-2}[\ln k(T_p)]' + [\ln f(\alpha_p)]'''[\alpha'(T_p)]^3. \tag{3.22}$$

The relationships presented up to this point are general and valid for any expression of $k(T)$ and $f(\alpha)$.

3.2.1 *n*th-order reaction model

In this section, the attention is focused on reaction models of the general form

$$f(\alpha) = (1-\alpha)^n, \tag{3.23}$$

where n is the order of the reaction. The integral of the nth order reaction model is

$$g(\alpha) = \frac{(1-\alpha)^{1-n} - 1}{n-1} \tag{3.24}$$

Using this in Eq. (3.5) gives the conversion as an explicit function of the temperature

$$\alpha = 1 - \left[1 + (n-1)\frac{A}{\beta}\bar{p}(T)\right]^{\frac{-1}{(n-1)}}. \tag{3.25}$$

The corresponding expressions for the derivatives of the rate of reaction assuming an nth-order reaction model are

$$\ln \alpha'(T_p) = [\ln \bar{k}(T_p)]' - \frac{n}{n-1} \ln \left(1 + (n-1)\frac{A}{\beta}\bar{p}(T_p) \right) = \ln H \tag{3.26}$$

$$[\ln \alpha'(T_p)]' = [\ln \bar{k}(T_p)]' - n\frac{A}{\beta}\bar{k}(T_p) \left[1 + (n-1)\frac{A}{\beta}\bar{p}(T_p) \right]^{-1} = 0 \tag{3.27}$$

$$[\ln \alpha'(T_p)]'' = [\ln \bar{k}(T_p)]'' - \frac{1}{n}\{[\ln \bar{k}(T_p)]'\}^2 = -\sigma_w^{-2} \tag{3.28}$$

$$[\ln \alpha'(T_p)]''' = [\ln \bar{k}(T_p)]''' - [\ln \bar{k}(T_p)]''[\ln \bar{k}(T_p)]' + \frac{n-2}{n^2}\{[\ln \bar{k}(T_p)]'\}^3 = \frac{3}{2}\frac{\tau_{asy}}{\sigma_w^4} \tag{3.29}$$

$$\alpha_p = 1 - \left[1 + (n-1)\frac{A}{\beta}\bar{p}(T_p) \right]^{-1/(n-1)} . \tag{3.30}$$

where $\bar{k}(T_p)$ is the rate constant $k(T_p)$ excluding the temperature independent parameter A. Equation (3.26) is related to the height of the peak, Eq. (3.27) is related to the position of the peak, Eq. (3.28) and (3.29) can be used in Eqs. (3.16) and (3.17) to obtain expressions for σ_w and τ_{asy}. Eq. (3.30) gives the conversion at T_p, which might be useful to identify the best reaction model or, in the case of nth-order reaction models, the order of reaction [146].

The expressions derived up to this point, are general expressions that could be applied with any rate constant for an nth-order reaction model. From now on we are going to make the assumption that the rate constant is given by the Arrhenius equation (Eq. 3.2).

The corresponding derivatives of the Arrhenius equation are

$$\ln \bar{k}(T) = -\frac{T_E}{T} \tag{3.31}$$

$$[\ln \bar{k}(T)]' = \frac{T_E}{T^2} \tag{3.32}$$

$$[\ln \bar{k}(T)]'' = -2\frac{T_E}{T^3} \tag{3.33}$$

$$[\ln \bar{k}(T)]''' = 6\frac{T_E}{T^4}. \tag{3.34}$$

where $T_E = \frac{E}{R}$.

The resulting expressions for the peak width and peak asymmetry parameters for nth-order reactions are

$$\sigma_w = n^{\frac{1}{2}} \frac{T_p^2}{T_E} \left(1 + 2n\,\frac{T_p}{T_E}\right)^{-\frac{1}{2}} \tag{3.35}$$

$$\tau_{asy} = \frac{2}{3}(n-2)\,\frac{T_p^2}{T_E}\left[1 + 2n\left(\frac{T_p}{T_E}\right)\right]^{-2}\left[1 + \frac{2n^2}{n-2}\left(\frac{T_p}{T_E}\right) + \frac{6n^2}{n-2}\left(\frac{T_p}{T_E}\right)^2\right] \tag{3.36}$$

It is interesting to notice that the peak width and asymmetry for this reaction kinetics model are dictated by the activation energy and the order of the reaction; they are independent of the pre-exponential factor of the Arrhenius equation.

According to the given ranges of typical activation energies of biomass pyrolysis [103], T_E would vary for hemicellulose between 9622 and 13952 K, cellulose between 2345 and 34400 K, and lignin between 2165 and 7818 K.

By knowing E and n, the pre-exponential factor can be determined from Eq. (3.27), which leads to

$$A = \beta \frac{1}{n} \left(\frac{T_E}{T_p^2} \right) e^{T_E/T_p} \left[1 - \frac{(n-1)}{n} \left(\frac{T_E}{T_p^2} \right) e^{T_E/T_p} \bar{p}(T_p) \right]^{-1} . \tag{3.37}$$

From this expression it can also be observed that the pre-exponential factor carries the effect of the heating rate.

The height of the DTG peak can be determined from Eq. (3.26)

$$H = \frac{A}{\beta} e^{-T_E/T_p} \left[1 + (n-1) \frac{A}{\beta} \bar{p}(T_p) \right]^{-n/(n-1)} . \tag{3.38}$$

Figure 3.3 shows how well the curve characteristics of the EGH model translate into the Arrhenius nth-order model for a range of given values of σ_w and τ_{asy}. Both curves are fitted at half height and at that point they perfectly match, nonetheless, they slightly differ at the base of the curve.

Figure 3.4 shows a comparison using the EGH model, of three different values of τ_{asy} for a given value of T_p, σ_w, height and heating rate, and it reflects how the value of τ_{asy} is related to the skewness of the curve, the more negative is τ_{asy}, the more skewed is the curve; the chosen values of τ_{asy} are negative representing a curve skewness to the left.

Figure 3.5 shows in which way the EGH parameters translate into the nth-order Arrhenius ones (n, E, and A), for given values of heating rate, T_p and σ_w, and changing values of τ_{asy}; the three kinetic parameters decrease with a more negative τ_{asy}, meaning that the values of the kinetic parameters decrease as the curve is more skewed to the left.

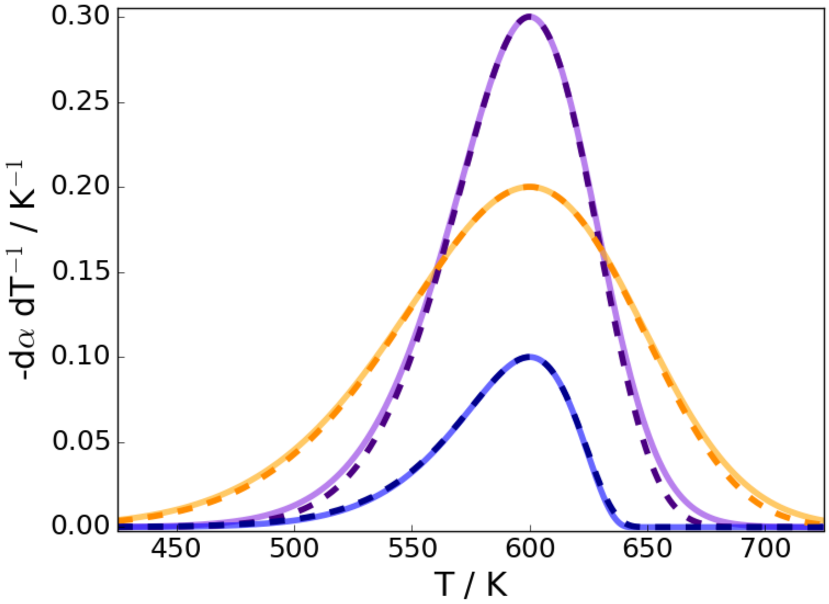

Figure 3.3: Peaks comparison of EGH model (dashed line) and nth-order Arrhenius (solid line) at 20 K min^{-1} and $T_p = 600$ K. The EGH parameters $H_p = 0.3\,\mathrm{K}^{-1}$, $\sigma_w = 30$ K and $\tau_{asy} = -10$ K transform into the Arrhenius parameters $E = 103.3\,\mathrm{kJ\,mol}^{-1}$, $A = 1.1 \times 10^7\,\mathrm{s}^{-1}$, $n = 1.2$ and a RMS = 6.0% (purple); the EGH parameters $H_p = 0.2\,\mathrm{K}^{-1}$, $\sigma_w = 50$ K and $\tau_{asy} = -15$ K transform into the Arrhenius parameters $E = 57.9\,\mathrm{kJ\,mol}^{-1}$, $A = 6.9 \times 10^2\,\mathrm{s}^{-1}$, $n = 1.1$ and a RMS = 5.1% (orange); and the EGH parameters $H_p = 0.1\,\mathrm{K}^{-1}$, $\sigma_w = 25$ K and $\tau_{asy} = -20$ K transform into the Arrhenius parameters $E = 100.9\,\mathrm{kJ\,mol}^{-1}$, $A = 7.0 \times 10^6\,\mathrm{s}^{-1}$, $n = 0.8$ and a RMS = 0.0% (blue).

The fraction of each component that can be determined from a DTG curve is their corresponding contribution to the volatiles released. The height of the peaks is related to the component fractions for a $\frac{d\alpha}{dT}$ peak, according to

$$x = H\,\frac{\beta}{A}e^{T_E/T_p}\left[1 + (n-1)\frac{A}{\beta}\bar{p}(T_p)\right]^{-n/(1-n)} . \tag{3.39}$$

In this section, mathematical relationships have been given between parameters that characterize the shape of a peak in a DTG curve and the parameters

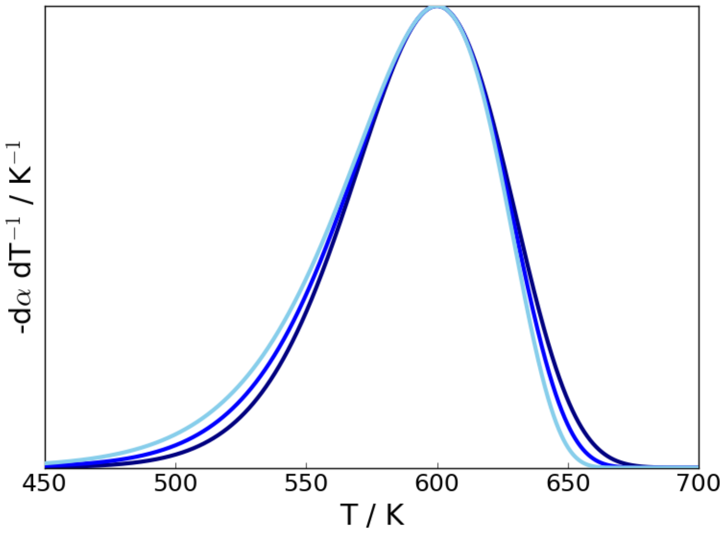

Figure 3.4: EGH model peaks comparison at 20 K min^{-1}, $T_p = 600$ K and $\sigma_w = 30$ K for different values of τ_{asy}: -10 K (dark blue), -15 K (blue) and -20 K (light blue).

of an *n*th-order reaction kinetics model. In Sec. 3.2.2, the found relationships are adapted for a first order reaction model.

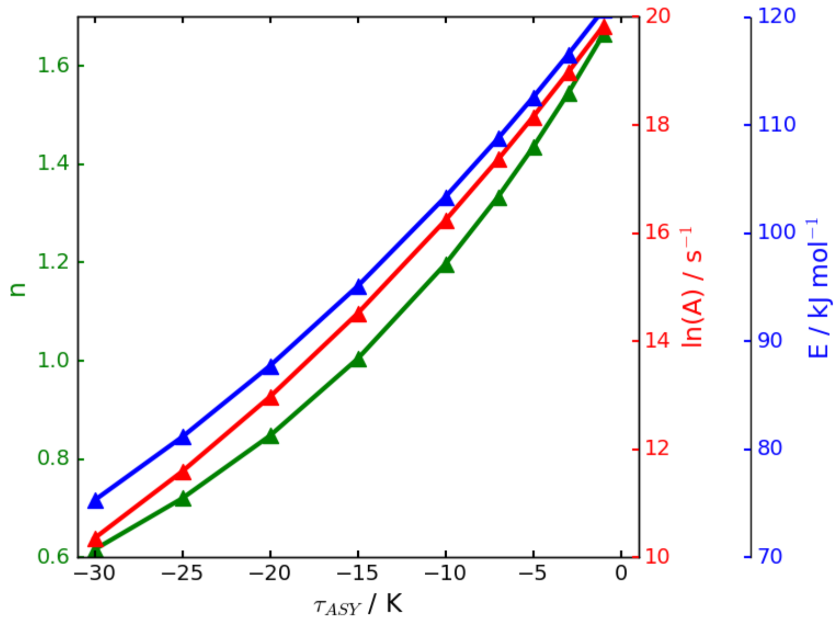

Figure 3.5: Corresponding values for the kinetic parameters of an nth-order Arrhenius model from the EGH model, for a heating rate of 20 K min^{-1}, $T_p = 600$ K and $\sigma_w = 30$ K, with different values of τ_{asy}.

3.2.2 First-order reaction model and Arrhenius rate constant

For a first-order reaction model, $n = 1$, and $f(\alpha) = (1 - \alpha)$. The expressions for σ_w, τ_{asy}, and the pre-exponential factor found for nth-order given in Sec. 3.2.1 simplify to

$$\sigma_w \approx \frac{T_p^2}{T_E} \tag{3.40}$$

$$\tau_{asy} \approx -\frac{2}{3}\frac{T_p^2}{T_E} \tag{3.41}$$

$$A = \beta \frac{T_E}{T_p^2} e^{T_E/T_p}. \tag{3.42}$$

It is worth noting that this expression for the pre-exponential factor turns out to be the same as in Kissinger method [120, 147] with its corresponding form.

Assuming an Arrhenius rate constant, the integral $\bar{p}(T)$ in Eq. (3.5) would be defined as $\bar{p}(T) = T_E\, p(\frac{T_E}{T})$, where

$$p(y) = -\int_y^{T_E/T_0} dy \frac{e^{-y}}{y^2}. \tag{3.43}$$

For first order, the integral in Eq. (3.24) is now modified to $g(\alpha) = -ln(1-\alpha)$, therefore the expression for conversion is

$$(1-\alpha) = \exp\left[-\left(-\frac{T_E}{T_p}\right)^2 e^{T_E/T_p}\, p(T_E/T)\right]. \tag{3.44}$$

Incorporating this expression, as well as the Arrhenius rate constant and the expressions found for σ_w and A into Eq. (3.4), we obtain the following integrated form of the reation rate, which is for a first order reaction model using an Arrhenius reaction rate

$$\frac{d\alpha}{dT} = -\exp\left[\frac{T_p}{\sigma_w} - \frac{T_p^2}{\sigma_w\, T} - \left(\frac{T_p}{\sigma_w}\right)^2 e^{T_p/\sigma_w}\, p(T_E/T)\right] \sigma_w^{-1} \tag{3.45}$$

The parameters for the peak shape can be converted to the parameters for the kinetics model with Eq. (3.46) and Eq. (3.47):

$$E = R\, \frac{T_p^2}{\sigma_w} \tag{3.46}$$

$$A = \frac{\beta}{\sigma_w}\, e^{T_p/\sigma_w}. \tag{3.47}$$

According to these expressions, E and A are inversely proportional to σ_w, and their values increase with increasing T_p.

The height of the peak is particularly useful when dealing with multi-component mechanisms. The height of the peak is found when $T = T_p$,

$$H_{p,i} = \exp\left[-\left(\frac{T_{p,i}}{\sigma_w}\right)^2 e^{T_{p,i}/\sigma_{w,i}} p(T_E/T_{p,i})\right] x_i\,\beta\,\sigma_{w,i}^{-1}. \tag{3.48}$$

The relative contribution of cellulose, hemicellulose, and lignin to the volatile yield can be estimated from the peak heights H_p of a DTG curve. For a multi-component kinetic mechanism, the total decomposition of the biomass is a sum of the decomposition of its components

$$\frac{d\alpha}{dt} = \sum_{i=1}^{n} x_i \frac{d\alpha_i}{dt} \tag{3.49}$$

where x_i is the fraction of component i. Using Eq. (3.48), the component fraction is given by

$$x_i = \frac{H_{p,i}\,\sigma_{w,i}}{\beta\,\exp\left[-\left(\frac{T_{p,i}}{\sigma_{w,i}}\right)^2 e^{T_{p,i}/\sigma_{w,i}}\,p(T_{E,i}/T)\right]} \tag{3.50}$$

The composition calculated can be used as an initial estimation for the components fractions when fitting the experimental data. The fraction parameters are optimized along with the values of T_p and σ_w.

3.2.3 Simultaneous evaluation

Thermogravimetric data from the same biomass sample, will have different peak positions depending on the heating rate. When considering the decomposition of a single component, the kinetic parameters, in principle, could be calculated adapting the methodology presented previously to deal with different heating rates by equating the expression for the pre-exponential factor, found in Eq. (3.42) for a first-order reaction, from two different heating rates

$$-\ln\frac{\beta}{\beta^*} = \frac{T_E}{T_p^*}\left(\frac{T_p^*}{T_p} - 1\right) + 2\ln\left(\frac{T_p^*}{T_p}\right) \tag{3.51}$$

and a simplified form with only peak shape parameters for a first-order rate law could be obtained

$$-\ln\frac{\beta}{\beta^*} = \frac{T_p^*}{\sigma_w^*}\left(\frac{T_p^*}{T_p} - 1\right) + 2\ln\left(\frac{T_p^*}{T_p}\right) \tag{3.52}$$

where the asterisk corresponds to parameters of the reference conditions. Ideally, given a single peak, for each pair of heating rates, the same activation energy should be found. An example of the application of this equation is given in Sec. 3.3.3.

3.3 Kinetic analysis and application

To illustrate the utility of the expressions developed in the previous sections, specific examples of the kinetic analysis of thermogravimetric data from biomass pyrolysis are provided, where the reactions are assumed to proceed with an

Arrhenius rate constant and to follow either a first-order or a *n*th-order model. In Sec. 3.3.1 and 3.3.2, experimental data from a single heating rate experiment are analyzed, and, in Sec. 3.3.3 and 3.3.4, data from several heating rates are evaluated simultaneously. For both cases, the biomass is initially treated as a single component (e.g. pure cellulose), after that, the biomass is treated as a combination of its main chemical components (i.e. hemicellulose, cellulose and lignin).

3.3.1 Case study 1: Experimental data from a single heating rate and a single-component mechanism

Experimental TG data of cellulose pyrolysis at $10\,\mathrm{K\,min^{-1}}$ [144] has been used as an example of kinetic analysis by directly calculating the kinetic parameters from only the measurable features of the peak shape, without the need for performing a fit. The shape parameters are measured on the DTG curve of conversion versus temperature, whose area is one, therefore T_p, σ_w, τ_{asy}, and height and conversion at the T_p are quantitatively estimated. The kinetic parameters for a first order reaction with an Arrhenius rate constant are E and A, and for an *n*th-order reaction model are E, A, and n. The number of peak shape parameters to be measured depends on the number of kinetic parameters to be calculated for the chosen reaction model. For the peak in Figure 3.6, the observed shape parameters are $T_p = 632.4\,\mathrm{K}$, $W_- = 22.9\,\mathrm{K}$, $W_+ = 15.6\,\mathrm{K}$, $H = 0.024\,\mathrm{K^{-1}}$ and $\alpha = 0.616$; the corresponding values of σ_w and τ_{asy} are $16.0\,\mathrm{K}$ and $-10.4\,\mathrm{K}$, respectively.

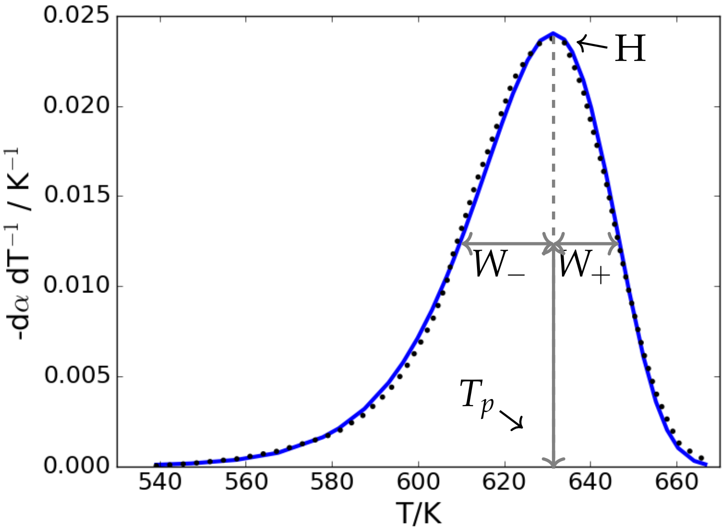

Figure 3.6: Calculated and experimental DTG curve of cellulose pyrolysis at 10 K min^{-1} [144].

Assuming a first-order reaction model, Eq. (3.46) and (3.47) are used to directly calculate the values of the kinetic parameters, resulting in $E = 206.3\,\mathrm{kJ\,mol^{-1}}$ and $A = 1.2 \times 10^{15}\,\mathrm{s^{-1}}$, similar to the literature values of $E = 237\,\mathrm{kJ\,mol^{-1}}$ and $A = 1 \times 10^{18}\,\mathrm{s^{-1}}$ [144]. In this case, the shape parameters that are constrained are T_p and σ_w. Assuming an nth-order reaction model, Eqs. (3.30), (3.35), (3.36), (3.37), and (3.38) can be used to calculate the kinetic parameters. Each expression constrains one of the measurable parameters, but in this case only three of the expressions are needed in order to calculate E, A, and n. In this example, we choose to constrain T_p, σ_w, and τ_{asy}, and, consequently, we obtain $E = 194.9\,\mathrm{kJ\,mol^{-1}}$, $A = 1.3 \times 10^{14}\,\mathrm{s^{-1}}$, and $n = 0.94$. Calculating the height ($H_p = 0.024\,\mathrm{K^{-1}}$) and conversion ($\alpha = 0.625$) from the resulting kinetic values, it can be noticed that the resulting height coincides with the measured one, but the conversion is slightly larger than observed, which makes sense if we compare it with the given range of conversion values for a first-order reaction model [146] and we see that our resulting order of reaction is slightly smaller than one, and conversion at the peak is slightly larger than the literature value. The height and conversion could have also been used to calculate the kinetic parameters, instead of σ_w and τ_{asy}; the only difference is which observable characteristics of the peak shape we want to predict with more accuracy.

3.3.2 Case study 2: Experimental data from a single heating rate and a multi-component mechanism

Experimental thermogravimetric data of beech wood pyrolysis at 5 K min^{-1} [131] were used as an example of deconvolution with a multi-component system in order to determine not only the reaction kinetics, but also the composition of the sample. The fitting procedure of a DTG curve consists of performing a least-squares minimization of the difference between the experimental and predicted rate of mass loss

$$\text{O.F.} = \sum_{k=1}^{n} \left[\left(\frac{d\alpha}{dT} \right)_{calc} - \left(\frac{d\alpha}{dT} \right)_{exp} \right]^2 \tag{3.53}$$

$$\left(\frac{d\alpha}{dT} \right)_{calc} = \sum_{i=1}^{3} x_i \frac{d\alpha_i}{dT} \tag{3.54}$$

For a first-order reaction model, the rate of reaction is calculated with Eq. (3.45) with respect to time. The input values are the initial estimates for the parameters to adjust, determined by direct observation of the DTG curve; These parameters are $T_{p,i}$, $\sigma_{w,i}$, and $H_{p,i}$, where i denotes each component reaction. The biomass relative composition x_i is estimated with Eq. (3.50), and the parameters to be optimized are $T_{p,i}$, $\sigma_{w,i}$, and x_i. The resulting values of $T_{p,i}$ and $\sigma_{w,i}$ can be used in Eqs. (3.46) and (3.47) to obtain the values of activation energy and pre-exponential factor.

The peak temperatures were allowed to vary in a range of 50 K from the selected temperature, this range depends on how distinguishable the curve peaks are and their level of overlapping. In this case, for cellulose and hemicellulose, their T_p was fairly identifiable but not so much for lignin. The σ_w was allowed to vary between $0.5\sigma_w$ and $1.5\sigma_w$. Individual bounds for a particular component can be specified, but yet, provided a good initial guess, the parameters that are clearly around the value given will tend to remain there independently of the size of the range. The resulting fit is shown in Figure 3.7, and the resulting kinetic parameters and composition in Table 3.1. For the deconvolution with the nth-order reaction model, the fit is done directly with the EGH model, setting the bounds for τ_{asy} and σ_w as ($0.5\tau_{asy}$ to $1.5\tau_{asy}$) and ($0.5\sigma_w$ to $1.5\sigma_w$), respectively. In this case, the initial conditions are the resulting parameters found from the deconvolution with a first-order reaction. The resulting kinetic parameters for the first-order reaction model are similar to those reported in the literature, and the calculated kinetic parameters for the nth-order reaction model, which can also be found in Table 3.1, are not far from the values determined for the first-order reaction.

The determined relative contribution of the biomass components is between 34.6% and 41.2% hemicellulose, between 45.8 and 55.7% cellulose and between 9.7 and 13% lignin. The reported composition, experimentally determined for beech [85], is 78% of holocellulose (hemicellulose + cellulose), 20% of lignin, and 2% of extractives on a dry basis. Taking into account that lignin is the major contributor to char formation [148], the calculated results seem consistent with the experimental data, since in the volatile there is a larger fraction of holocellulose than in the raw biomass. In the case of deconvolution of DTG data from a single heating rate, it has been found that there is no significant difference or improvement when considering an *n*th-order reaction model instead of a first-order one.

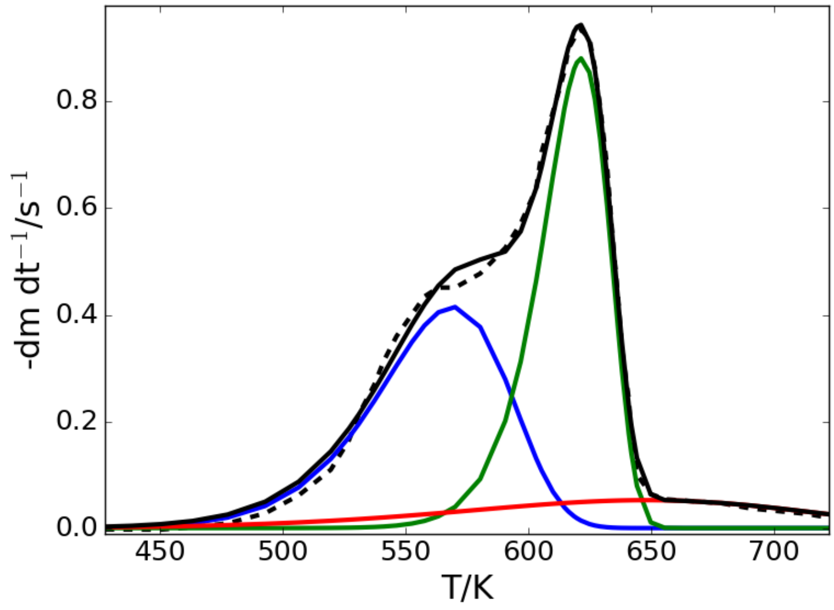

Figure 3.7: Experimental [131] (dashed line) and calculated (solid line) data of beech wood pyrolysis at 5 K min^{-1} using three components: cellulose (blue), hemicellulose (green) and lignin (red).

Fitting is a mathematical procedure that does not obey any thermo-chemical law, and sometimes results that are not in agreement with what we already know about the thermal behavior of the material can be obtained. For instance, in the case example, we need to make sure that the peak temperatures and decomposition ranges are in agreement with what is reported in the literature for

Table 3.1: Resulting kinetic parameters from deconvolution of beech wood as in Fig. 3.7.

Parameter	First-order	nth-order	Literature [131]
E_{HCE} (kJ mol^{-1})	97	114.8	100
A_{HCE} (s^{-1})	2.4×10^6	1.5×10^8	4.3×10^6
E_{CELL} (kJ mol^{-1})	231.5	191.5	236
A_{CELL} (s^{-1})	1.7×10^{17}	6.3×10^{13}	3.8×10^{17}
E_{LIG} (kJ mol^{-1})	45.9	74.3	46
A_{LIG} (s^{-1})	5.5	1.5×10^3	4
n_{HCE}	1	1.3	1
n_{CELL}	1	0.83	1
n_{LIG}	1	1.2	1
χ^2	0.011	0.005	-

similar conditions. The advantage of using the peak shape methodology, is the easy estimation of the initial values to be adjusted, and that their constraints have the same units as in the DTG curve axis. For instance, if we observe that the predicted decomposition does not take place in a temperature range in agreement with the ranges reported in the literature, the fit could be adjusted by shifting the T_p towards the reported range or modifying the bounds to widen them, symmetrically or not.

3.3.3 Case study 3: Experimental data from several heating rates and a single-component mechanism

Experimental data from cellulose pyrolysis at different heating rates [144, 149, 150, 151, 152, 111, 113, 112, 153] were used to exemplify how the peak shape method can be used to find a single set of kinetic parameters across all the DTG experimental data. For DTG data from a single component at different heating rates, Eq. (3.52) could be used to find a single set of kinetic parameters, as rendered in Fig. 3.8b, where each line in the plot corresponds to a different activation energy. The peak shape parameter obtained from the experimental data is the T_p from DTG curves of cellulose pyrolysis at different heating rates, and is represented by black dots. For the sake of clarification, the crosses correspond to calculated data derived for $E = 100\,\mathrm{kJ\,mol^{-1}}$ at three different heating rates, their DTG curves are shown in Figure 3.8a.

If the experimental data would display an ideal behavior, as the calculated data, all points would fall on the same line, defining which is the specific activation energy for cellulose, but as can be observed from the figure, the experimental data does not behave as expected. There could be several explanations for the fact that the experimental data does not define a unique activation energy. One explanation is related to the comparability of the experimental data; It is possible that the different cellulose sources used by the different authors, and the different experimental conditions might have had an impact on the distribution of the peak temperatures, or that the experiments might be governed by transport phenomena rather than being kinetically controlled. Furthermore, it is also possible that the single-step and first-order reaction model does not satisfactorily render the complexity of the decomposition process. The experimental points allow the delineation of a range of activation energies, but to find a single set of kinetic parameters suitable across the range of studied temperatures, a simultaneous evaluation of thermogravimetric data at different heating rates is considered necessary and will be discussed in Sec. 3.3.4.

In Figure 3.8b, at the bottom, the width of the peak is plotted with respect to the heating rate. From both subplots in Figure 3.8b, it can be observed that T_p and σ_w increase proportionally with the heating rate, following the expression

$$\frac{\sigma_w}{\sigma_w^*} = \left(\frac{T_p}{T_p^*}\right)^2 . \tag{3.55}$$

In the following section we use the peak shape method to perform a simultaneous evaluation of DTG data from several heating rates with a multi-component mechanism.

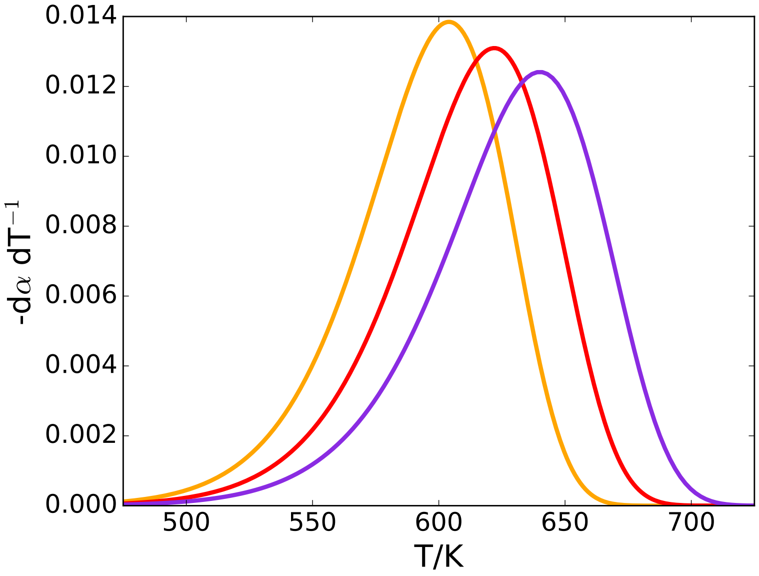

(a) Calculated DTG curves for cellulose pyrolysis derived from E = 100 kJ/mol for different heating rates: 5 K min^{-1} (orange), 10 K min^{-1} (red) and 20 K min^{-1} (purple).

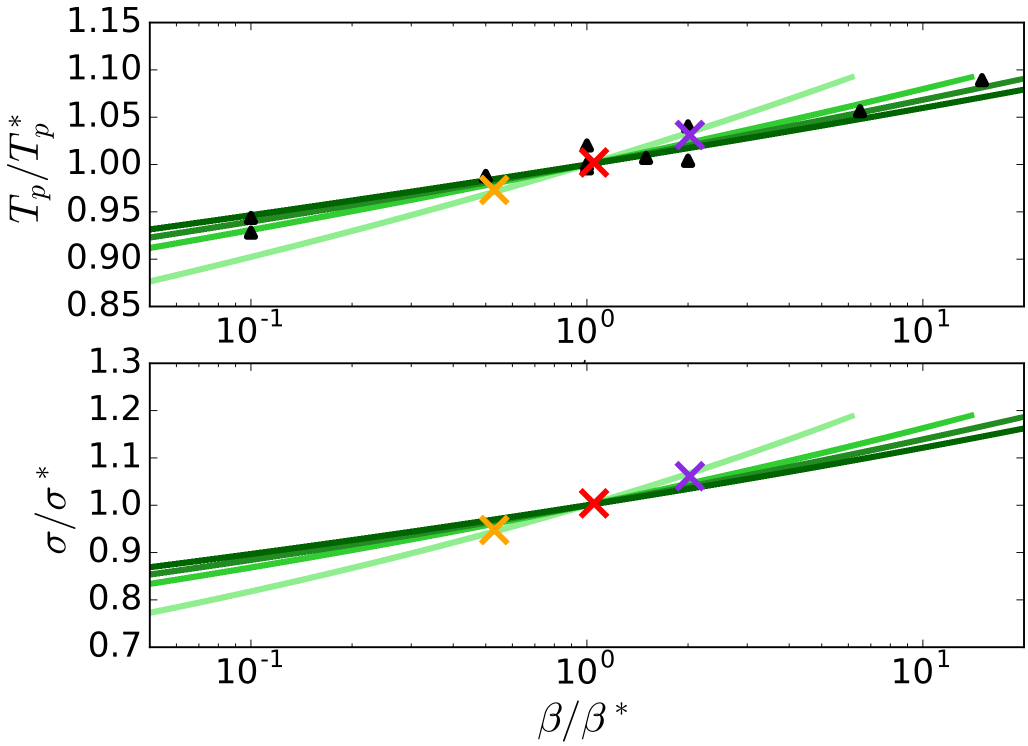

(b) Experimental peak temperature versus heating rate of cellulose pyrolysis [144, 149, 150, 151, 152, 111, 113, 112, 153] (black dots), calculated peak temperature and calculated sigma versus heating rate obtained from figure (a) (crosses), and different activation energy curves for cellulose: 100 kJ mol^{-1}, 150 kJ mol^{-1}, 175 kJ mol^{-1} and 200 kJ mol^{-1} (from light green to dark green).

Figure 3.8: Cellulose pyrolysis at different heating rates, relationship between heating rate and activation energy.

3.3.4 Case study 4: Experimental data from several heating rates and a multi-component mechanism

Experimental data from pyrolysis of macadamia nut shell are taken from the literature [154] to serve as an example of simultaneous deconvolution of several DTG curves at different heating rates, each of them featuring three main peaks corresponding to hemicellulose, cellulose and lignin. The choice of the reference curve is arbitrary. From four DTG curves of biomass pyrolysis performed at heating rates of 5, 10, 20, and $30\,\mathrm{K\,min^{-1}}$, the one at $10\,\mathrm{K\,min^{-1}}$ was selected to be a reference curve. This simultaneous fitting is suitable for single and multi-component decomposition mechanisms, but in the following example, we are going to consider a multi-component mechanism, the more complex of the two.

The input parameters for a first-order reaction model are $T^*_{p,i}$, $\sigma^*_{w,i}$ and $H^*_{p,i}$, where the asterisk indicates that the properties belong to the reference curve and i refers to the biomass component. The initial values for the peak temperature and width are estimated by direct observation of the DTG curve, and the initial estimation of the composition comes from applying Eq. (3.50) to the reference curve. From the fitting, a single composition and a single set of kinetic parameters able to render the biomass decomposition and taking into account the impact of different heating rates is obtained.

The fitting procedure is similar to the one applied for a single heating rate. The difference in this case is that a reference curve is chosen, and the rest of curves at the different heating rates are calculated with Eq. (3.52) with respect to the reference. In this way, only the kinetic parameters for the reference curve $T^*_{p,i}$, $\sigma^*_{w,i}$ and x^*_i, need to be adjusted to minimize the objective function

$$\text{O.F.} = \sum_{k=1}^{n} \left[\left(\frac{d\alpha}{dT} \right)_{\text{calc}} - \left(\frac{d\alpha}{dT} \right)_{\text{exp}} \right]^2 \tag{3.56}$$

$$\left(\frac{d\alpha}{dT} \right)_{calc} = \sum_{j=1}^{4} \sum_{i=1}^{3} x_i^{(j)} \frac{d\alpha_i^{(j)}}{dT} \tag{3.57}$$

where j denotes the different heating rates, and i denotes the components in the biomass.

The bounds for T_p are 50 K on each side of the chosen temperature value, the range is large due the fact that for hemicellulose and lignin the peaks are overlapped and difficult to identify, the lower bound for σ_w is 0.5 times the initial value, and the upper bound is 1.5 times the initial value. The resulting fit can be found in Fig. 3.9 and the resulting kinetic parameters in Tab. 3.2.

Deconvolution of the DTG curves with an nth-order reaction mechanism was also carried out, and the results are reported in Table 3.2. Similar to the deconvolution from a single DTG curve, no significant improvement in the fit was observed by using an nth-order reaction model rather than the simpler first-order model. The experimentally estimated raw material composition of macadamia nutshell is reported by Antal et al [155] and is 17.8% hemicellulose, 26.9%cellulose and 40.1% lignin. The estimated composition of the biomass in this work is 27.1% hemicellulose, between 51.7 and 53.4% cellulose, and between 19.5 and 21.1% lignin. The fractions of cellulose and hemicellulose are larger than the ones reported in the mentioned literature and the lignin fraction is lower, like in the previous example given in Sec. 3.3.2. The calculated

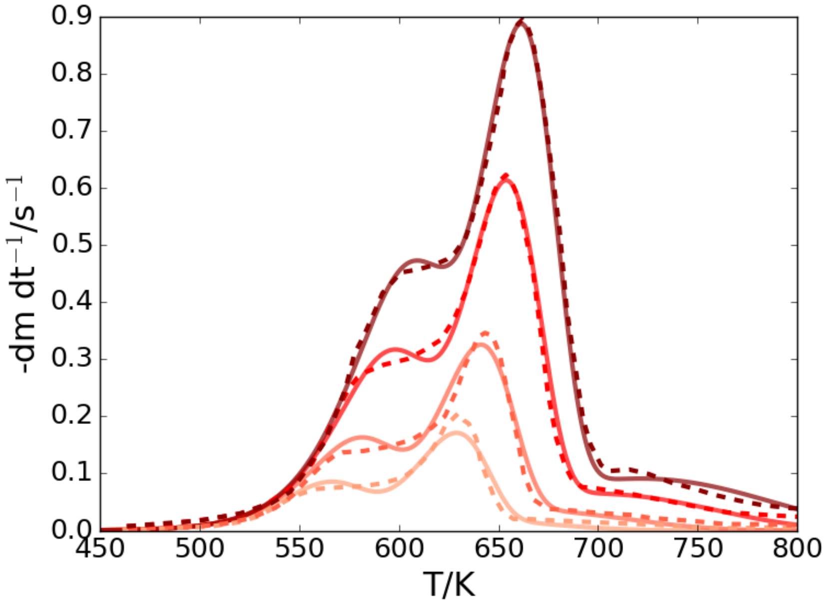

Figure 3.9: Simultaneous evaluation (solid line) of experimental data [154] (dashed line) from macadamia nut shell pyrolysis at different heating rates: 5 K min^{-1}, 10 K min^{-1}, 20 K min^{-1} and 30 K min^{-1} (from light red to dark red).

kinetic parameters are similar too but slightly differ from the reported literature ranges, which might be due to the assumption of only three components and leaving out extractives.

The reliability of the calculated kinetic parameters depends on the initial values, bounds of the fit parameters, the suitability of the chosen kinetic mechanism, and the quality of the experimental data, meaning that the experimental conditions should ensure that the process takes place in a kinetically controlled regime.

Table 3.2: Resulting kinetic parameters from simultaneous deconvolution of macadamia nutshell as in Fig. 3.9.

Parameter	First-order	nth-order	Literature [154]
E_{HCE} (kJ mol^{-1})	125.9	131.4	132.2–150.6
A_{HCE} (s^{-1})	1.9×10^9	6.6×10^9	2.9×10^9–1.8×10^{11}
E_{CELL} (kJ mol^{-1})	182.1	173.1	221.2–265.7
A_{CELL} (s^{-1})	6.2×10^{12}	1.1×10^{12}	8.9×10^{15}–8.2×10^{19}
E_{LIG} (kJ mol^{-1})	59.2	72.7	62.8–74.5
A_{LIG} (s^{-1})	1.3×10^2	1.9×10^3	2.7×10^2–1×10^4
n_{HCE}	1	1.1	1
n_{CELL}	1	0.88	1
n_{LIG}	1	1.2	1
χ^2	0.036	0.028	-

3.4 Conclusions

A method to estimate the parameters of a reaction kinetics model, directly from the shape of the derivative thermogravimetric (DTG) curve was developed. This method is different from the traditional fitting methods in that the model used to determine the kinetics parameters depends only on observable parameters that can be obtained from the thermogravimetric results, therefore it makes the fitting process easier and quicker, because the initial value and the boundaries of the parameters to fit are already known. It is suitable for single or multi-component mechanisms involving single-step reactions. The developed method has been presented and validated with numerical integration and model-fitting.

The present work comprehensively encompasses the measurable shape parameters of the DTG curve of biomass pyrolysis and from the study of chromatography peaks reported in the literature, by deriving mathematical expressions that directly link the peak shape with kinetics. The shape parameters reported in this work can be selected and used in any combination, according to the number of required kinetic parameters specific for each reaction model. This gives the flexibility to decide which are the decomposition characteristics that we want to predict with more accuracy, and also to assume different rate constants and reaction models.

As already mentioned in the literature review, other methods that are based on observable features of the DTG curve use an approximation for the temperature integral, they rely on numerical analysis, and they only use one or a couple of observable properties. The peak shape method is different from the previous ones in that it is entirely analytical, does not rely on any integral approximation, and can use any of the observable properties of the DTG curve. Furthermore, the present method can account for the heterogeneity of biomass because it is also suitable for the decomposition of multiple parallel reactions, and it can use experimental data from both isothermal or non-isothermal heating conditions, as opposed to previous methods.

In the specific examples of application included in this work, an Arrhenius rate constant and first/nth-order reaction models are used, which requires two/three kinetic parameters to be determined. The results of the deconvolution examples, show how the shape method allows for an easy estimation of the initial values of the parameters, which can be obtained by direct observation of the DTG curve. Furthermore, the bounds of the parameters can also be defined from direct observation, in order to improve the fit or reduce the convergence time. When dealing with single-component mechanisms, in which the DTG curve displays a single peak, the kinetic parameters can be calculated by directly applying the expressions that link the peak shape parameters with the reaction kinetics, without the need to fit. For multi-component mechanisms in which the DTG displays multiple peaks, the goodness of the fit relies on the precision of the initial values and bounds of the fit parameters, and their estimation depends on the overlapping degree of the peaks. The resulting kinetic parameters and contribution fractions of the biomass main components, could then be used as the initial values of the key kinetic parameters and provide reasonable constraints in order to reduce the computational cost of more elaborated fitting procedures.

To improve the fit for the given examples, other components could be included in the kinetic mechanism, such as extractives, and differing reaction models from the nth-order could be considered. The present method for the kinetic analysis of thermogravimetric data could also be applied to other similar thermal reactions from which a DTG curve can be obtained, such as drying, crystallization, and decomposition processes of solid fuels or other materials; It would be particularly advantageous to use this method for a process of which there is not much previous kinetic information about it, as long as thermogravimetric data of the process could be obtained.

Chapter 4

Pyrolysis and oxidative pyrolysis of a single biomass particle

In this chapter the experimental work on pyrolysis (with pure nitrogen atmosphere) and oxidative pyrolysis (with 90 vol% nitrogen and 10 vol% oxygen) of a wheat straw pellet is presented. The objective of this experimental work is to find out how sensitive is the election of a reactor and biomass type (by comparing with literature) to the resulting mass loss, product yields and pellet inner temperature. Also how the different inner heating profiles in the particle affect the mass loss and product yields, and to further study the process of devolatilization by finding the temperature range where devolatilization starts.The pyrolysis results are presented in terms of mass loss, inner temperature and gases emissions. Subsequently the inner temperature and the emissions are compared with the results from oxidative pyrolysis.

4.1 Materials and procedure

The biomass material used in this work is wheat straw. Wheat is one of the most important crops worldwide, and wheat straw is the agricultural by-product of harvesting wheat grain for food consumption. The use of agricultural waste reduces the use of energy crops or wood deforestation in order to produce biofuel. More specifically, the samples used are wheat straw pellets purchased from Agripellets Ltd. [156]. Straw pellets are generally produced for industrial and domestic heating purposes in biomass boilers, they are also used in co-combustion with coal [157]. Figure 4.1 shows a picture of a pellet with the pellet dimensions. The pellets received were measured and sometimes modified in order to use an average pellet size of 1 cm length and 7 mm diameter. The figure also shows the position of the thermocouples insertion, which will be discussed later in this section. The pellets were dried overnight at 105°C and kept in a desiccator cabinet. The bulk density of the dry pellet is approximately 780 kg m^{-3} and it was calculated using the measured pellet mass of 0.3 g and the measured pellet volume of 3.8×10^{-7} m^3.

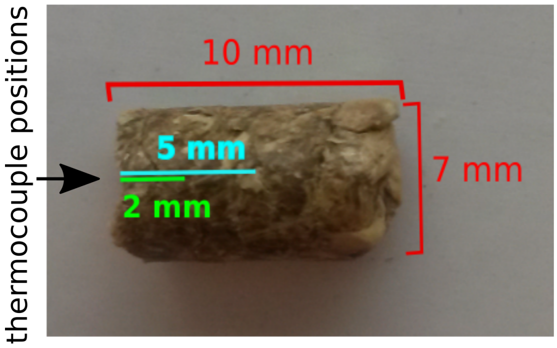

Figure 4.1: Wheat straw pellet dimensions (red lines) and inner thermocouple positions (blue and green lines).

Table 4.1: Physical and chemical characterization of wheat straw (w. straw), straw and wood; Moisture (M), ash, and higher heating value (HHV) are presented in 'as received' basis (ar) and the rest in dry ash-free basis (daf).

Sample	**Proximate analysis wt%**				**Ultimate analysis^{daf} wt%**						**HHV^{ar}**
	M^{ar}	Ash^{ar}	VM^{daf}	FC^{daf}	C	H	O	N	S	Cl	MJ kg^{-1}
w. straw	9.3	6.7	80.8	19.2	48.8	5.67	44.5	0.77	0.16	0.13	17.2
w. straw [158]	7.33	10.53	91.3	8.7	39.71	6.62	52.91	0.55	0.21	-	15.6
w. straw [159]	12.8	4.1	79.4	20.6	49.2	6.4	43.1	0.84	0.12	0.4	16.45
straw [160]	14.4	5.9	81.3	18.7	49.4	6.2	43	0.9	0.25	0.29	16.1
wood [160]	24.2	0.5	84.6	15.4	50.6	6.1	43	0.2	0.03	0.01	15.3

The proximate and elemental analysis of the wheat straw pellets is reported by the supplier (Agripellets Ltd.) and it can be found in Table 4.1, along with the analysis results for wheat straw, straw (as an average of 10 straw samples) and wood (as an average of 12 wood samples) from other sources. These analyses are performed using procedural standards so the results ought to be comparable, as long as they exclude the moisture and ash contents, because that depends on the climate and soil conditions and not so much on the biomass type. The wheat straw composition is very similar in terms of volatile matter and fixed carbon to one of the literature sources [159] and to the expected average contents for straw biomass as a group, but with more ash content, a bit less volatile matter and a bit more fixed carbon than the average contents for wood biomass as a group.

This experimental work was done in collaboration with the Process Chemistry Centre at the Åbo Akademi University. Figure 4.2 features the single particle reactor used in this work, Fig. 4.2a is a picture of the reactor and Fig. 4.2b is a schematic diagram of it. The reactor consists of a quartz tube inserted in a ceramic furnace that is electrically heated. A general description of the reactor is given in this section but further information can be found elsewhere [161, 162]. The inner diameter of the reactor is 4.43 cm. The gas volumetric flow is 220 L h^{-1} for all the experiments, for pyrolysis the gas used is nitrogen and for oxidative pyrolysis a 10 vol% of oxygen and a 90 vol% of nitrogen. Mass flow controllers were used to produce the selected artificial gas mixture keeping the volumetric flow constant. The pellet was sitting in a platinum basket holder, which could potentially interfere with the heat transfer but in this study it has not been considered. The pellet, already placed in the sample holder, was first placed in a lateral quartz arm and kept there till all the oxygen was carried away before introducing the pellet at the center of the reactor in the reacting zone. It took about a second to move the sample from the lateral to the center. After pyrolysis the pellet was pulled out of the reacting zone and kept at the lateral arm till it cooled down with nitrogen gas to avoid further decomposition. After that the sample was ready to be weighed. The experimental measurements taken were the pellet mass loss, the pellet internal temperature, and the emissions of some of the flue gas species.

To measure the mass loss in pyrolysis conditions, samples were extracted from the reactor at different times and rapidly cooled with nitrogen flow at ambient temperature to avoid further decomposition of the pellet. Once the sample is removed from the reactor it is weighted with a scale, which has a maximum error of ± 0.05 mg. Taking into account the weight of the holder with the sample of about 700-800 mg, it supposes a very small percentage error smaller than 1%.

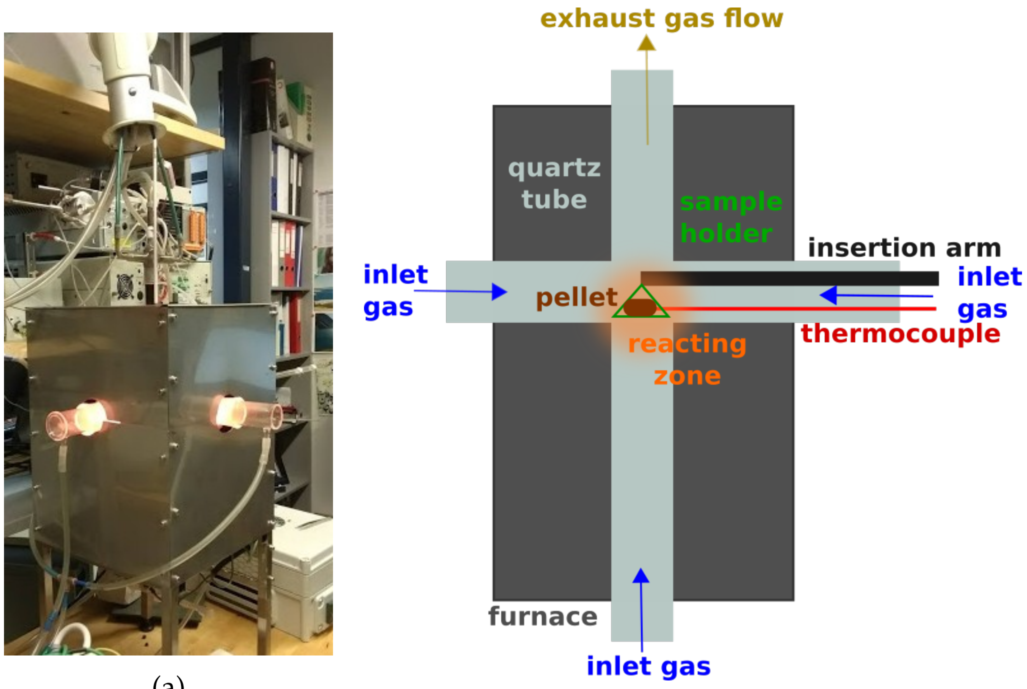

(a)

(b)

Figure 4.2: Single particle reactor (a), and diagram of the single particle reactor (b).

The inner pellet temperature was measured with a thermocouple. The thermocouple was inserted at a designated position in the pellet and the temperature was continuously recorded. To obtain the temperature information from another inner position in the pellet, a repetition of the experiment was carried on. The selected positions were at 2 and 5 mm from an end of the pellet. The center temperature was selected because it is one of the parameters most reported in the literature on pyrolysis of a single biomass particle. The temperature at 2 mm was chosen to have more detailed information about the pellet temperature gradient.

The release of carbon monoxide and carbon dioxide during pyrolysis was continuously analysed from the flue gas that was collected from the top of the reactor with commercial analysers. The gas emissions were measured in mole fraction and converted into mass. The gas analysers were calibrated with pure nitrogen and with different amounts of nitrogen and oxygen to make sure that the selected conditions in the mass flow controllers match the measured gas leaving the reactor. The measuring range for carbon monoxide and carbon dioxide was 10 vol%.

Experiments with oxidative pyrolysis conditions used a gas mixture of nitrogen 90 vol % and oxygen 10 vol%, but only data from the inner temperature and emissions were recorded. In Table 4.2 a list of all the experimental runs is given.

Table 4.2: List of experiments with their respective conditions and measurements.

gas	temperature (°C)	time (s)	repetitions	measurement
N_2	200	200		T(center), emissions
	300	200		T(center), emissions
	400	200	x3	T(center), emissions
	500	∼120	x4	T(center), weight, emissions
	500	∼120	x4	T(2mm)
	500	between 0 and 120	x22	weight
	600	∼120	x4	T(center), weight, emissions
	600	∼120	x4	T(2mm)
	600	between 0 and 120	x22	weight
	700	∼120	x4	T(center), weight, emissions
	700	∼120	x4	T(2mm)
	700	between 0 and 120	x26	weight
$N_2 + O_2$	200	200		T(center), emissions
	300	200	x2	T(center), emissions
	400	∼150	x4	T(center), emissions
	500	∼120	x3	T(center), emissions
	700	∼120	x3	T(center), emissions

4.2 Measured temperature and mass loss during pyrolysis

The pellet's visual changes during pyrolysis are mostly related to the color. Figure 4.3 is included for illustrative purposes. The picture shows the appearance of the pellets after different pyrolysis times. The longer the time, the larger the degree of charring; These pellets where weighed to obtain a mass loss curve with time.

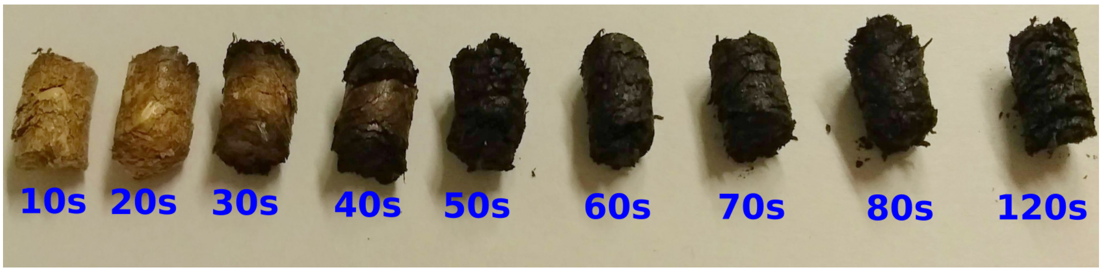

Figure 4.3: Pellet appearance after a given time of pyrolysis for the reactor temperature of 500°C.

Figure 4.4 shows the resulting mass loss of a pellet undergoing pyrolysis with time for three reactor temperatures. The higher the reactor temperature the quicker the decomposition occurs, however they end up having a similar amount of char of about 30% of the initial mass, slightly higher for a lower reactor temperature. It is known that the char yield clearly decreases with increasing pyrolysis temperature up to a point, after that, its decrease with temperature is very small. For instance, the pyrolysis of ground beech wood shows a decrease of char yield with pyrolysis temperature up to 600°C, after that, the drop of char yield is not significant [60]. The amount of final char content, is larger than the determined fixed carbon in the proximate analysis (see Table 4.1) because it includes the ash fraction and because the pyrolysis conditions used for both experiments are different; The fixed carbon from the proximate analysis is calculated by difference with a standard procedure in which the biomass sample is heated to a temperature of 900°C, yielding much less char.

For a reactor temperature of 500°C, the loss of mass happens between 30 and 60 s, and looking at Fig. 4.3 it can be observed that the volume of the pellet did not seem to significantly change with mass loss; for a reactor temperature of 600°C, the main loss of mass takes place between 20 and 50 s; and for a reactor temperature of 700°C, between 10 and 30 s. Similar timescales are reported for the pyrolysis of a wood pellet of similar dimensions [163] (diameter and length of 7 mm), where for a reactor temperature of 500°C the decomposition happens between 40 and 80 s, for a reactor temperature of 600°C between 30 and 70 s, and for a reactor temperature of 700°C, the range between 10 and 30 s matches with the current experimental data. The differences between the literature and the experimental data at lower temperatures could be due to the use of different biomass samples, a different reactor configuration or a different recording technique.

Babu et al. studied the influence of the temperature and the particle size on biomass pyrolysis [164]. For a cylindrical pellet and a pyrolysis temperature of about 627°C, they compared the time required for pyrolysis completion for different particle radius, which goes from 53 s for a radius of 0.25 mm to 717 s for a radius of 13 mm. These times are consistent with the current experimental results for a pellet of diameter 0.7 mm and length 1 cm, requiring about 90 s for a reactor temperature of 600°C and about 75 s for a reactor temperature of

700°C.

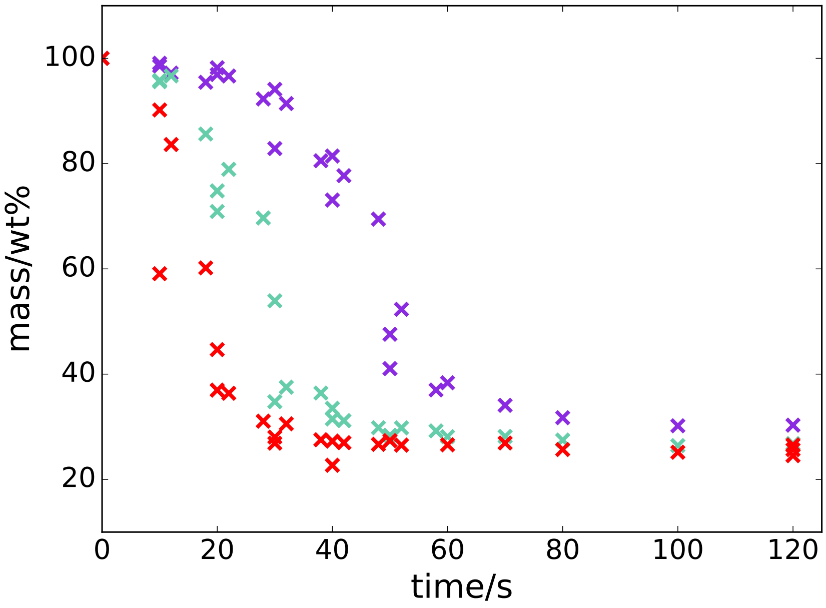

Figure 4.4: Measured mass loss of a pellet subjected to pyrolysis at different reactor temperatures: 500°C (purple), 600°C (green) and 700°C (red).

Figure 4.5 shows the measured inner temperatures of a pellet undergoing pyrolysis for different reactor temperatures. The initial particle temperature seems to be different for each reactor temperature, that is because the particle is first introduced into a glass container attached to the reactor to sweep away all the oxygen before being introduced into the reactor, but from that position it already receives some heat. Depending on the reactor temperature, the particle will reach a different initial temperature before being introduced into the reacting area. The particle temperature nearer the surface increases steeply from the beginning, reaching the reactor temperature earlier than at the center, where the temperature starts increasing after a delayed period of time in which the heat travels from the surface to the center. In the experimental data reported

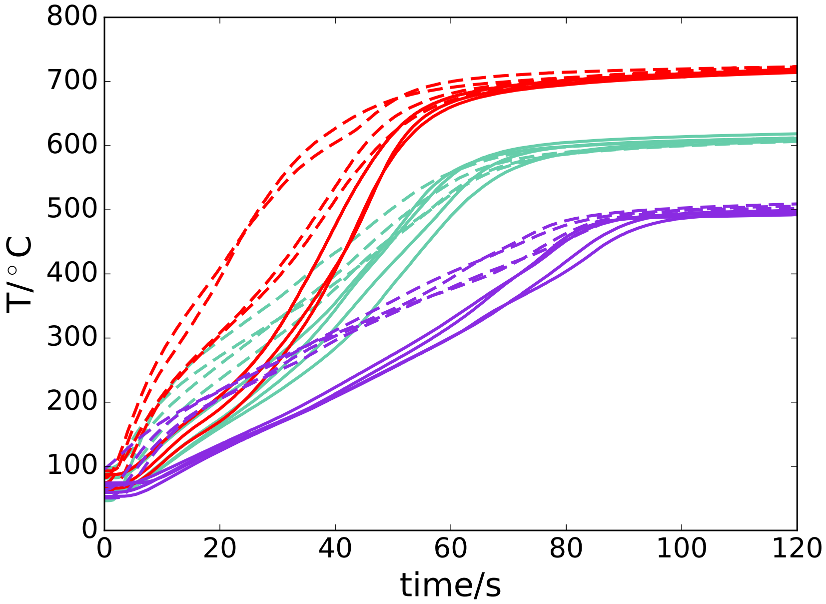

Figure 4.5: Measured inner temperatures of a pellet subjected to pyrolysis at different locations: center (solid line) and at 2 mm from the surface (dashed line), and for different reactor temperatures: 500°C (purple), 600°C (green) and 700°C (red).

by Haseli et al. [134], despite their particle being much larger, the same trend can be observed. The steeper the temperature gradient inside the particle, the smaller is its thermal conductivity and the Biot number becomes larger.

A first shoulder is visible for the curves at 2 mm for all the reactor temperatures, but perhaps is more visible at the reactor temperature of 500°C. This shoulder reflects a steep increase of temperature for a period of time of about 10 s at the beginning of pyrolysis, and it is probably caused by a localized increase of thermal convection and thermal radiation due to the damaged pellet surface at the area of insertion of the thermocouple.

It should be noted that the variability of the measured data is probably due to the use of a different pellet for each experiment, which entails a natural variability in the wheat straw material, the variability of the thermocouple manual insertion and the possible changes in room temperature in the laboratory from day to day.

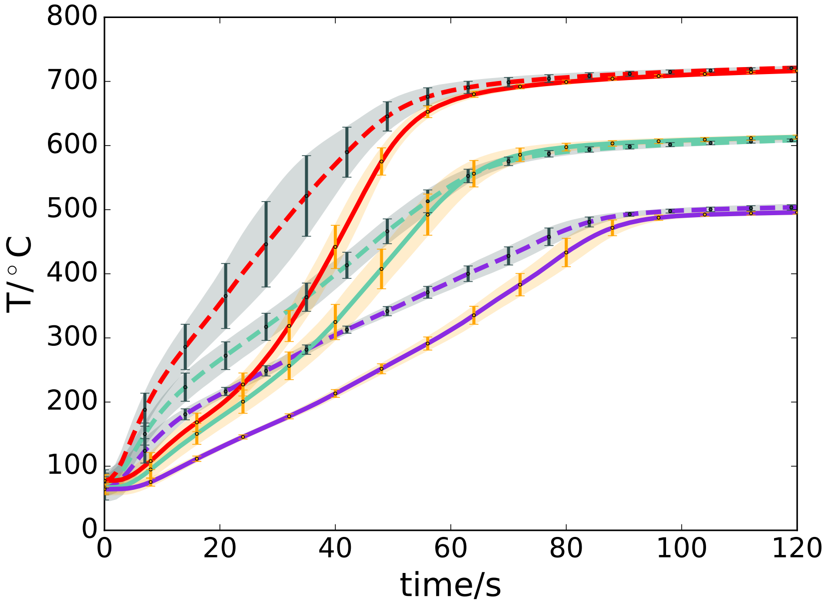

Figure 4.6: Mean and standard deviation of the measured inner temperatures of a pellet subjected to pyrolysis at different locations: center (solid line) and at 2 mm from the surface (dashed line), and for different reactor temperatures: 500°C (purple), 600°C (green) and 700°C (red).

Figure 4.6 shows the mean of the experimental curves showed in Fig. 4.5 with their respective standard deviation. It is clear that at a higher reactor temperature there is a steeper temperature increase and the the variability of the measured data increases. From the information given in this figure it could be concluded that more repetitions at the higher reactor temperatures is advisable, and that it is difficult to adjust the single particle model by using only the measured temperature at high reactor temperatures. The temperature at 2 mm from the surface shows a larger standard deviation than the temperature at the center of the particle, that could also be a consequence of the breakage of the surface of the particle.

4.3 Measured temperature and gas emissions during oxidative pyrolysis

Biomass oxidative pyrolysis consists mainly of two main stages, in addition to the water evaporation step in the beginning. The stages are biomass devolatilization and char oxidation, which might even happen simultaneously at high temperatures [165]. The biomass devolatilization stage is the same process as pyrolysis, however pyrolysis does not include the stage of char oxidation, which requires the presence of some amount of oxygen. Work on oxidative pyrolysis shows how the oxygen might also have an effect at the devolatilization stage. For small particles at high temperatures, the devolatilization time is shorter in comparison with pyrolysis, given that the volatiles released combust near the particle releasing heat, which in turn contributes to heating more the particle [166]. This extra source of heat also affects the products yields, enhancing the gas yield [167]. Kinetic studies of oxidative pyrolysis can be found for cellulose [168], hemicellulose [169] and with the combination of cellulose, hemicellulose and lignin [170].

Figure 4.7 shows the measured center temperature of a pellet undergoing pyrolysis and the center temperature of a pellet undergoing oxidative pyrolysis. From this figure we can observe that the temperature in oxidative pyrolisis is

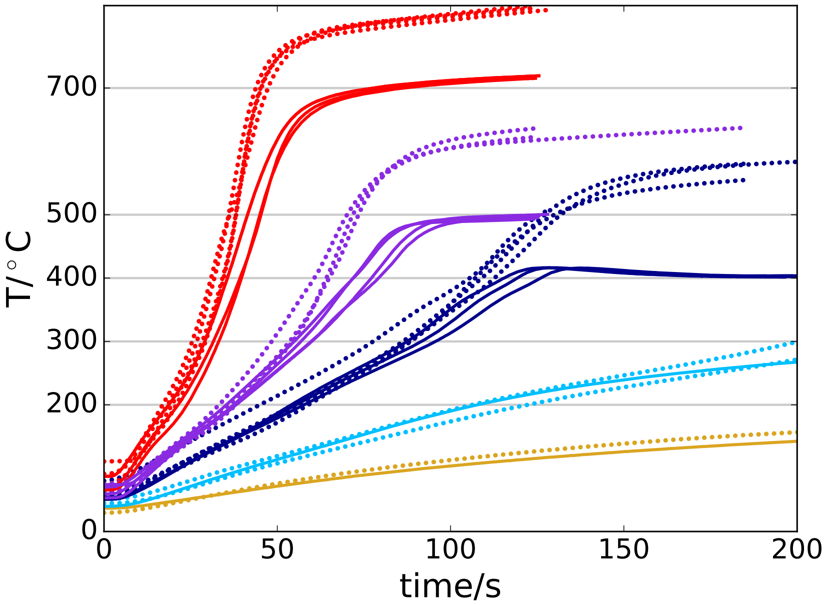

Figure 4.7: Center temperature of a pellet subjected to pyrolysis (solid line) and oxidative pyrolysis (dotted line) for different reactor temperatures: 200°C (yellow), 300°C (cyan), 400°C (dark blue), 500°C (purple) and 700°C (red).

higher than with pyrolysis. That is possibly due to the partial combustion of the volatiles released, which generate heat near the particle and contribute to its heating. The ignition temperature can be identified when the pyrolysis and the oxidative pyrolysis curves diverge from each other. The ignition temperature of this biomass could be placed between 300 and 400°C, because it can be observed that for the reactor temperature of 300°C at 200 s, pyrolysis is just starting because there is a very small increase in the center temperature of oxidative pyrolysis with respect to the pyrolysis curve, due to the combustion of the volatiles released during the pyrolysis stage. An ignition temperature of 400°C was also established for cylindrical wheat straw pellets of 18 mm diameter [158]. The curve for the reactor temperature of 200°C, on the other hand, does not show any difference between the center temperature of pyrolysis and oxidative pyrolysis, meaning that there has been no release of volatiles or that the volatiles released did not combust near the particle.

The center temperature of pyrolysis at 400°C shows a small peak or shoulder just before it stabilizes to the reactor temperature. When this happens, the rate of heat release is higher than the rate of heat transfer. It is believed to be caused by exothermic reactions happening just before all the devolatilization reactions finish, that is why it is associated with the decomposition of a solid intermediate into a solid product [93]. The exothermic reaction causing the peak, might be related to char formation, which is favoured at low heating rates [171]. After the peak, the particle temperature reaches equilibrium with the reactor temperature due to thermal convection [134].

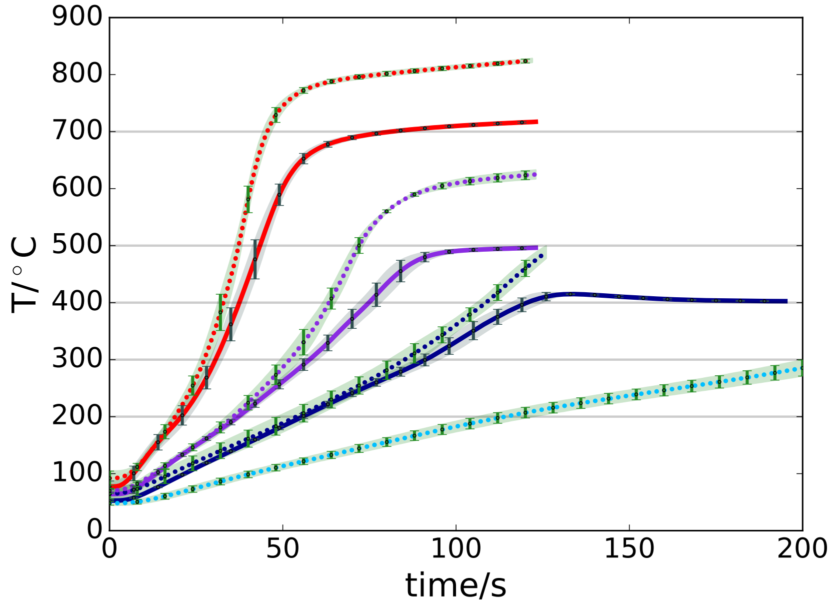

Figure 4.8: Mean and standard deviation of the measured center temperature of a pellet subjected to pyrolysis (solid line) and oxidative pyrolysis (dotted line) for different reactor temperatures: 200°C (yellow), 300°C (cyan), 400°C (dark blue), 500°C (purple) and 700°C (red).

Figure 4.8 shows the mean of the multiple measured center temperature curves given in Fig. 4.7 and the corresponding standard deviation. The measurements that did not have multiple repetitions were left out of this plot because a standard deviation could not be calculated. The beginning of the heating period and the end have a very low standard deviation, and the larger standard deviation is observed when there are steep changes in temperature in a short time. This information allows us to assess how precise needs the model prediction to be; At the reactor temperature of 300°C the closest model approximation to the experimental data is desired, but at higher reactor temperatures the model precision can be less strict during the heating period.

Figure 4.9 shows the rate of carbon monoxide and carbon dioxide emissions with time for different reactor temperatures. Carbon dioxide emissions in oxidative pyrolysis are higher than what the device was calibrated for, that is why it appears to be off the chart, and the emissions for the reactor temperature of 600°C were only recorded for pyrolysis. The tail of the CO_2 curves for oxidative pyrolysis is due to the slow oxidation of the remaining char.

It should also be mentioned that, according to Fig. 4.7, a pellet pyrolysed at 700°C is able to reach a slightly higher temperature than the reactor temperature. Going back to Fig. 4.9, it can be observed that at a temperature of 700°C, the amount of CO_2 release spikes up. It is clear that at high temperatures there might be exothermic reactions causing the overheating of the particle, and those reactions might be related to the dense volatile released, transforming further into light volatiles. Secondary pyrolysis reactions are reported to be very exothermic [172, 173].

The general emissions trend is that there is more generation of CO and CO_2 in oxidative pyrolysis, but at the reactor temperature of 700°C, there is more CO production for the process of pyrolysis than in oxidative pyrolysis.

From the study of pyrolysis of coal using CO_2 as a carrier gas, it was found that the CO_2 could be considered inert below 400°C [174]. The same study found that the temperature at which the devolatilization started was the same as with using N_2 as a carrier gas, but the rate of generation of volatiles was increased. Another study on biomass pyrolysis at temperatures between 600 and 1000°C also used CO_2 instead of N_2 as a carrier gas during pyrolysis of microalgae, and they found that it enhanced the production of CO, overall decreasing the bio-oil fraction in favour of the gas fraction [175]. The enhancement of the CO yield is more pronounced at the temperatures between 600 and 800°C [175]. This can be explained by the Boudouard reaction ($C + CO_2 \rightarrow 2CO$) that favours the CO formation at temperatures above 700°C [176].

The Boudouard reaction could also explain why the CO rate is higher in pyrolysis compared to oxidative pyrolysis for the temperature of 700°C (see Fig. 4.9a). At that temperature the CO_2 generated during pyrolysis might partly react with the char to form more CO. But in oxidative pyrolysis, the CO, which is a combustable gas, will react with the amount of O_2 available, generating more CO_2; The results are summarized in Fig. 4.9b. The oxidative pyrolysis of pinewood at 500°C showed that the process can reach autothermal operation due to the energy released from the char partial oxidation, and also from the partial oxidation of the combustable gases in the volatile phase, such as CO and other hydrocarbons [101]. In the oxidative pyrolysis at 700°C, part of the generated CO reacts with O_2 to form CO_2, which in turn might increase the CO generation from the biomass, which will later react with O_2.

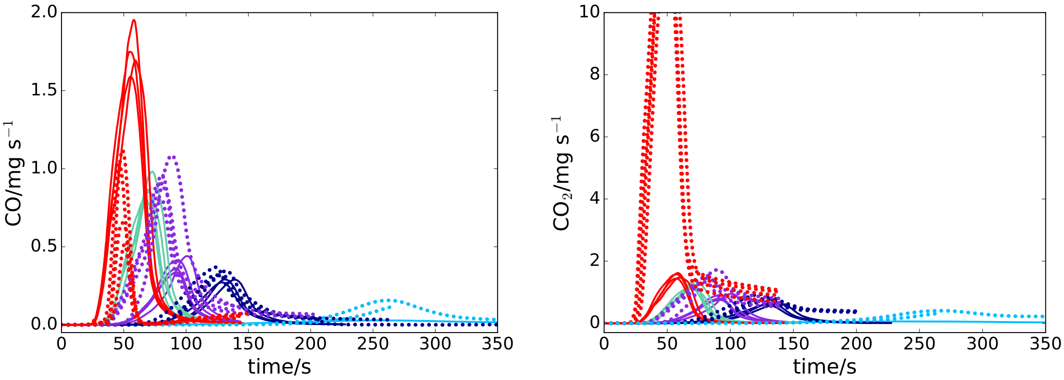

(a) CO emissions

(b) CO_2

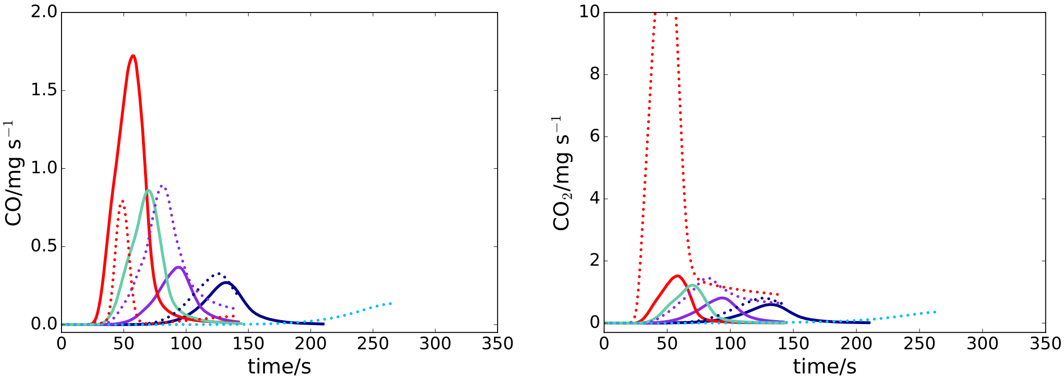

(c) Mean CO emissions with the following standard deviation for an increasing order of temperature: 0.01, 0.02, 0.03 and 0.04 mg s^{-1} (pyrolysis); 0.006, 0.02, 0.06 and 0.03 mg s^{-1} (oxidative pyrolysis).

(d) Mean CO_2 emissions with the following standard deviation for an increasing order of temperature: 0.02, 0.05, 0.04 and 0.04 mg s^{-1} (pyrolysis); 0.01, 0.04, 0.1 and 0.3 mg s^{-1} (oxidative pyrolysis).

Figure 4.9: Measured carbon emissions from the pyrolysis (solid line) and oxidative pyrolysis (dotted line) of a wheat straw pellet for the reactor temperatures of 300°C (cyan), 400°C (blue), 500°C (purple), 600°C (green) and 700°C (red).

The area under the curve was calculated from the average value of emissions given in Fig. 4.9c and 4.9d to determine the total amount of carbon dioxide and carbon monoxide released during pyrolysis (see Table 4.3). Note that the total amounts calculated for carbon dioxide in oxidative pryolysis are smaller than the actual amount, because the experimental data were recorded up to a certain time, when the carbon dioxide release was not complete. Additionally, there was a limit on how much the device could detect, so in the case of the reactor temperature of 700°C the maximum rate of release was beyond the measurement bounds.

The amount of CO in oxidative pyrolysis increases with reactor temperature until the reactor temperature of 500°C, then at the reactor temperature of 700°C it decreases to a level similar to the CO yield at the reactor temperature of 300°C.

Table 4.3: Carbon monoxide and carbon dioxide emissions from pyrolysis and oxidative pyrolysis.

Species/mg	300°C	400°	500°	600°	700°
CO (pyrolysis)	4.7	11.3	13.4	26.4	49.4
CO (oxidative)	11.2	17.1	36.4	-	12.9
CO_2 (pyrolysis)	11.5	28.9	31.7	39.5	44.3
CO_2 (oxidative)	50.5	53.9	82.8	-	395.2

4.4 Calculated temperature and mass loss using a lumped model

A lumped pyrolysis model assuming a small biomass particle and an instantaneous internal heating, meaning that the temperature inside the particle is homogeneous everywhere, has been used to compare it with the experimental data of the pyrolysis of a wheat straw pellet. The purpose of this comparison is to establish if a lumped model is sufficient, or if the particle is large enough that it requires a model that accounts for the internal heating gradients. The kinetic mechanism used in this work is explained later in Fig. 5.1 and consists of four reactions (r_1, r_2, r_3, r_4) and four components, including wheat straw and activated wheat straw (biomass B), char C, and volatile V (gas G + tar T).

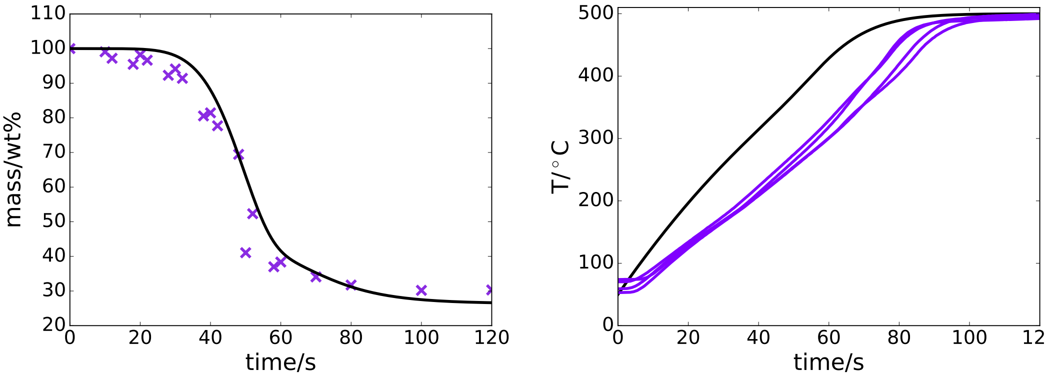

(a) (b)

Figure 4.10: Measured mass loss (purple) and measured center temperature (purple) comparison with a lumped model (black) for the reactor temperature of 500°C.

Figure 4.10 compares the experimental results from the pyrolysis of a wheat straw pellet with a lumped model [177], based purely on the chemical kinetics. In this particular case we do not account for the heat of reaction. The lumped model should not properly render the decomposition of a thick biomass particle, because it assumes there is no gradient of temperature inside. However, as we can see in Fig. 4.10a, the calculated mass loss curve seems to agree quite well with the experimental data. One possible reason for this, is that the kinetic mechanism was determined from TG experiments of biomass that was not completely in the thermally thin regime. Nevertheless, the delayed decomposition, which starts at about 30 s, can also be caused by a delayed heating time of the particle surface instead of an internal temperature gradient. The time required to heat the surface of the particle might be higher than the time required to heat internally. This is also corroborated by the comparison of the calculated convective and conductive time-scales.

The time-scale of a particle heating by conduction is calculated using the thermal diffusivity coefficient, $\alpha_T = \frac{\lambda}{\rho C_p}$, which taking into account the size of the particle, gives $t = \frac{CL^2}{\alpha_T} = 30\,s$. The parameters used are C_p = 2000 J kg^{-1} K^{-1} (heat capacity), ρ = 1000 kg m^{-3} (specific density), λ = 0.11 W m^{-1} K^{-1} (thermal conductivity) and the dimensions of the cylindrical pellet are a diameter of 0.007 m, a length of 0.01 m, and CL stands for characteristic length.

The time-scale for convective heating in a lumped system analysis is given by $t = \frac{\rho C_p V}{hA} = 260\,s$, where V is the particle volume, A is the particle surface area, and h is the convective heat transfer coefficient. A value of 10 W m^{-2} was used for the heat transfer coefficient, the value was picked to be between 5 W m^{-2}[178] and 20 W m^{-2}[71]. The heat transfer coefficient is calculated in Chapter 5 for a more complex pyrolysis model, giving also a value around 10 W m^{-2}. As can be appreciated, the convection time-scale is larger than the conduction one, explaining the slow decomposition at the beginning.

If we look at the comparison of the experimental center temperature and the lumped temperature in Fig. 4.10b, it can be observed that the lumped temperature starts heating immediately and the experimental center temperature needs more time for the heat to reach the center and start increasing the temperature. From this, it can be concluded that the lumped model is not sufficient to have a good understanding of the pyrolysis of a thermally thick particle, because the predicted lumped temperature does not match the measured center temperature, meaning that the temperature distribution is not captured. The numerical simulation of biomass pyrolysis aims not only to predict the mass loss, but to improve the accuracy of the product yields prediction, specially the amounts and species in the volatile product, and its composition strongly depends on the temperature distribution of the pellet.

4.5 Conclusions

The experimental data of pyrolysis of a wheat straw pellet displayed an expected behaviour with respect to what has been previously reported in the literature for similar biomass and conditions. However, interesting information has been obtained in reference to which type of experimental conditions and procedure would yield the most useful data in order to understand and model the process. Interesting thermochemical processes observed, were the conditions in which overheating of the pellet can take place, the range of temperatures in which devolatilization and ignition starts, and carbon dioxide and carbon monoxide interactions with oxygen at high temperature.

From the comparison of the center temperature profiles of pyrolysis and oxidative pyrolysis, it has been found that the ignition temperature of wheat straw pellets is placed between 300 and 400°C. The center temperature with oxidative pyrolysis is higher than the center temperature with pyrolysis because in oxidative pyrolysis there is extra heat around the particle due to the partial combustion of the volatiles released from the particle that react with the available oxygen in the reactor.

An unexpected behaviour of the inner temperature profile of a pellet at the location of 2 mm from the surface has been observed. The steep temperature slope during the first 10 s after the temperature curve starts increasing cannot be explained by pyrolysis reactions, therefore it is concluded that the insertion of the thermocouple can make an impact on the temperature reading caused by the physical damage of the pellet when inserting the thermocouple. Other studies have used a solid wood particle with a clean perforation to insert the pellet, but when working with straw pellets any attempt of perforating the pellet would entail a certain degree of surface breakage around the thermocouple insertion. Alternative methods to hold the sample could also be investigated to find out how it affects the heating of the particle.

The experimental results obtained in this work corroborate the potential presence of an inner temperature peak or shoulder above the reactor temperature when certain conditions are given, like an increased heat release from the pyrolysis reactions in comparison with the heat lost to the reactor environment in combination with a slow inner heating rate that allows for the peak to be visible (as observed for pyrolysis at the reactor temperature of 400°C).

The comparison of gas emissions from pyrolysis and oxidative pyrolysis have shown some interesting results with respect to the generation of carbon monoxide and carbon dioxide at the reactor temperature of 700°C. For reactor temperatures below 700°C the general trend was more generation of carbon monoxide and carbon dioxide in oxidative pyrolysis, but at the reactor temperature of 700°C, there was more carbon monoxide production for the process of pyrolysis. A plausible explanation for this behaviour is that at that temperature the carbon dioxide generated might react with the char to produce more carbon monoxide. The steep increase in carbon dioxide in oxidative pyrolysis also for the temperature of 700°C might be caused by the partial combustion of the carbon monoxide generated during devolatilization, producing more carbon dioxide, that at the same time might increase the release of carbon monoxide.

Finally a lumped model was used to model the process, and it was concluded that a lumped model is not suitable to predict pyrolysis of large biomass particles, because it only renders kinetics and not transport phenomena, which is relevant in the case of a wheat straw pellet of the given dimensions. Instead, a single particle model is required to reliably predict the pyrolysis behaviour of thick biomass particles.

Chapter 5

Mathematical description of the single particle model

This chapter defines and analyses the pyrolysis of a single biomass particle with mathematical equations, making the necessary transformations and adjustments to the equations in order to be able to solve them. The single particle model is then used to obtain the results presented in the remaining chapters.

5.1 Kinetic mechanism

The reaction mechanism proposed by Lanzetta et al. [177] is selected because it was determined for the same type of biomass as in the single particle experiments performed in this work (wheat straw). The kinetic model was determined for milled and dried wheat straw, using a very thin layer of biomass of 100 μm. According to their sample size, their experiments should exclude

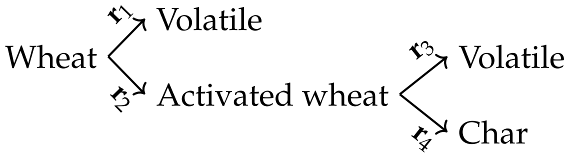

Figure 5.1: Diagram of the kinetic mechanism.

Table 5.1: Kinetic parameters of wheat straw pyrolysis [177].

Parameter	$\mathbf{r}_1$	$\mathbf{r}_2$	$\mathbf{r}_3$	$\mathbf{r}_4$
A (s^{-1})	$1.1{\cdot}10^5$	$1.2{\cdot}10^3$	$1.2{\cdot}10^3$	2.82
E (kJ mol^{-1})	75.1	53.55	66.53	27.61

any heat and mass transfer limitations. They used a very rapid heating and kept the sample at a given temperature in the range of 400 and 648 K, and used the information from the weight loss versus time to elucidate a two stage kinetic mechanism. The experiments were considered isothermal because a quick heating rate of 25-27 K s^{-1} was used. This mechanism was chosen because the type of biomass used is the same, and because the kinetics determined from fine biomass particles could be considered as the intrinsic kinetics.

The diagram of the kinetic mechanism can be found in Fig. 5.1 and the values of the kinetic parameters in Table 5.1. It starts from a single component, that decomposes with parallel, multi-step and first-order reactions. The four reactions are: wheat straw decomposes into volatiles (r1) and activated wheat (r2); the activated wheat then reacts further to form more volatiles (r3) and char (r4).

5.2 System description

To describe the pyrolysis of a single biomass particle, the system is defined as a porous particle, because biomass is a porous material. The particle consists of a solid phase and porosity, which is represented by a void fraction ε.

The effect of the reactor on the particle is represented with the surface boundary conditions imposed on the particle. The main reactor effects captured are the temperature of the reactor environment T_∞, and the media in the reactor environment, which is nitrogen flowing through the reactor and taking away all the vapour products released from the particle. The release of volatiles is regulated by Darcy's law, which depends on the internal pressure gradient of the particle and on its permeability κ.

In this model we assume that the solid and the vapour phase are in thermal equilibrium, therefore there is only one variable for the particle temperature T that represents both, the solid and the vapour phase. The energy balance accounts for the surface heating of the particle according to a given reactor temperature by heat convection and thermal radiation. Then the heat is transferred from the surface of the particle to its center by conduction. The heat of reaction might also influence the particle temperature depending on its exothermicity.

The evolution of the mechanism components during pyrolysis is described with the mass balance. Another component that is not included in the reaction mechanism but is present in the system is nitrogen, which is initially present in the particle before it is displaced by the volatile generated. The nitrogen release follows the same principles as the volatile release, therefore its evolution is rendered with the same mass balance. Also, in this model it is assumed that there is only primary pyrolysis taking place, and not secondary reactions of the volatiles with char or with other volatiles.

The values of the parameters used in the single particle model are obtained from the literature or determined for the given conditions. The convective heat transfer coefficient is determined with

$$h = \frac{Nu\,\lambda_{N_2}}{CL} \tag{5.1}$$

where CL is the particle characteristic length, for a spherical or cylindrical particle, the particle diameter could be used instead, λ_{N_2} is the thermal conductivity of nitrogen, because nitrogen is the carrier gas used in the reactor, and Nu is the Nusselt number, which has been determined using the Churchill-Bernstein correlation [179]

$$Nu = 0.3 + \frac{0.62\,Re^{\frac{1.0}{2.0}}\,Pr^{\frac{1.0}{3.0}}}{\left[1 + \left(\frac{0.4}{Pr}\right)^{\frac{2.0}{3.0}}\right]^{\frac{1.0}{4.0}}} \left[1 + \left(\frac{Re}{282000}\right)^{\frac{5.0}{8.0}}\right]^{\frac{4.0}{5.0}} \tag{5.2}$$

where Pr is the Prandtl number and Re is the Reynolds number. This correlation is used to determine the Nusselt number of a cylinder in a convective flow that causes heat transfer between the body and the flow. It is valid for a wide range of Pr and Re as long as Pr×Re is larger or equal to 0.2. The Prandtl number is a dimensionless number used in systems where there is heat transfer between a particle and a carrier gas, is defined as

$$Pr = \frac{C_{p,N_2}\,\mu_{N_2}}{\lambda_{N_2}} \tag{5.3}$$

where μ_{N_2} is the dynamic viscosity of nitrogen, and the heat capacity and thermal conductivity also refer to the carrier gas. The Reynolds number is

$$Re = \frac{\rho_{N_2}\,\mathbf{v}_{N_2}\,d_p}{\mu_{N_2}} \tag{5.4}$$

where $\mathbf{v_{N_2}}$ is the velocity calculated from the nitrogen flow rate and the cross-sectional area of the reactor. Since the density of nitrogen changes with temperature, the resulting Reynolds number and heat transfer coefficient will also vary with temperature. The range of Re in this problem is between 3.6 and 6.7, and Pr is 0.795, which makes the choice of Nusselt number correlation suitable.

Table 5.2 gives the values of the parameters used in the SPM, some of them are determined from the experimental work and others are taken from the literature or determined from given correlations. d_p is the diameter of the cylindrical pellet used in the experimental work, $\rho_{s,0}$ is the initial particle bulk density, and T_0 is the initial particle temperature which corresponds to the measured temperature of the particle when it is in the lateral arm of the reactor before being introduced in the center of the reactor, that is why for each reactor temperature

Table 5.2: Thermophysical properties used in the single particle model.

Parameter	**Value or expression**	
d_{particle} (m)	0.007	
$\rho_{s,0}$ (kg m^{-3})	780	
ε_0	0.22	
T_0 (K) (T_∞ = 200)	35	
T_0 (K) (T_∞ = 300)	40	
T_0 (K) (T_∞ = 400)	50	
T_0 (K) (T_∞ = 500)	60	
T_0 (K) (T_∞ = 600)	70	
T_0 (K) (T_∞ = 700)	70	
$C_{p,B}$ (J kg^{-1} K^{-1})	$2300 - 1150e^{-0.0055T}$	[28]
$C_{p,C}$ (J kg^{-1} K^{-1})	$1430 + 0.355T - 7.3210^7T^{-2}$	[28]
$C_{p,G}$ (J kg^{-1} K^{-1})	$770 + 0.629T + 1.91 \cdot 10^{-4}T^2$	[178]
$C_{p,T}$ (J kg^{-1} K^{-1})	$-100 + 4.4T - 1.57 \cdot 10^{-3}T^2$	[178]
$C_{p,V}$ (J kg^{-1} K^{-1})	$0.85C_{p,T} + 0.15C_{p,G}$	[93]
λ (W m^{-1} K^{-1})	$\lambda_{cond} + \lambda_{rad}$	[71]
	$\lambda_{cond} = \varepsilon\lambda_V + \frac{\rho_B}{\rho_{B,0}}\lambda_B + (1 - \frac{\rho_B}{\rho_{B,0}})\lambda_C$	
	$\lambda_V = 0.026$	[180] as in [71]
	$\lambda_B = 0.11$ or $\lambda_B = 0.15$	[181] as in [71]
	$\lambda_C = 0.071$	[181] as in [71]
	$\lambda_{rad} = \frac{\varepsilon\sigma T^3 d_{\text{pore}}}{\epsilon}$	
	$\epsilon = 0.9$	[71]
	$d_{\text{pore}} = 3.2 \cdot 10^{-6}$	[71]
κ (m^{-2})	$\frac{\rho_B}{\rho_{B,0}}\kappa_B + (1 - \frac{\rho_B}{\rho_{B,0}})\kappa_C$	
	$\kappa_B = 5 \cdot 10^{-16}$	[140]
	$\kappa_C = 10^{-13}$	[140]
μ_{N_2} (Pa s)	$3.5 \cdot 10^{-5}$	
MW_{N_2} (kg mol^{-1})	0.028	
λ_{N_2} (W m K^{-1})	0.04	

Table 5.3: Estimated initial values of some model parameters for the different reactor temperatures.

Parameter	**200°C**	**300°C**	**400°C**	**500°C**	**600°C**	**700°C**
λ_0 (W m^{-1} K^{-1})	0.1165	0.1165	0.117	0.117	0.117	0.117
α_0 (m^2 s^{-1})	$7.1{\cdot}10^{-8}$	$7.1{\cdot}10^{-8}$	$7.1{\cdot}10^{-8}$	$7{\cdot}10^{-8}$	$7{\cdot}10^{-8}$	$7{\cdot}10^{-8}$
Re_0	6.7	5.5	4.7	4.1	3.6	3.2
Nu_0	1.6	1.5	1.4	1.3	1.3	1.2
h_0 (W m^{-2} K^{-1})	9.2	8.5	8	7.6	7.2	7

the initial particle temperature is different.

The initial pellet porosity is determined with information about the particle density (specific density) of wheat straw, which, using a pycnometer has a value of about 1100 kg m^{-3} [100] and 983 kg m^{-3} [182]. In this work a mean value of 1000 kg m^{-3} was used. The initial porosity is calculated as ε_0 = 1-$\frac{\rho_{\text{specific}}}{\rho_{\text{bulk}}}$, where the ρ_{bulk} is the bulk density which includes the porosity, and it can be easily measured from the pellet size and the pellet weight, and ρ_{specific} is the specific density which would be the particle's density without including the porosity.

Heat capacity is described by correlations that depend on the temperature, each component has a different heat capacity. And the heat capacity of the volatile (V) is determined by a linear combination of the heat capacities of tar (T) and gas (G). Thermal conductivity is also a correlation that depends on the individual thermal conductivities of the components, and it also includes the influence of the thermal radiation λ_{rad} assuming a constant pore size d_{pore}. The permeability depends on how the solid fraction changes.

The initial values of the determined heat transfer coefficient, Reynolds number, Nusselt number and thermal conductivity are given in Table 5.3 to have an idea of their order of magnitude. Each of them is determined for all the reactor temperatures that have been used in the experimental work. The parameter $\alpha = \frac{\lambda_0}{\rho_{s,0}\, C_{p,B,0}}$ that also appears in the table, is the thermal diffusivity of the solid phase.

According to Mason et al. [183] the thermal conductivity of wheat straw pellets of a density of about 1149 - 1165 kg m^{-3} should be in the order of 0.15 - 0.16 W m^{-1} K^{-1}. The thermal conductivity for biomass determined in this work using a three dimensional model of the pellet is about 0.11 W m^{-1} K^{-1} for all the reactor temperatures, which is smaller than the measured value found by Mason et al.

5.3 Governing equations

The variables in this model are the species in the solid phase, the species in the vapour phase, porosity, pressure inside the particle, velocity of the vapour phase, and temperature, assuming that solid and vapour are in thermal equilibrium.

The conservation of the solid species is given by

$$\frac{\partial \rho_{s,i}}{\partial t} = \sum_r \nu_{r,i} \frac{\partial \xi_r}{\partial t}, \tag{5.5}$$

where $\rho_s = \sum_i \rho_{s,i}$ is the density of the solid phase including any individual solid species, $\nu_{r,i}$ is the stoichiometric coefficient of the species i in the reaction r and ξ_r is the extent of reaction, defined as

$$\frac{\partial \xi_r}{\partial t} = k_r(T) f(\rho_s) \tag{5.6}$$

where $f(\rho_s)$ is the rate law, which in this case is a first order reaction that describes the decomposition of the solid biomass, and $k_r(T)$ is the temperature dependent Arrhenius constant

$$k_r(T) = A_r e^{\frac{-E_r}{RT}}, \tag{5.7}$$

where A_r (pre-exponential factor) and E_r (activation energy) are the kinetic parameters referring to the reaction r, R is the gas constant and T is the absolute temperature.

The conservation of the vapour species includes the generation of volatiles and the mass convection of the vapour species, which is much more dominant than the volatiles diffusion, and for that reason, the mass diffusion term is usually neglected [136]. The resulting mass balance is

$$\frac{\partial}{\partial t}(\varepsilon\rho_{v,i}) + \nabla \cdot (\rho_{v,i}\mathbf{u}) = \sum_r \varepsilon\nu_{r,i}\frac{\partial \xi_r}{\partial t} \tag{5.8}$$

where $\rho_v = \sum_i \rho_{v,i}$ is the density of the volatile phase, $\rho_{v,i}$ is the density of the volatile species i, ε is porosity, and $\mathbf{u}$ is the vapour phase velocity, defined by Darcy's law

$$\mathbf{u} = \frac{-\kappa}{\mu}\nabla P \tag{5.9}$$

where κ is permeability, μ viscosity and P is vapour phase pressure in the pore. Assuming that the gas phase behaves like an ideal gas, the pressure can be calculated using the ideal gas law

$$P = \frac{\rho_v RT}{MW_v}. \tag{5.10}$$

where MW_v is the mean molecular weight of the volatile and the nitrogen according to their respective fractions.

The porosity is defined as

$$\varepsilon = 1 - (1 - \varepsilon_0)\frac{\rho_s}{\rho_{s,0}}. \tag{5.11}$$

The conservation of energy includes the heat generation from the reactions, heat convection from the volatile release, and heat conduction. Heat transfer due to the volatiles diffusion is considered not to be significant [140], so it is not included in the energy balance, which is

$$(\rho_s C_{p,s} + \varepsilon \rho_v C_{p,v})\frac{\partial T}{\partial t} + \mathbf{u}\rho_v C_{p,v} \cdot \nabla T - \nabla \cdot (\lambda \nabla T) = -\sum_r \Delta H_r \frac{\partial \xi_r}{\partial t} \tag{5.12}$$

where λ is the particle overall thermal conductivity, $C_{p,s}$ is the heat capacity of the solid phase, $C_{p,v}$ is the heat capacity of the vapour phase, and ΔH_r is the enthalpy of the reaction r. This expression can also be written as

$$\sum_i (\rho_{s,i} C_{p,i} + \varepsilon \rho_{v,i} C_{p,i})\frac{\partial T}{\partial t} + \mathbf{u}\sum_i \rho_{v,i} C_{p,i} \cdot \nabla T - \nabla \cdot (\lambda \nabla T) \tag{5.13}$$

$$= -\sum_r H^s_{r,i} \nu^s_{r,i} \frac{\partial \xi_r}{\partial t} + \sum_i H^s_{r,i} \nu^v_{r,i} \varepsilon \frac{\partial \xi_r}{\partial t} \tag{5.14}$$

where $H^s_{r,i}\nu^s_{r,i}$ and $H^v_{r,i}\nu^v_{r,i}$ refer to the enthalpy of reaction of the solid phase and volatile phase respectively.

The initial conditions are

$$\rho_{B,0} = \rho_{s,0} \tag{5.15}$$

$$\rho_{C,0} = 0 \tag{5.16}$$

$$\rho_{V,0} = \rho_{V,\infty} = 0 \tag{5.17}$$

$$\rho_{v,0} = \rho_{N_2} = \frac{P_0}{R\,T_0} MW_{N_2} \tag{5.18}$$

$$P_0 = P_\infty = P_{atm} \tag{5.19}$$

where $\rho_{B,0}$ corresponds to the initial bulk density of the particle, and initially the only solid component is wheat straw; $\rho_{V,0}$ is the initial volatile density, which is zero; $\rho_{v,0}$ is the initial vapour phase density, which consists only of nitrogen, MW_{N_2} is the molecular weight of nitrogen; And P_0 is the initial pressure of the particle, which corresponds to the reactor pressure and is equal to the atmospheric pressure (101325 Pa). The initial values of the parameters T_0, $\rho_{s,0}$ and ε_0 were already given in Table 5.2.

At the surface of the particle a Neumann boundary condition is used for the temperature

$$-\hat{n} \cdot \lambda \nabla T = h(T - T_\infty) + \epsilon\sigma(T^4 - T_\infty^4) \tag{5.20}$$

where $\hat{n}$ is a normal vector to the surface, h is the heat transfer coefficient, T_∞ is the reactor temperature, ϵ is the emissivity of the particle, and σ is the Stefan-Boltzmann constant.

Also at the surface, a Dirichlet boundary condition is used to fix the value of the pressure at atmospheric pressure, which is necessary when using Darcy's flow to regulate the release of volatiles from the particle to the surroundings. Another assumption is that the volatiles move from the center to the surface of the particle in a symmetrical manner, therefore the velocity of the volatiles at the center of the particle is zero. These two boundary conditions can be expressed as

$$P(r = R) = P_{atm} \tag{5.21}$$

$$\mathbf{u}(r = 0) = 0 \tag{5.22}$$

where r is a position inside the particle, R is a position at the surface of the particle, and $r = 0$ is at the center of the particle.

The conservation of energy is originally given as a derivative of the enthalpy, but is generally used in the form of a derivative of temperature. The transformation of the energy balance can be found in Appendix A.

The system is defined with a porous particle, but the porous particle could have different shapes with different levels of symmetry. If we assume a more symmetrical system, the equations are simplified and their numerical solution is less computationally expensive. The one-dimensional axisymetrical formulation of the governing equations is

$$\frac{\partial}{\partial t}(\varepsilon\rho_{v,i}) + \frac{1}{r^n}\frac{\partial}{\partial r}\left(r^n\rho_{v,i}\mathbf{u_r}\right) = \sum_r \nu_{r,i}\frac{\partial\xi_r}{\partial t} \tag{5.23}$$

where $\mathbf{u_r}$ is the velocity in the radial direction, and the value of n depends on the desired particle shape, $n = 1$ for a cylindrical particle and $n = 2$ for a spherical particle, the conservation of energy

$$(\rho_s C_{p,s} + \varepsilon\rho_v C_{p,v})\frac{\partial T}{\partial t} + \mathbf{u_r}\rho_v C_{p,v}\frac{\partial T}{\partial r} - \frac{1}{r^n}\frac{\partial}{\partial r}\lambda\, r^n\frac{\partial T}{\partial r} = -\sum_r \Delta H_r\frac{\partial\xi_r}{\partial t} \tag{5.24}$$

$$\begin{aligned}&\sum_i(\rho_{s,i}C_{p,i} + \varepsilon\rho_{v,i}C_{p,i})\frac{\partial T}{\partial t} + \mathbf{u_r}\sum_i\rho_{v,i}C_{p,i}\frac{\partial T}{\partial r} - \frac{1}{r^n}\frac{\partial}{\partial r}\left(\lambda\, r^n\frac{\partial T}{\partial r}\right)\\ &= -\sum_r\sum_i H^s_{r,i}\nu^s_{r,i} + \sum_r\sum_i H^v_{r,i}\nu^v_{r,i}\end{aligned} \tag{5.25}$$

and the velocity

$$\mathbf{u_r} = \frac{-\kappa}{\mu}\frac{\partial P}{\partial r}. \tag{5.26}$$

5.4 Dimensional analysis

The dimensionless form of the governing equations is given in this section. Nondimensionalization has been carried out in order to simplify the solver solution when comparing orders of magnitude and also to compare the relative importance of the different terms in the governing equations, to know which processes are more significant.

The conservation of the solid species is modified as

$$\frac{\partial \bar{\rho}_{s,i}}{\partial \bar{t}} = \sum_r \nu_{r,i} \bar{A}_r e^{\frac{-\bar{E}_r}{\bar{T}}} \bar{\rho}_s \tag{5.27}$$

where the parameters with a bar over the letter mean that they are dimensionless parameters. Their definition is given in Table 5.4, where τ is the same as $\bar{t}$.

The conservation of the volatile species is modified as

$$\frac{\partial}{\partial \bar{t}}(\varepsilon \bar{\rho}_{v,i}) + \bar{\nabla} \cdot (\bar{\rho_{v,i}} \bar{\mathbf{u}}) = \sum_r \nu_{r,i} \bar{A}_r e^{\frac{-\bar{E}_r}{\bar{T}}} \bar{\rho}_s \left(\frac{\rho_{s,0} R T_0}{P_0} \right). \tag{5.28}$$

The momentum equation that describes the velocity of the volatiles is also modified

$$\begin{aligned} \bar{\mathbf{u}} &= -\frac{\kappa_0 \, \tau \, P_0}{\mu \, d_p^2} \, \bar{\kappa} \bar{\nabla} \bar{P} \\ \bar{\mathbf{u}} &= -\frac{\kappa_0 \, P_0}{\mu \, \alpha_0} \, \bar{\kappa} \bar{\nabla} \bar{P} \end{aligned} \tag{5.29}$$

and the pressure, which is given by the ideal gas law equation is now

$$\bar{P} = \bar{\rho_v}\bar{T}. \tag{5.30}$$

The conservation of the energy is

$$\begin{aligned}
&(\bar{\rho_s}\bar{C}_{p,s} + \varepsilon\bar{\rho_v}\frac{P_0}{\rho_{s,0}\,R\,T_0}\bar{C}_{p,v})\frac{\partial\bar{T}}{\partial\bar{t}} \\
&+ \bar{\mathbf{u}}\,\bar{\rho_v}\frac{P_0}{\rho_{s,0}\,R\,T_0}\bar{C}_{p,v} \cdot \bar{\nabla}\bar{T} - \bar{\nabla} \cdot (\bar{\lambda}\bar{\nabla}\bar{T}) = -\sum_r \frac{\Delta H_r}{T_0\,C_{p,s,0}}\bar{A}_r\,e^{\frac{\bar{E}_r}{\bar{T}}}\,\bar{\rho}_s
\end{aligned} \tag{5.31}$$

and the Neumann boundary condition for the temperature is

$$-\hat{n} \cdot \bar{\lambda}\bar{\nabla}\bar{T} = \frac{h_0\,d_p}{\lambda_0}\,(\bar{T} - \bar{T_\infty}) + \frac{\epsilon\sigma\,d_p\,T_0^3}{\lambda_0}\,(\bar{T}^4 - \bar{T}_\infty^4) \tag{5.32}$$

Table 5.4 gives the definition of the dimensionless parameters that appear in the dimensionless equations, as well as the values used to determine them. The parameter transformation attempts to approximate the parameter values to the unit.

Table 5.5 gives the values of the dimensionless groups for the different reactor temperatures and also it indicates to which equations they are linked. Comparing the dimensionless groups in front of the terms in the energy balance, it can be assessed which are the dominant heat transfer mechanisms. Using the values of the dimensionless groups for the reactor temperature of 700°C

Table 5.4: Parameters and groups used to nondimensionalize the model equations.

Parameter	Value or expression
$\bar{\rho_s}$	$\frac{\rho_s}{\rho_{s,0}}$
$\bar{\rho_v}$	$\frac{\rho_v R T_0}{P_0 MW_v}$
$\bar{T}$	$\frac{T}{T_0}$
$\bar{P}$	$\frac{P}{P_0}$
$\bar{\mathbf{u}}$	$\frac{\tau}{d_p}\mathbf{u}$
$\bar{\nabla}$	$d_p \nabla$
$\bar{\lambda}$	$\varepsilon_0 \, \frac{\lambda_G}{\lambda_0} + \frac{\rho_B}{\rho_{B,0}} \frac{\lambda_B}{\lambda_0} + \left(1 - \frac{\rho_B}{\rho_{B,0}} \frac{\lambda_C}{\lambda_0} + \frac{13.5 \sigma T^3 d_{\text{pore}}}{\epsilon \lambda_0}\right)$
$\bar{A}_r$	τA_r
$\bar{E}_r$	$\frac{E_r}{R T_0}$
$\bar{\kappa}$	$\frac{\rho_B}{\rho_{B,0}} \frac{\kappa_B}{\kappa_0} + \left(1 - \frac{\rho_B}{\rho_{B,0}}\right) \frac{\kappa_C}{\kappa_0}$

Table 5.5: Values of the dimensionless groups of the governing equations.

Group	**200°C**	**300°C**	**400°C**	**500°C**	**600°C**	**700°C**	appears in
$\tau = \frac{\mathrm{d}_\mathrm{p}^2}{\alpha_0}$	685.1	686.8	689.9	692.8	695.5	695.5	-
$\frac{\rho_{s,0} R T_0}{P_0}$	19.7	20	20.7	21.3	22	22	Eq. (5.28)
$\frac{P_0}{\rho_{s,v} R T_0}$	0.05	0.049	0.048	0.047	0.045	0.045	Eq. (5.31)
$\frac{\Delta H_r}{T_0 \, C_{p,s,0}}$	0.078	0.076	0.073	0.07	0.068	0.068	Eq. (5.31)
$\frac{\epsilon \sigma \, d_p \, T_0^3}{\lambda_0}$	0.09	0.094	0.1	0.113	0.123	0.123	Eq. (5.32)
$\frac{h_0 \, d_p}{\lambda_0} = \mathrm{Bi}$	0.55	0.5	0.48	0.46	0.43	0.42	Eq. (5.32)
$\frac{\kappa_0 P_0}{\mu \, \alpha_0}$	4723	4734	4756	4776	4794	4794	Eq. (5.29)

as example, the significance of the terms in the energy balance is compared. The coefficients of heat convection, thermal radiation and the generation of heat from the reactions are 0.42, 0.12 and 0.068 respectively, meaning that the external heating of the particle is dominant over the particle self-heating from the heat of reaction. It also shows that heat convection is dominant over thermal radiation. The term of the heat of reaction contains an exponential, which means that at high temperatures that term might become more influential. The coefficient that appears in front of the volatile terms is very small, 0.045, and it barely changes for the different reactor temperatures. From this observation it can be assumed that the volatile terms do not have a significant impact on the particle temperature, therefore the influence of the volatiles convection in the energy balance could be neglected, and the heat capacity of the volatiles is not as influential as the heat capacity of the solids. The mass convection of the vapour phase is still relevant in the mass balance of the vapour phase, the velocity of the vapour has a coefficient of 4794, and the generation of volatiles has a coefficient of 22, although the generation term has an exponential that depends on the temperature, so its influence will be larger at high temperatures.

Anca-Cuoce et al. [136] acknowledged that the influence of the volatiles convection on the temperature distribution of the particle could be neglected, but it should not be neglected from the volatiles mass balance if the aim of the study is to predict the species in the bio-oil and gas products. Some earlier work attributed to volatiles convection a cooling effect on the particle [140, 89, 184], but the relative importance of the heat transfer mechanisms has also been taken into consideration in this work.

5.5 Numerical method

The finite element method has been used to discretize in space the partial differential equations (PDEs) seen in Sec. 5.3, obtaining first-order ordinary differential equations (ODEs). The resulting ODEs are discretized in time using the Crank-Nicolson method. The discretization with the finite element method consists of breaking the spatial domain into smaller regions of simple geometry called subdomains or finite elements [185]. An example of application is given using the diffusion equation

$$\frac{\partial u}{\partial t} - D\nabla^2 u = 0 \tag{5.33}$$

which depends on space and time.

The finite element method consists of solving the governing equations in the form of weak formulation. A method to do it is the Galerkin method, which consists of finding u by multiplying the original PDE by a test function and integrating over the spatial domain. A solution is found when the integrals are equal to zero.

The variational formulation is

$$F_u = \int \left[\frac{du}{dt} - D\nabla^2 u \right] \psi_i(x)\, dx = 0 \tag{5.34}$$

where ψ_i is a test function. The term with the second order derivative requires integration by parts,

$$F_u = \int \left[\frac{\partial u}{\partial t} \psi_i + D \nabla u \cdot \nabla \psi_i \right] dx - \oint (D \nabla u) \psi_i \, ds = 0 \tag{5.35}$$

and given the boundary condition $\hat{n} \cdot D \nabla u = q$,

$$F_u = \int \left[\frac{\partial u}{\partial t} \psi_i + D \nabla u \cdot \nabla \psi_i \right] dx - \oint q \, \psi_i ds = 0 \tag{5.36}$$

The solution u is constructed with basis functions, which are a piecewise polynomial approximation

$$u(x,t) = \sum_{j=1}^{N} u_j(t) \psi_j(x) \tag{5.37}$$

where j are the elements, u_j are unknown constants, and ψ_j are test functions that are piecewise, in this work they are Lagrange polynomials of first order. Equation (5.37) is included in Eq. (5.36),

$$\sum_{j=1}^{N} \frac{\partial u_j}{\partial t} \int \psi_j(x) \psi_i(x) \, dx + \sum_{j=1}^{N} u_j \int D \nabla \psi_j(x) \nabla \psi_i(x) - \oint q \, \psi_i ds = 0 \tag{5.38}$$

where N is the number of elements. This equation could also be written in the form

$$\sum_{j=1}^{N} M_{i,j}\frac{\partial u_j}{\partial t} + \sum_{j=1}^{N} W_{i,j}u_j - b_i = 0 \tag{5.39}$$

$$\sum_{j=1}^{N} \frac{\partial u_j}{\partial t} + \sum_{j=1}^{N} M_{i,j}^{-1}W_{i,j}u_j - \sum_{j=1}^{N} M_{i,j}^{-1}b_i = 0 \tag{5.40}$$

where $b_i = \oint q\,\psi_i ds$, $M_{i,j} = \int \psi_j(x)\psi_i(x)dx$ and $W_{i,j} = \int D\nabla\psi_j(x)\nabla\psi_i(x)dx$. This is the PDE discretized in space, but it still needs to be discretized in time.

The Crank-Nicolson method is a finite difference method of discretization in time. Equation (5.40) has the shape of a ODE, to make it more clear it can be rewritten using $f(u_j, t) = -M_{i,j}^{-1}W_{i,j}u_j + M_{i,j}^{-1}b_i$,

$$u_j' = f(u_j, t) \tag{5.41}$$

where $u' = \frac{\partial u}{\partial t}$ and f is a nonlinear function of u_j, Crank-Nicolson approximates $f(u_j, t)$ with an arithmetic mean

$$\frac{u_j^{n+1} - u_j^n}{\Delta t} = \theta\left[f(u_j^n, t_n)\right] + (1-\theta)\left[f(u_j^{n+1}, t_{n+1})\right] \tag{5.42}$$

where t_n refers to the previous time, and t_{n+1} would be the current time, determined as $t_{n+1} = t_n + \Delta t$ for a given time-step Δt, $u_j^n = u_j(t_n)$ and $u_j^{n+1} = u_j(t_{n+1})$. The solution at the previous time is determined from a known initial solution or from a previous solution to the model, and the solution at the current time is determined from the previous solution. Forward Euler method would involve only the previous time-step, and backward Euler method only the current time-step. Using the Second-order Crank-Nicolson method, θ is $\frac{1}{2}$

$$\frac{u_j^{n+1} - u_j^n}{\Delta t} = \frac{1}{2}\left[f(u_j^n, t_n) + f(u_j^{n+1}, t_{n+1})\right]. \tag{5.43}$$

Rearranging back into matrices form, similar to Eq. (5.40)

$$\sum_{j=1}^{N} \int M_{i,j} \frac{u^{n+1} - n^n}{\Delta t} + \sum_{j=1}^{N} \frac{1}{2}\left[\int W_{i,j} u_j^n - q + \int W_{i,j} u_j^{n+1} - q\right] = 0 \tag{5.44}$$

The final system of linear equations is solved using FEniCS open-source software [186]. The variational formulation of the governing equations used in this work is given in Appendix B.

5.6 Model implementation and benchmarking

In this section the numerical solution of the SPM is validated with the analytical solution of one-dimensional problems of heat transfer. Additionally, the results from lumped (zero-dimensional), one-dimensional and three-dimensional models, using different particle shapes (sphere, finite cylinder and infinite cylinder) are compared in order to choose the best combination depending on the purpose of study.

The governing equations are numerically solved for a given geometry. In this work, the three-dimensional mesh used describes a cylinder of mesh resolution of 30 and consists of 25663 tetrahedral elements with 4831 vertices (see Fig. 5.2), and the time step is 0.001 s. The higher the mesh resolution, the more refined is the mesh and higher the number of elements. The one-dimensional mesh used has a resolution of 20, which consists of 20 intervals and 21 vertices, and the time step is 10^{-5} s, but the time-step is automatically reduced by half when the numerical calculation has to render a more abrupt change in temperature in a shorter time. The order of the smallest time-step reached is 10^{-8} s. The mesh resolution in the case of a one-dimensional mesh, means that the value of resolution is the number of intervals in the mesh.

In this section, simplified mathematical expressions included in the single particle model have been used to validate the model implementation and to study the mass convection process, and different resolutions and time-steps have also been assessed. The respective model resolutions are mentioned for each figure that includes numerical results. More specifically, in this section the heat transfer model is validated with analytical and with lumped model solutions for different particle shapes and for different Biot numbers. After that, solutions from lumped and three-dimensional models are compared to see the impact of the particle thickness on the inner particle heating.

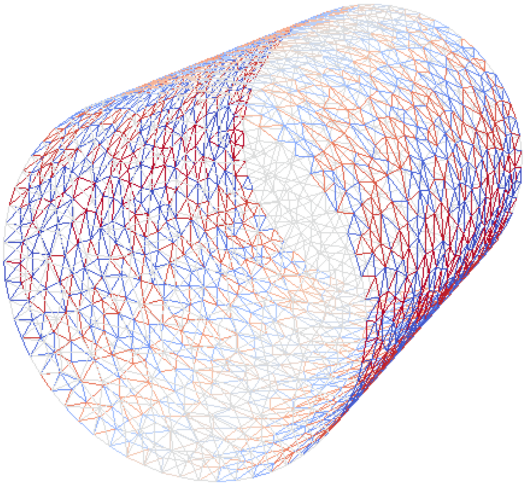

Figure 5.2: Three-dimensional mesh wireframe. The different colors and transparency are just to have a clearer look of the shape.

A simplified heating model involving only heat convection and heat conduction has been numerically solved and compared with the analytical solution and with the lumped model solution in order to validate the model implemented with the finite element method.

The analytical solutions are for transient one-dimensional heat conduction and for an infinite cylinder or a sphere with a given temperature at the surface. One analytical solution describes the evolution of the temperature with time at the center of a sphere or at the center of an infinite cylinder, and the other analytical solution also describes the temperature evolution with time but at different positions along the radius of the sphere/cylinder.

The analytical solution is the one-term approximation that describes the temperature at the center of spherical and cylindrical particles, and is defined as

$$\frac{T(t) - T_\infty}{T_0 - T_\infty} = A_1 e^{-\lambda_1^2 \tau^*} \tag{5.45}$$

where A_1 and λ_1 are functions of the Biot number and their values are interpolated from the transient temperature charts (Heisler charts) depending on the geometry of the conduction body [88], and τ^* is the dimensionless time defined as $\frac{\alpha\, t}{r^2}$, where r is the radius and α is the thermal conductivity. The one-term approximation describing the temperature profile across the radius of a spheric particle for a given time is

$$\frac{T(r) - T_\infty}{T_0 - T_\infty} = A_1 e^{-\lambda_1^2 \tau^*} \frac{sin(\lambda_1 \frac{R}{R_0})}{\lambda_1 \frac{R}{R_0}} \tag{5.46}$$

where R is the position along the radius, and R_0 is the outer radius.

In the lumped model, the increase of the energy of the particle is equal to the heat transferred to the body as follows

$$\rho C_p\, V \frac{dT}{dt} = -A\, h\, (T - T_\infty) \tag{5.47}$$

where V is volume and A is area. After rearranging, including the thermal radiation and the heat of reaction

$$\frac{dT}{dt} = \frac{-A\, h}{\rho C_p\, V}(T - T_\infty) - \frac{A\, \sigma \epsilon}{\rho C_p\, V}(T^4 - T_\infty^4) - \sum_r \frac{d\xi_r}{dt} \frac{\Delta H_r}{\rho C_p} \tag{5.48}$$

where $\frac{d\xi_r}{dt}$ is the extent of the reaction r, and its corresponding heat of reaction is ΔH_r. For each different particle shape, the area and the volume change accordingly, and for an infinite cylinder, their relationship is $\frac{2}{R}$.

The parameters used in the benchmarking and analysis of the heat transfer

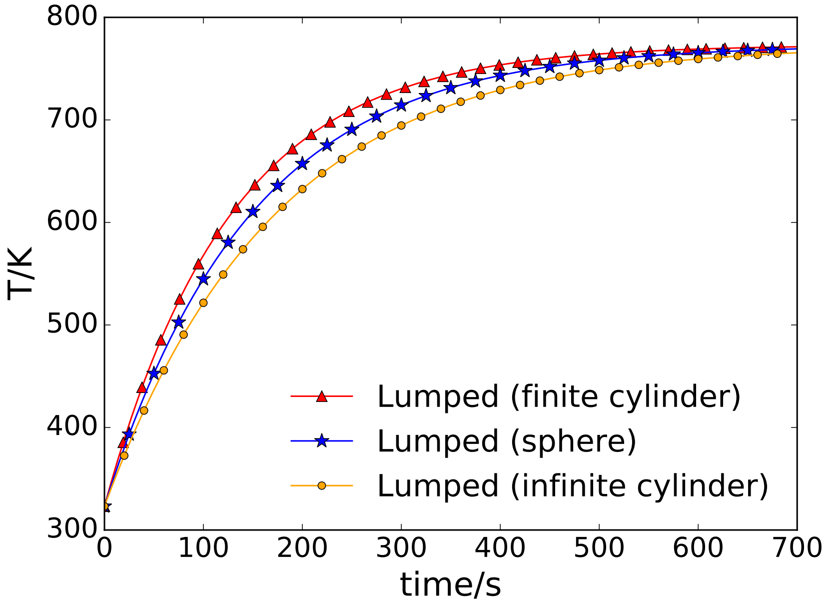

Figure 5.3: Temperature comparison of different particle shapes heating by convection with a lumped model. Sphere (blue), finite cylinder (red) and infinite cylinder (yellow).

model are ρ = 1000 kg m^3, C$_p$ = 2000 J kg^{-1} K^{-1}, h = 20 W m^{-2} K^{-1}, an initial temperature of 323.15 K, a T_∞ of 773.15 K, the particle radius for a cylinder is 3.5 mm and the particle radius for a sphere of the same volume is 4.5 mm. The Biot number is defined as $Bi = \frac{h\,CL}{\lambda}$, where CL is the characteristic length of the particle. The calculations with Bi = 0.01 have a large thermal conductivity constant of 7 W m^{-1} K^{-1} for an infinite cylinder, and 9 W m^{-1} K^{-1} for a sphere, and the results are comparable with a lumped model. The simulations with Bi = 0.6 have a smaller thermal conductivity of 0.117 W m^{-1} K^{-1} for an infinite cylinder, and 0.15 W m^{-1} K^{-1} for a sphere, keeping the value of the heat transfer coefficient constant.

Figure 5.3 shows how the center of different particle shapes heats by convection using the lumped model. The finite cylinder has a radius of 3.5 mm and a length of 10 mm, the infinite cylinder has a radius of 3.5 mm and the sphere has a radius of 4.5 mm preserving the volume of the finite cylinder. The finite cylinder is the first to heat because it has the larger surface area, after that is the sphere and finally the infinite cylinder. The finite cylinder and the sphere receive heat from all sides, but the infinite cylinder receives heat only radially. In this work a finite cylinder has been used for the simulations in three-dimensions of the single particle model, but in one-dimension, a finite cylinder is not possible, therefore a spherical shape has been chosen.

Particles of Biot number smaller than 0.1 are considered to be in the thermally thin regime in which there is no significant temperature gradient inside the particle. Figure 5.4 compares how a particle of Bi = 0.01 is heated by convection with the three-dimensional numerical model, the lumped model and the one-term approximation solution. In Fig. 5.4a the particle has a spherical shape and the three models perfectly match one another. Figure 5.4b represents the heating of a finite and an infinite cylinder, in this case, the three-dimensional numerical model and the one-term approximation do not match because the first is calculated with a mesh depicting a finite cylinder and the one-term approximation is calculated for an infinite cylinder, but the lumped model can match either of them depending on how we define the area and volume of the cylinder.

Figure 5.4a also compares two particles heating by convection, one with a small Biot number, which means that there is no temperature gradient inside the particle, and the other with a larger Biot number that shows a delayed heating of the particle. The analytical solution matches the three-dimensional solution in both cases, and the lumped model is only able to describe pryolysis without a temperature gradient, so it only matches the small Biot number.

Figure 5.5 shows the heating by convection and thermal radiation at the center of the particle for different shapes. The emissivity in the thermal radiation term is 0.9, and values of the heat capacity and the heat transfer coefficient are the same as previously stated. Both particles have the same volume (3.85×10^{-7} m^3) but different shape, in this case the sphere has a radius of 4.5 mm and a surface area of 2.5×10^{-4} m^2, smaller than the surface area of the cylinder with a radius of 3.5 mm and a surface area of 3×10^{-4} m^2. As a result, the sphere heats with a bit of delay after the cylinder. If we were to compare a sphere and a cylinder of the same radius instead of the same volume, then the sphere would heat up more quickly.

Figure 5.6 shows a comparison of the inner heating profile of a spherical particle of Bi = 0.6 with the analytical model and the numerical three-dimensional model. The degree of overlap of the compared solutions is given by the root mean square (RMS). Figure 5.6a shows a good match between both models, and Figure 5.6b shows how important the resolution of the numerical three-dimensional mesh is, higher resolution gives a closer match to the analytical solution.

In this section the particle heating with a numerical model has been validated with analytical and lumped solutions, and for the one and three-dimensions. A cylindrical shape is used in the three-dimensional numerical model because it is the closest representation of a cylindrical pellet, but in the one-dimensional numerical model it has been found that the heating profile of a spherical shape is closer to the three-dimensional cylinder than the one-dimension infinite cylindrical shape. In the following section we focus on the process of mass transfer instead of heat transfer, and the numerical instabilities derived from the process of mass convection are discussed along with a possible stabilization method.

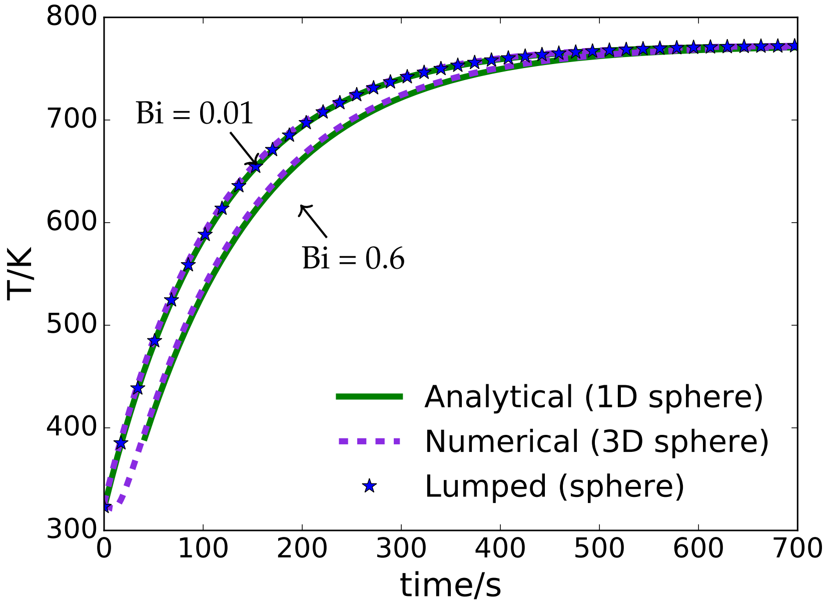

(a) Sphere

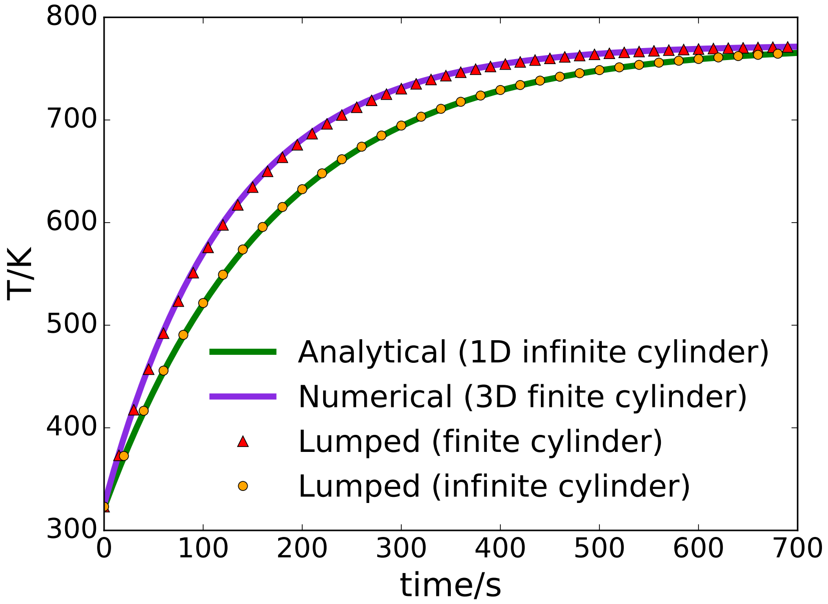

(b) Finite and infinite cylinder

Figure 5.4: Center temperature of particles of different shape and size: (a) sphere with two Biot numbers, (b) cylinder for a Bi = 0.01. One-term approximate solution (green solid line), numerical three-dimensional solution with a mesh resolution of 20 and a time-step of 1 s (purple solid/dashed line) and lumped solution (Eq. 5.47) (star, triangle and circle symbols).

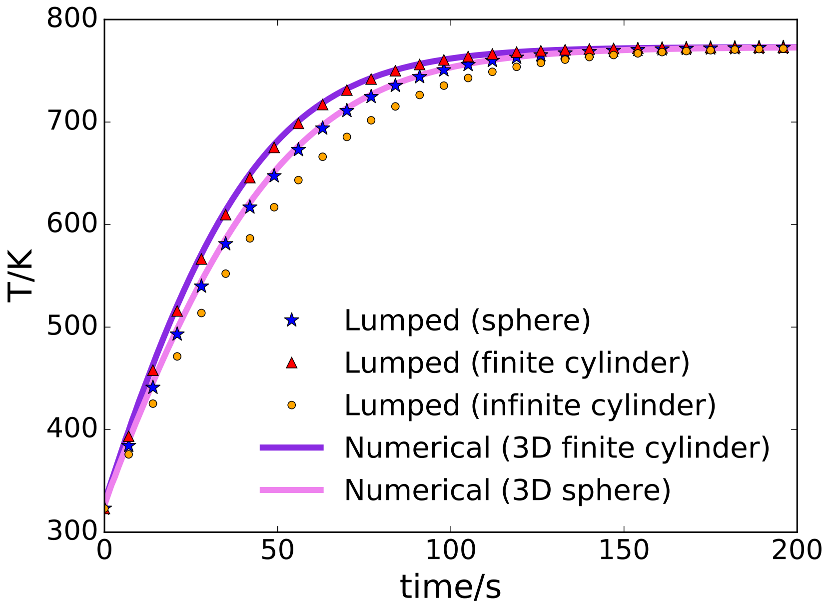

Figure 5.5: Heating comparison of particles of different shape using a lumped and a three-dimensional model with a mesh resolution of 20 and a time-step of 1 s. Lumped model and spherical shape (blue star), lumped model and a finite cylinder shape (red triangle), lumped model and an infinite cylinder shape (yellow circle), numerical model and spherical shape (pink solid line), and numerical model and a finite cylinder shape (purple solid line).

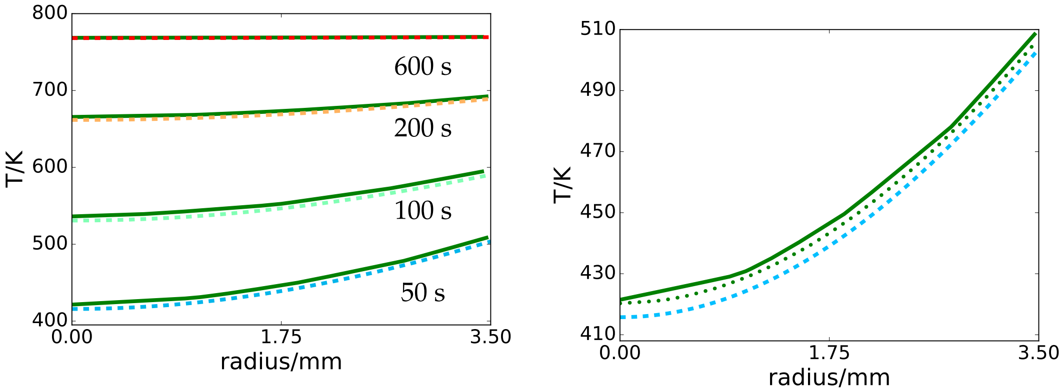

(a) Three-dimensional model with a mesh resolution of 10 (solid line), and the one-term approximation (dashed line). The given times are 50 s (RMS = 7), 100 s (RMS = 6.6), 200 s (RMS = 4.1) and 600 s (RMS = 0.4).

(b) One-term approximation at 50 s (dashed line), three-dimensional model at 50 s with a mesh resolution of 10 (solid line) (RMS = 7), three-dimensional model at 50 s with a mesh resolution of 40 (dotted line) (RMS = 4.2).

Figure 5.6: Internal temperature profile of a sphere of Bi = 0.6 heating by convection using the analytical solution (Eq. 5.46) and the three-dimensional numerical simulation. The profile is from the center (0 mm) to the surface (3.5 mm) and for different given times.

5.7 Mass convection and numerical stabilization

One of the governing equations in the single particle model is a mass balance of the vapour phase. The vapour phase consists of the volatiles generated and the nitrogen that was already in the particle pores before pyrolysis started, but the nitrogen and the volatile species are not accumulated in the particle indefinitely, they are released by mass convection from the particle to the reactor environment.

The process of convection might cause numerical instabilities in some cases where there is a high convective flux, a mesh not sufficiently refined, and a time-step too large for the characteristic time of the given process. The instability of the numerical calculations when dealing with the process of mass convection has been counteracted with a stabilization method, which is presented in this section, along with an analysis of the convection-diffusion equation with respect to their potential instabilities in the results and the effect of the stabilization method.

The convection-diffusion equation [187] for steady-state is

$$\mathbf{u} \cdot \nabla \rho - D \nabla^2 \rho = 0, \tag{5.49}$$

where $\mathbf{u}$ is a vector of velocity, ρ is concentration and D is a constant diffusion coefficient. The same equation in one-dimensional coordinate system is

$$u_x \frac{\partial \rho}{\partial x} - D \frac{\partial^2 \rho}{\partial x^2} = 0. \tag{5.50}$$

Taking into account the Peclet number $Pe = \frac{\mathbf{u}L}{D}$, a particle length L of 1 m and $D = 1 \text{ m}^2 \text{ s}^{-1}$, the previous equation is transformed

$$Pe \frac{\partial \rho}{\partial x} - \frac{\partial^2 \rho}{\partial x^2} = 0. \tag{5.51}$$

The analytical solution for the steady-state with a boundary condition at $x = 0$ of ρ(0) = 1 and at $x = 1$ of ρ(1) = 0 [188] is

$$\rho(x) = \frac{1 - e^{\frac{Pe\, x}{L}}}{1 - e^{Pe}}. \tag{5.52}$$

In this case L = 1 and D = 1, therefore Pe number depends only on **u**. The numerical solution has been calculated using a unit one-dimensional mesh with the following boundary conditions: $\rho(x = 0) = 0$ and $\rho(x = L) = 1$.

The variational formulation of the convection-diffusion equation used for the finite element method is:

$$\int \left(\mathbf{u} \cdot \nabla \rho \, \psi_\rho + D \nabla \rho \cdot \nabla \psi_\rho \right) dx = 0 \tag{5.53}$$

where ψ_ρ is the test function. As we can observe in Fig. 5.7, for a small Pe number the numerical solution coincides with the analytical, independently

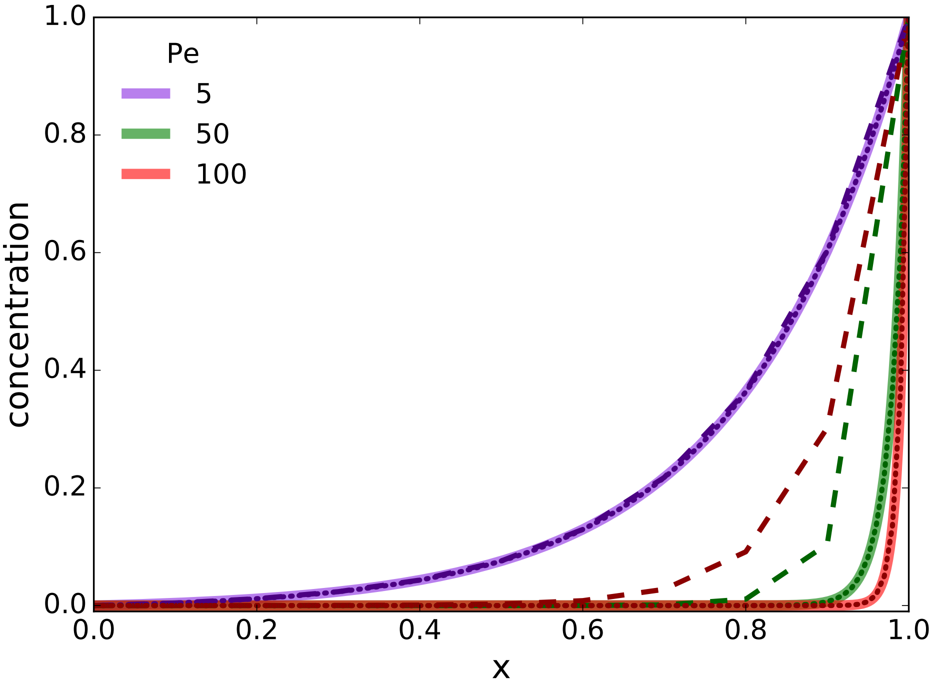

Figure 5.7: Analytical and one-dimensional numerical solution to the convection-diffusion equation for different Peclet numbers. Analytical (solid line); numerical and resolution 10 (dashed line); numerical and resolution 100 (dotted line).

of the mesh resolution. For higher Pe numbers the accuracy of the numerical solution depends on the mesh resolution; the higher the resolution, the closer is the numerical solution to the analytical.

The time-dependent convection-diffusion problem, in general and in one-dimension is

$$\frac{\partial \rho}{\partial t} + \mathbf{u} \cdot \nabla \rho - D \nabla^2 \rho = 0 \tag{5.54}$$

$$\frac{\partial \rho}{\partial t} + Pe \frac{\partial \rho}{\partial x} - \frac{\partial^2 \rho}{\partial x^2} = 0 \tag{5.55}$$

with the corresponding analytical solution

$$\rho(x,t) = \frac{1 - e^{\frac{Pe\,x}{L}}}{1 - e^{Pe}} + \sum_n A_n e^{-\lambda_n t} e^{\frac{Pe\,x}{2}} \sin n\pi x \tag{5.56}$$

where A_n is a coefficient that can be determined from the initial condition, and $\lambda_n = n\pi^2 + \left(\frac{Pe}{2}\right)^2$.

Figure 5.8 shows a comparison between the analytical and the one-dimensional numerical time-dependent solution of the convection-diffusion equation. The values of the coefficients used are A_n = 1 and n = 1 for the initial profile, $\mathbf{u}$ = 5 m s^{-1} and a mesh resolution = 50. It can be observed that at time 0.4 s the analytical and the numerical solution already reached a steady-state value. At the beginning (time 0 s), the analytical and the numerical curves are overlapped, and the analytical solution keeps overlapping with the numerical solution that uses a small time-step (0.02 s) for all given times. The numerical solution for a larger time-step (0.1 s), however, does not match the analytical solution for all times, this indicates that to obtain reliable results from the numerical solution, it is recommendable to use the smaller time-step.

It is important to chose a time-step which makes sense with the rate of the overall process. For a high Pe, to avoid instability, Courant number ($Cr = \frac{\mathbf{u}\Delta t}{\Delta x}$) should be smaller than one. According to the Courant number expression, a higher mesh resolution, which implies that the mesh divisions are going to be smaller, will require a smaller time-step to keep the Courant number small.

The stabilization method used in this work is the Streamline-upwind Petrov/Galerkin (SUPG) [188]. Upwind methods are suitable for convection dominated sys-

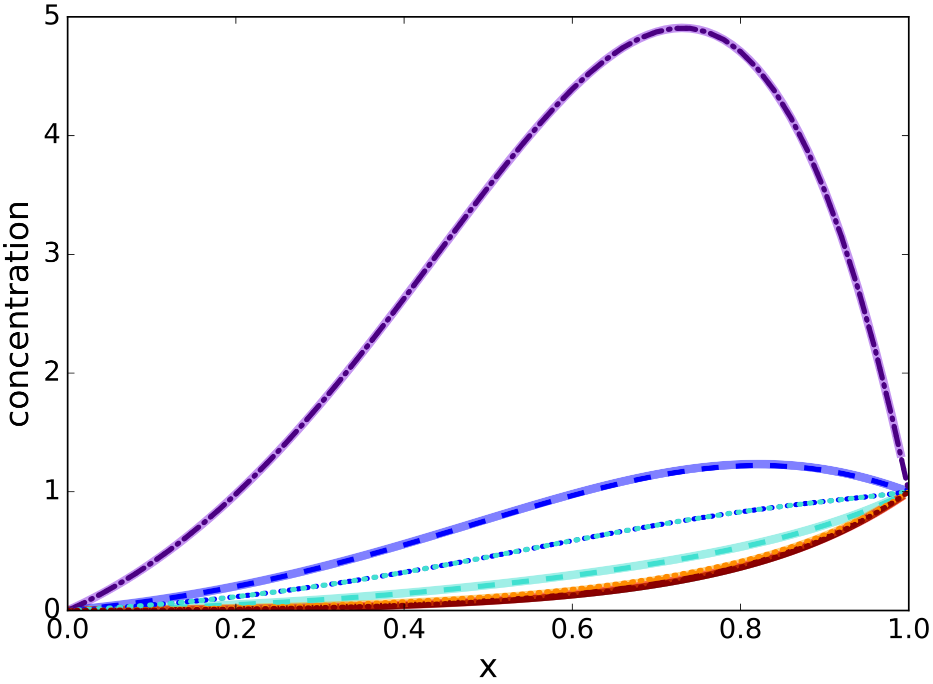

Figure 5.8: Analytical and one-dimensional numerical solution to the convection-diffusion equations for a mesh resolution of 50 and Pe = 5. Analytical time-dependent solutions (coloured solid lines), numerical solutions with a time-step of 0.02 s (dashed lines) and numerical solution with a time-step of 0.1 s (dotted lines). Each color is a different time: 0 s (purple), 0.1 s (blue), 0.2 s (cyan), 0.3 s (orange) and 0.4 s (red).

tems and they are useful when the central difference scheme cannot achieve a convergent solution. The SUPG method focuses on obtaining a more accurate solution upstream. This method has shown to achieve more reliable results in comparison with other upwind methods [188].

The stabilization term is added to the 'projection' term $\psi_{\rho_{v,i}}$ when the volatiles mass balance (Eq. (5.8)) is discretized in space for the FEM formulation

$$\int \frac{\partial}{\partial t}(\varepsilon\rho_{v,i})\, \psi_{\rho_{v,i}} dx + \int (\mathbf{u} \cdot \nabla \text{æ}_{\mathbf{v,i}})(\text{¯}_{\text{æ}_{\mathbf{v,i}}} + \text{ø}_{\mathbf{SUPG}}\, \mathbf{u} \cdot \nabla \text{¯}_{\text{æ}_{\mathbf{v,i}}})\, \mathbf{dx} = \int \,^{\circ}\, _{\mathbf{r,i}} \frac{\boldsymbol{\partial}\,\text{¸}}{\boldsymbol{\partial}\mathbf{t}}\, \text{¯}_{\text{æ}_{\mathbf{v,i}}}\, \mathbf{dx} \tag{5.57}$$

$$\int \frac{\partial}{\partial t}(\varepsilon\rho_{v,i})\, \psi_{\rho_{v,i}} dx + \int (\mathbf{u} \cdot \nabla \text{æ}_{\mathbf{v,i}})\, \text{¯}_{\text{æ}_{\mathbf{v,i}}} \mathbf{dx}$$
$$+ \int (\mathbf{u} \cdot \nabla \text{æ}_{\mathbf{v,i}})(\text{ø}_{\mathbf{SUPG}}\, \mathbf{u} \cdot \nabla \text{¯}_{\text{æ}_{\mathbf{v,i}}})\, \mathbf{dx} - \int \,^{\circ}\, _{\mathbf{r,i}} \frac{\boldsymbol{\partial}\,\text{¸}}{\boldsymbol{\partial}\mathbf{t}}\, \text{¯}_{\text{æ}_{\mathbf{v,i}}}\, \mathbf{dx} = \mathbf{0} \tag{5.58}$$

where τ_{SUPG} is a stabilization constant and it might comprise three terms, one for the convection-dominated case, the transient-dominated, and the diffusion-dominated [189]. In this case diffusion contribution can be neglected because the volatiles transport will be defined by the convection and the small time-scale of the process, so only these two terms are included

$$\begin{aligned} \tau_{SUPG} &= \left(\frac{1}{\tau_{adv}^{m}} + \frac{1}{\tau_{trans}^{m}} \right)^{-\frac{1}{m}} \\ \tau_{SUPG} &= \left(\frac{1}{\left(\frac{h}{2|\mathbf{u}|}\right)^{m}} + \frac{1}{\left(\frac{\Delta t}{2}\right)^{m}} \right)^{-\frac{1}{m}} \end{aligned} \tag{5.59}$$

where m is an integer, in this case the m used is 2 [189].

The full variational formulation of the volatiles mass balance, including the discretization in time, can be found in Appendix B. To illustrate the effect of the stabilization method, the general convection-diffusion equation was used, and the results can be found in Fig. 5.9. The use of a stabilization method

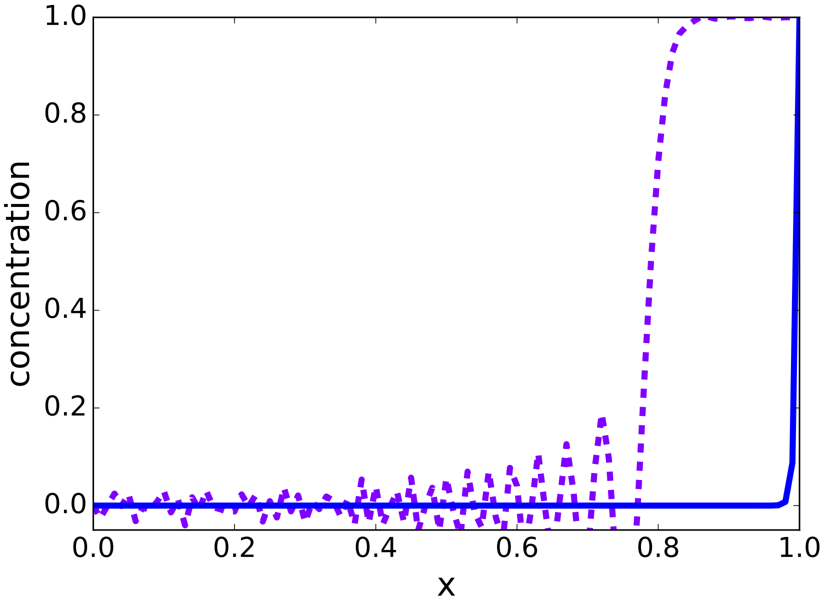

Figure 5.9: Concentration distribution at 0.01 s using a convection-diffusion mechanism with $Pe = 100$, a mesh resolution of 100, a time-step of 1×10^{-5} without any stabilization mechanism (purple) and with SUPG stabilization (blue).

is suitable when additional mesh refinement and additional decrease in time-step does not yield a smooth solution.

5.8 Conclusions

The single particle model has been explained in detail in this chapter, along with a dimensional analysis, validation and preliminary assessment of the model. The dimensional analysis of the single particle model has given very useful information about which transport processes are more relevant in the biomass particle. The value of the dimensionless group referring to the volatile phase in the energy balance is very small, proving that the contribution of the volatiles to the particle temperature is not significant. It was also shown that the dominant heating mechanism of the particle is by external heating over the enthalpy of reaction, and that of the two external heating mechanisms, heat convection is more relevant than thermal radiation.

The numerical solution using the finite element method has been validated with analytical and lumped solutions and for different particle shapes. The way in which the single particle model is implemented gives flexibility to solve the equations in one-dimension or three-dimensions, although for one-dimension some modifications in the system of coordinates are required. A comparison of the one-dimensional and the three-dimensional model was performed in terms of their corresponding heating profiles. The shape of the particle influences the internal heating profile, therefore if the original biomass sample has a cylindrical shape, a three-dimensional cylindrical shape is preferable in the single particle model. If the model requires a simplification in dimensions to save in computational cost, a one-dimension spherical shape is preferable over a one-dimension infinite cylinder if the original biomass sample has the shape of a short cylinder.

This model can also cope with potential numerical instabilities when implementing the mass convection process by using the SUPG stabilization method.

The release of the volatiles generated from the particle to the surroundings has been modelled with Darcy's law, which depends on the pellet internal pressure gradient. Most of the literature assumes a fixed atmospheric pressure at the surface, and that assumption is enough in the case of pyrolysis, but in the case of oxidative pyrolysis, a mass convection mechanism able to account for the penetration of gas from the surroundings towards inside the particle would be required.

Chapter 6

One-dimensional pyrolysis simulations of a single biomass particle

The single particle model described in Chapter 5 is implemented to study the intra-particle heat and mass transfer processes of the pyrolysis of a pellet. Some model parameters are still not well known, like the kinetic mechanism, how the thermophysical properties change with temperature and the enthalpy of reaction. For this reason, the model has been used to perform a parameter sensitivity study and to gain insight into the parameter bounds. It has also been discussed which type of experimental data would be most useful to adjust the model parameters.

The single particle model is generally computed with a one-dimensional model to minimise its computational time. A three-dimensional model could be implemented if the effect of volatiles convection is excluded; If only primary pyrolysis takes place in the particle, the internal temperature distribution of the particle is not greatly affected by the volatiles convection, making a three-dimensional model suitable. However, if secondary pyrolysis takes place in the particle, then the volatiles convection should be included given that the secondary reactions could also contribute to the particle's inner temperature.

The values of the physical constants can be found in Table 5.2. The governing equations of the single particle model are modified with respect to the multi-dimensional equations to represent a one-dimensional sphere, which means that the length of the mesh is the radius of the particle, and a radial heating of the pellet is assumed. The kinetic mechanism [177] explained in Chapter 5 has been assumed. The kinetic mechanism has an impact on the results in terms of when the enthalpy of reaction will influence the temperature of the particle. It also makes an impact indirectly on the mass loss curve and on the thermophysical properties of biomass.

In this chapter the model equations presented in Chapter 5 are implemented in one-dimension, including the process of convective mass transfer, and the model results are compared with the experimental data from Chapter 4 of the pyrolysis of a dry wheat straw pellet.

6.1 Center temperature profile

This section is focused on the pellet center temperature. To model the particle center temperature first the values of the thermo-physical parameters required in the model are selected, in this case the heat capacity of the different components, either raw biomass or pyrolysis products, and their thermal conductivity. The choice of heat capacity and thermal conductivity has more impact during the initial heating phase of the particle. After that, the process of heating/cooling due to the enthalpy of the pyrolysis reactions becomes more relevant. Also, the thermo-physical properties of the raw biomass play a bigger role in the heating phase, they have a stronger effect on the particle heating than the thermal properties of the char, tar or gas, because the products only appear when the particle has already heated to the pyrolysis temperature.

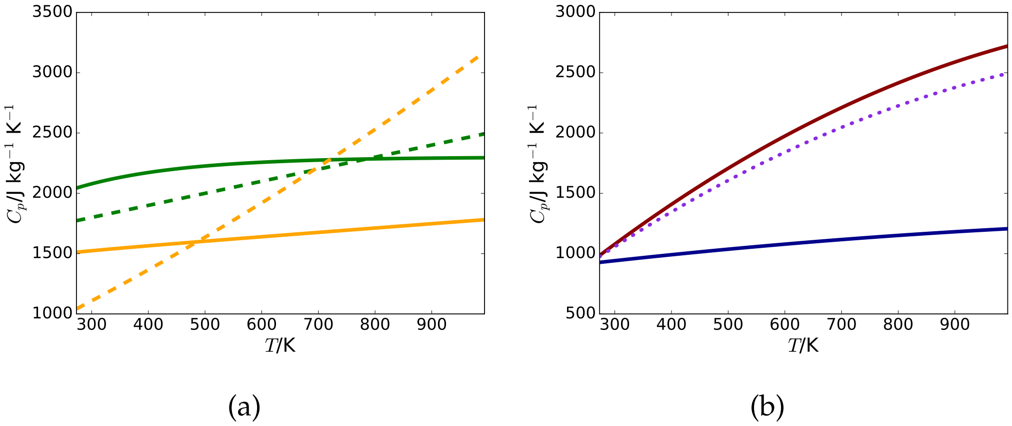

(a) (b)

Figure 6.1: Heat capacity comparison of the different biomass components. (a) Biomass (solid line) and char (dashed line) using the correlation from Blondeau et al. [28] (green) and the correlation from Grønli et al. [131] (yellow). (b) Tar (red solid line), gas (blue solid line) and volatile (dotted purple line) using the correlation from Grønli et al. [131].

The heat capacity correlations used for biomass are shown in Fig. 6.1. The main difference is that the biomass correlation from Blondeau et al. starts with a larger value of heat capacity but its increase with temperature slows down up to a maximum value of heat capacity of 2300 J kg^{-1} K^{-1}. On the other hand, the biomass correlation from Grønli et al. starts from a lower value of heat capacity but it keeps increasing at a constant rate with temperature, being able to reach a higher maximum value. For this study the maximum pyrolysis temperature is 700°C, therefore it is not really much affected by the final value of the heat capacity, however, the initial value of the heat capacity has a significant impact on the temperature profile, because the pyrolysis reactions that generate heat do not start until a certain temperature is achieved, and the main parameters that determine how the particle heats are the thermal convection from surroundings to the particle surface, and the thermal conductivity and heat capacity of the biomass material that define how the heat is transferred across the particle. A larger heat capacity means that the particle temperature will increase more slowly than for a smaller heat capacity. Blondeau et al.'s correlations start with a larger heat capacity, which makes more sense when fitting the current experimental data.

Figure 6.2 shows a comparison of different predicted center temperatures with the experimental data. The different calculated curves use the same mathematical model but different values for heat capacity and thermal conductivity. The experimental center temperature at the reactor temperature of 200°C and for the given time of 200 s did not have time to reach the minimum temperature to start the pyrolysis reactions, which means that with the right combination of heat transfer coefficient, thermal conductivity and heat capacity, we should be able to reproduce the temperature profile. The uncertainty of not knowing if the kinetics mechanism selected is the best possible choice, does not interfere with fitting the thermal properties of the pellet at this temperature. By looking at the figure it can be determined that the thermal conductivity should be lower or/and the heat capacity should be higher than the values compared,

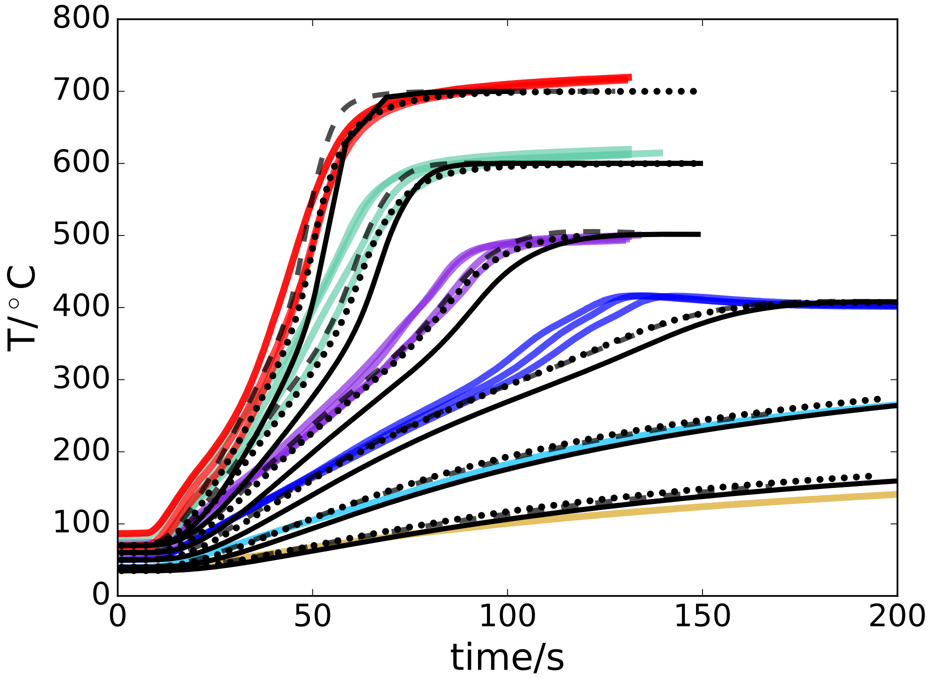

Figure 6.2: Measured center temperature of a pellet at different reactor temperatures: 200°C (yellow), 300°C (cyan), 400°C (dark blue), 500°C (purple), 600°C (green) and 700°C (red); and calculated center temperature using a one-dimensional model and different parameters values: Heat capacity from Blondeau et al. and thermal conductivity 0.11 W m^{-1} K^{-1} (solid line), heat capacity from Blondeau et al. and thermal conductivity 0.15 W m^{-1} K^{-1} (dashed line), and heat capacity from Grønli et al. and thermal conductivity 0.11 W m^{-1} K^{-1} (dotted line).

because the three calculated center temperatures at the reactor temperature of 200°C are above the experimental line. But in that case, the remaining curves at higher reactor temperatures, which already seem to start to decompose a bit later than the experimental, would start to decompose even later. However, the variability of the measured center temperatures should be also taken into account, therefore more repetitions at the low reactor temperatures would be very useful.

The error between the calculated center temperatures using a 1D model and the experimental data can be found in Table 6.1, and it has been calculated with the root mean square as RMS = $\frac{\sum_i^n (y1_i - y2_i)^2}{n}$, where $y1$ and $y2$ are the values to compare from two different curves, i denotes the value at a given time and n is the total number of values. The combination with the smaller RMS for the major number of curves is with λ_B = 0.15 W m^{-1} K^{-1} and the heat capacity correlation from Blondeau et al. [28], which are the parameters that are going to be used to obtain all the following one-dimensional model results.

Table 6.1: Error as root mean square (RMS) for the different reactor temperatures (T_∞) between the experimental data and the the calculated center temperature using 1D and 3D models and different correlations for heat capacity of biomass and char (C_p), and different values of thermal conductivity of biomass (λ_B).

T_∞ (°C)	**RMS (1D)**	**RMS (3D)**	C_p (J kg^{-1} K^{-1})	λ_B (W m^{-1} K^{-1})
200	12	18.1	[28]	0.11
	12.8	23.6	[28]	0.15
	17.4	27.6	[131]	0.11
300	6.8	7.5	[28]	0.11
	5.5	17.9	[28]	0.15
	8.3	20.3	[131]	0.11
400	34.8	20.7	[28]	0.11
	22.2	15.6	[28]	0.15
	22.3	14.6	[131]	0.11
500	39.4	14.3	[28]	0.11
	12.8	18.1	[28]	0.15
	13.7	15.4	[131]	0.11
600	54.2	26.8	[28]	0.11
	25.3	19.3	[28]	0.15
	12.8	18.9	[131]	0.11
700	61.1	23.3	[28]	0.11
	27.1	37.2	[28]	0.15
	17.5	33.6	[131]	0.11
$\sum$	406	372.8		

The purpose of comparing different values of thermo-physical properties is to have a feel of their impact on the particle temperature distribution. The heterogeneity of composition of biomass is one of the main challenges in elucidating a unique kinetic mechanism for all types of biomass, it is expected then, that the biomass heterogeneity also translates into different heating behaviours depending on the material.

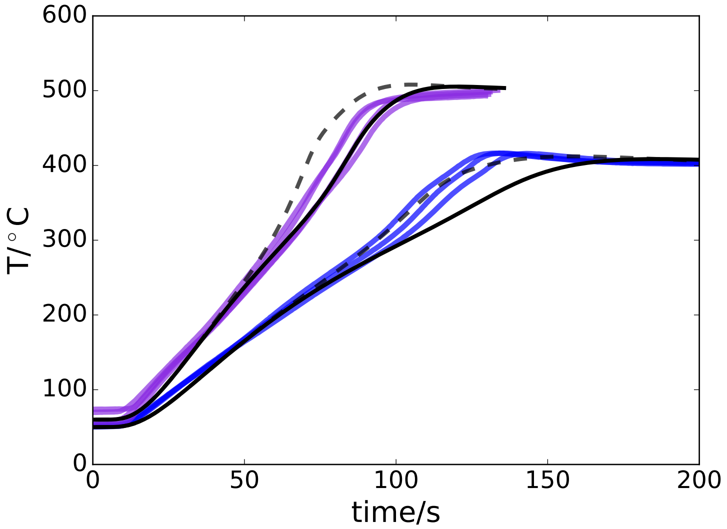

Figure 6.3: Measured center temperature of a pellet at different reactor temperatures: 400°C (dark blue) and 500°C (purple); and measured center temperature using a one-dimensional model and different enthalpy of reaction: ΔH_{r_1}=50, ΔH_{r_2}=0, ΔH_{r_3}=-100 and ΔH_{r_4}=-100 J kg^{-1} (solid line), and ΔH_{r_1}=-100, ΔH_{r_2}=0, ΔH_{r_3}=-100 and ΔH_{r_4}=-100 J kg^{-1} (dashed line).

Referring back to the kinetic mechanism explained in Chapter 5, it consists of four reactions, each reaction is favoured at a different temperature and they can be either exothermic reactions, contributing to a temperature increase, or endothermic reactions, contributing to a temperature decrease in the particle. According to the values of the activation energies, the reactions (r) would happen in the following order: $r4$, $r2$, $r3$ and $r1$, but $r4$ cannot start until the activated wheat is generated from $r2$, this means that as soon as the activated wheat is produced, it will be consumed to produce char. The reactions that generate volatiles are $r1$ and $r3$, and both have a higher activation energy than the other two reactions, which means that if the particle heats up slowly, char formation will be favoured, and if the particle is quickly heated, the generation of the volatile phase might be favoured because there are two reactions able to generate volatile as opposed to only one for char generation.

Depending on which reactions are favoured, the temperature of the particle will be affected by the reactions exothermicity or endotermicity. The selected enthalpies of reaction are based on values from the literature but they are also adjusted to get a better fit of the inner temperature profile of the particle. The enthalpy used in all the calculations with the one-dimensional model is $\Delta H_{r_1} = 50$, $\Delta H_{r_2} = 0$, $\Delta H_{r_3} = -100$ and $\Delta H_{r_4} = -100$ J kg^{-1}.

Figure 6.3 compares the experimental center temperature with the calculated center temperature using different values of enthalpy of reaction. The enthalpies used in this work are compared with a modified enthalpy in which $r1$ is also exothermic. The peak experimentally observed for the reactor temperature of 400°C does not appear at other reactor temperatures and it cannot be reproduced unless the reactions between 100 and 150 s are more exothermic. Several combinations of enthalpy of reaction would be able to predict more closely the experimental data, but all of them involve increasing the exothermicity of the reactions, as seen in this example, which is not compatible with the results from the rest of the reactor temperatures. If the same combination of enthalpies of reaction cannot represent well different reactor temperatures, it might indicate that the kinetic mechanism, the convective heat or some of the model parameters are not completely adequate to render how this particle heats and reacts. The values of the heat capacity and thermal conductivity could be adjusted to allow a diffent value of enthalpy of reaction, but as seen in Fig. 6.2, for the reactor temperatures of 200°C when reactions have not yet started, the heating rate if anything should be slower and not faster. Another potential solution would be to modify the kinetic mechanism so the different reactions become active in a different order.

6.2 Transport of the vapour phase

The internal pressure of the particle increases with increasing temperature, and it also changes with the generation of volatiles inside the particle and their posterior release from it. The pressure and the release of volatiles cannot be measured experimentally, but it has been studied assuming that the vapour phase obeys the ideal gas law, and its motion obeys Darcy's law. The vapour phase includes the initial inert gas filling the particle porosity and the volatiles generated.

Figures 6.4-6.8 show the flux and velocity at different locations in the pellet of the vapour phase leaving the particle, and the pressure also at different locations in the pellet with time. The pressure at the surface of the particle remains at atmospheric pressure throughout the process because that is a boundary condition given to the model and at the center of the pellet is where pressure reaches a maximum value because the volatiles generated at the center take longer to leave the particle than the volatiles generated at a position closer to the pellet surface. The initial pressure in the inner positions of the pellet in Fig. 6.6 seems to be higher than one, but in this case it is possibly due to a numerical instability, because the initial pressure was already given to the model and it was the same as the atmospheric. The velocity and the flux of the vapour phase at the center position is practically zero, because of the assumption of the particle's symmetry of properties and processes, where the permeability of the particle increases starting from the surface and towards the center radially, allowing the flux of the vapour phase to increase as permeability increases.

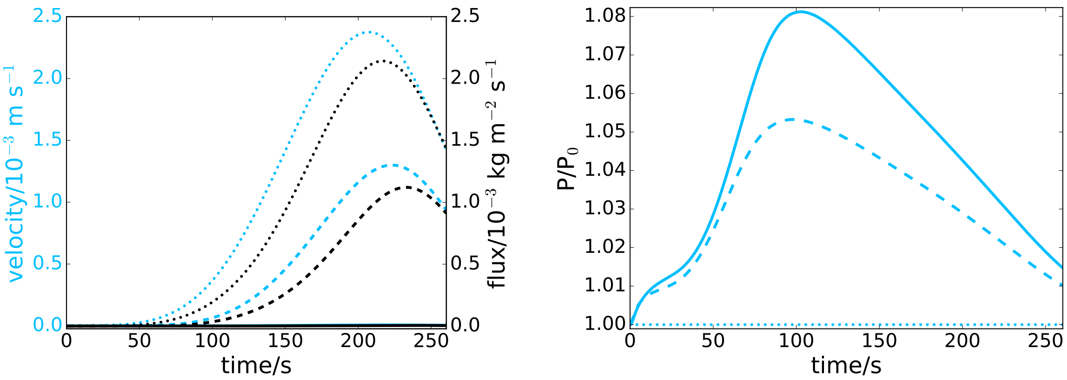

(a) Velocity and flux of the vapour phase

(b) Pressure

Figure 6.4: Calculated vapour phase flux, vapour phase velocity and internal particle pressure for a reactor temperature of 300°C and at different positions in the particle: center (solid line), half radius (dashed line), surface (dotted line).

Across all reactor temperatures, an easily distinguishable trend is that at higher reactor temperatures, there is a higher inner pressure and a higher velocity and flux of the vapour phase. Also, the maximum value of pressure, velocity and flux are reached sooner for higher reactor temperatures.

The behaviour of the inner pressure consists in increasing as the particle starts

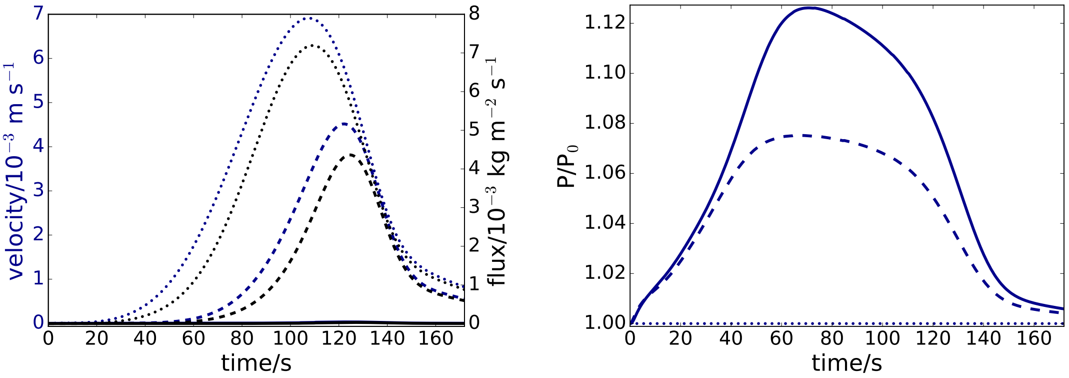

(a) Velocity and volatiles flux

(b) Pressure

Figure 6.5: Calculated volatiles flux, volatiles velocity and internal particle pressure for a reactor temperature of 400°C and at different positions in the particle: center (solid line), half radius (dashed line), surface (dotted line).

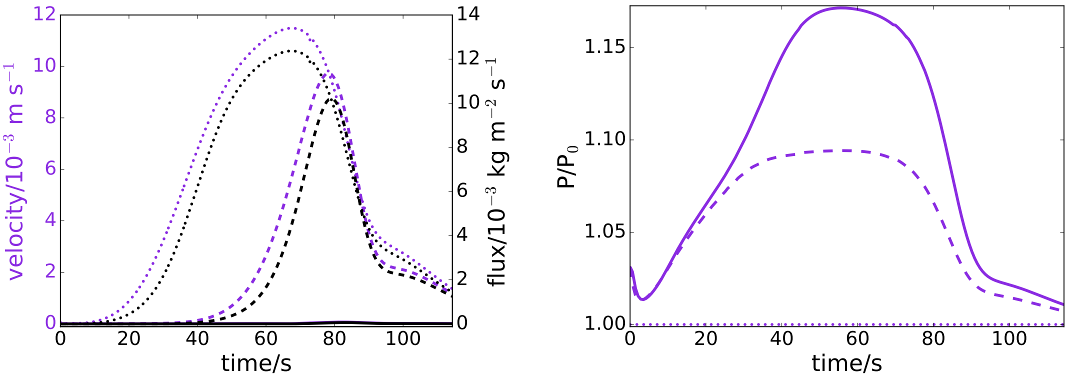

(a) Velocity and volatiles flux

(b) Pressure

Figure 6.6: Calculated volatiles flux, volatiles velocity and internal particle pressure for a reactor temperature of 500°C and at different positions in the particle: center (solid line), half radius (dashed line), surface (dotted line).

heating, it reaches a peak of maximum pressure, which is more distinguishable at the center, and then starts decreasing back to atmospheric pressure. The maximum pressure reached at a half radius position is not as elevated as the pressure at the center, and it appears to maintain a stable mean value between 40-70 s for the reactor temperature of 500°C, between 25-55 s for the

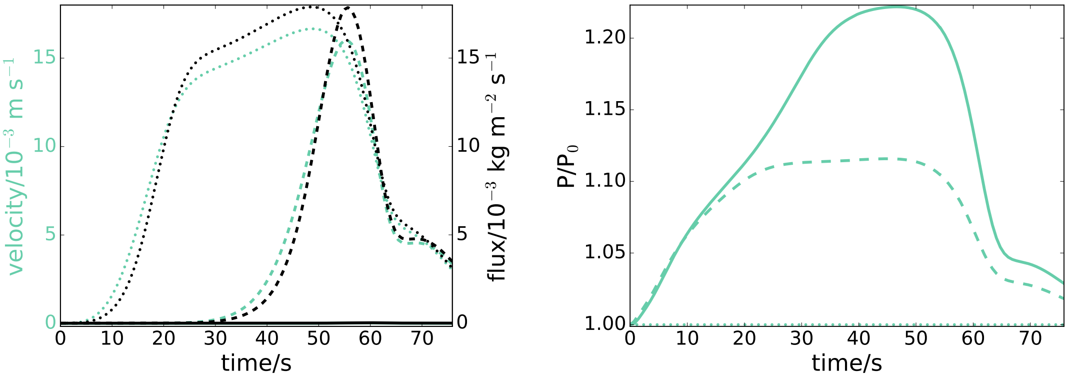

(a) Velocity and volatiles flux

(b) Pressure

Figure 6.7: Calculated volatiles flux, volatiles velocity and internal particle pressure for a reactor temperature of 600°C and at different positions in the particle: center (solid line), half radius (dashed line), surface (dotted line).

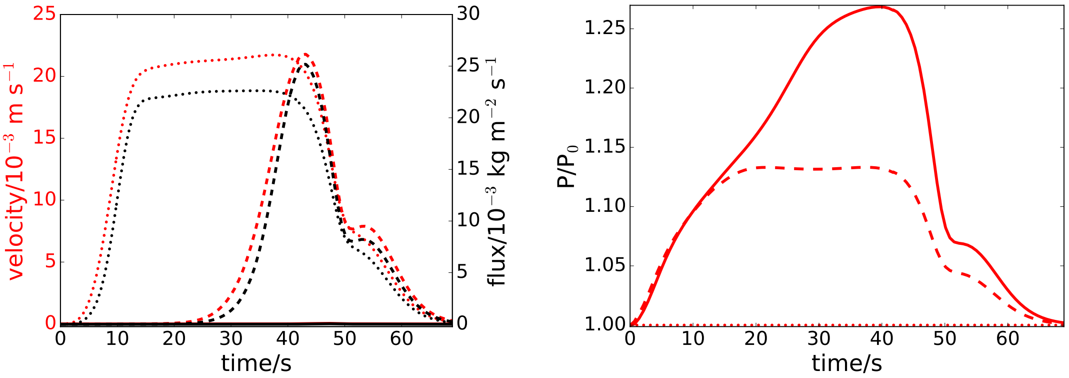

(a) Velocity and volatiles flux

(b) Pressure

Figure 6.8: Calculated volatiles flux, volatiles velocity and internal particle pressure for a reactor temperature of 700°C and at different positions in the particle: center (solid line), half radius (dashed line), surface (dotted line).

reactor temperature of 600°C, and between 20-40 s for the reactor temperature of 700°C, before also decreasing back to atmospheric pressure.

Observing the inner pressure curves it can be noticed that when the inner pressure is already decreasing there is a time where the pressure seems to stabilize for a few seconds, and looking back at Fig. 6.2 it can be seen that that time coincides with when the particle's center temperature reaches the reactor temperature. In the beginning the pressure was increasing due to an increasing temperature and due to a net increase of volatiles in the particle, then the pressure started decreasing due to a net decrease of volatiles in the particle, but the particle was still heating and therefore contributing towards increasing the pressure. When the particle reaches the maximum temperature, the changes in the pressure stop depending on the temperature, and there is a change in the decreasing rate of the pressure and of the volatiles flux.

Observing the velocity and the flux curves it can be seen that after the maximum at the surface position has been reached, there is a point where the surface curves overlap with the half radius curves, that means that the properties of the particle from the surface to the half radius positions are already similar in terms of temperature and permeability.

The increase in pressure is what drives the increase of the vapour velocity, and the vapour flux is calculated from the vapour velocity times the vapour density, that is why the behaviour of the velocity and the flux of the vapour phase is the same. The behaviour of the vapour phase is also linked to the permeability changes in the particle, in this model there is a constant permeability assigned to biomass and a different one to char. The char permeability is higher than the biomass permeability, therefore when the particle starts reacting from the surface, it also means that the permeability starts increasing from the surface and working its way radially towards the center of the particle.

First, the nitrogen that was already in the pellet porosity starts to heat and contributes to increase the pressure in the particle, and later there is generation of volatiles that also contribute to increase the pressure and cause the flux of the vapour phase to increase. The order of theses processes can be more easily observed in Fig. 6.9, that shows the time at which the maximum pressure, maximum velocity and maximum flux are reached for each reactor temperature. As can be seen in almost all the reactor temperatures, the maximum pressure takes place sooner than the flux and velocity maximums, except at high reactor temperatures where all the processes tend to overlap and take place simultaneously. It can also be observed that the pressure at half radius and the pressure at the center reach their corresponding maximums at the same time, and that the velocity at the surface reaches the maximum earlier than the velocity at half radius position.

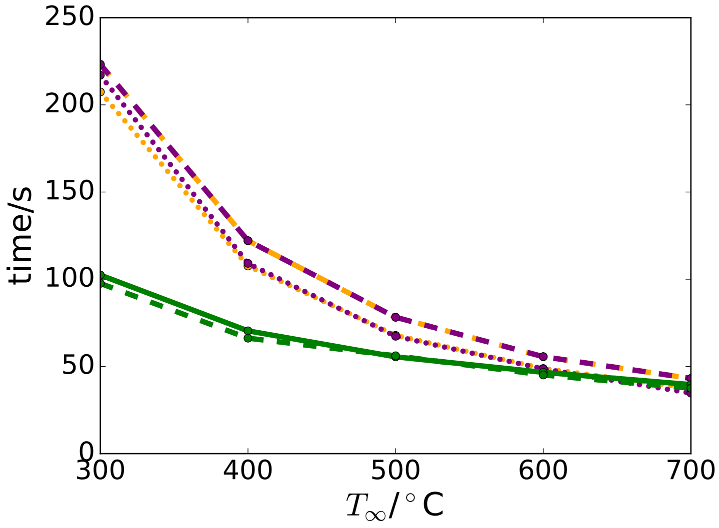

Figure 6.9: Time at which the maximum pressure (green), velocity (orange) and flux (purple) are reached for each reactor temperature and particle position: surface (dotted line), half radius (dashed line), and center (solid line).

6.3 Radial distribution of the relevant properties

This section shows the radial distribution of porosity, pressure and biomass components. Figures 6.10-6.14 show the distribution of the pellet components at different given times (15, 30, 50 and 100 s), as well as for the variables of porosity, temperature and pressure. The values given are dimensionless and their definition can be found in Table 5.4. For the reactor temperatures of 600 and 700°C the final reported time is lower than 100 s because the process had already finished.

Taking Fig. 6.13 for the reactor temperature of 600°C as reference, at 15 s the particle starts heating from the surface and therefore reacting, consuming wheat and generating char, activated wheat and volatiles, the porosity starts increasing from the surface and the pressure starts increasing from the center. At 30 s the activated wheat displays a peak because it is also being consumed, and the volatiles also display a peak because they are being generated as soon as the minimum reaction temperature is achieved, but they are also being released from the surface. At 50 s the peak of activated wheat moves towards the center and the volatiles generation has already reached a maximum at the center. In the end, wheat and activated wheat are completely consumed, the nitrogen and the volatiles are released from the particle leaving only a small quantity of volatiles, and only char is left. The temperature and the porosity have reached a maximum, and pressure has returned to atmospheric conditions.

The volatiles are never completely gone from the particle because the model does not account for the intake of nitrogen from the surroundings and the par-

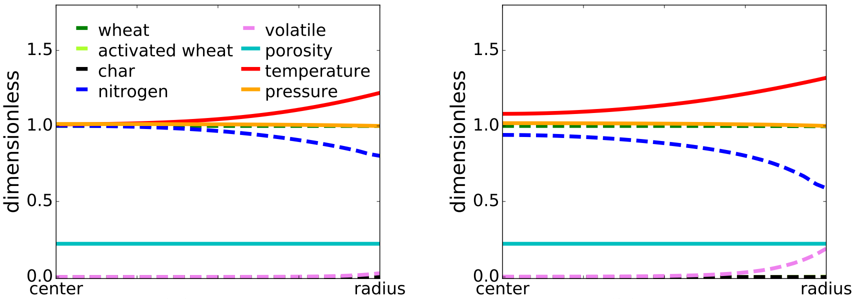

(a) 15 s (b) 30 s

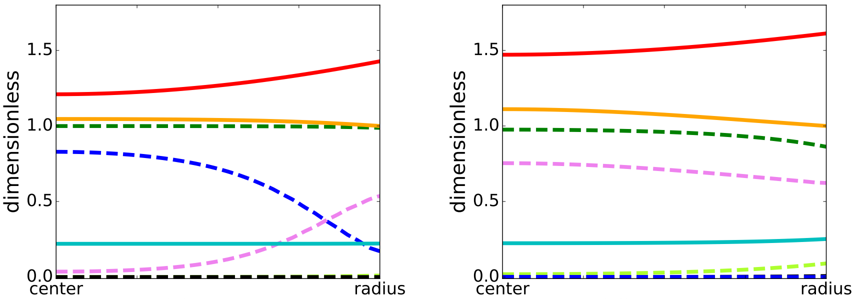

(c) 50 s (d) 100 s

Figure 6.10: Distribution along the particle with a 1D model for $T_\infty = 300°\text{C}$.

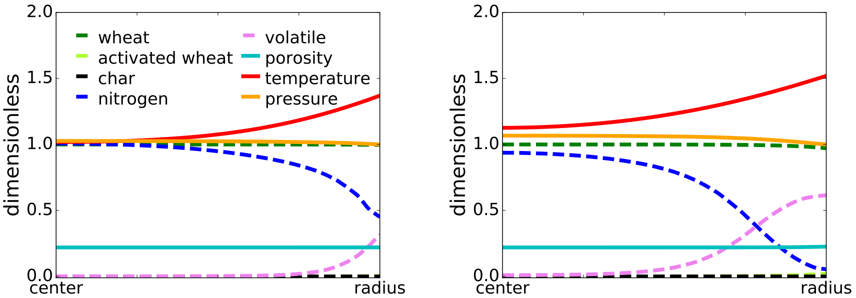

(a) 15 s (b) 30 s

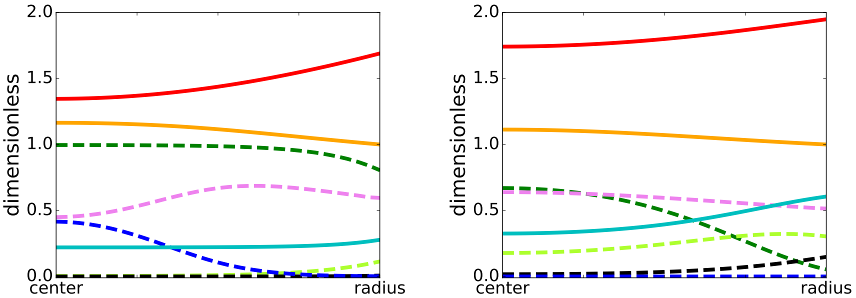

(c) 50 s (d) 100 s

Figure 6.11: Distribution along the particle with a 1D model for $T_\infty = 400°\text{C}$.

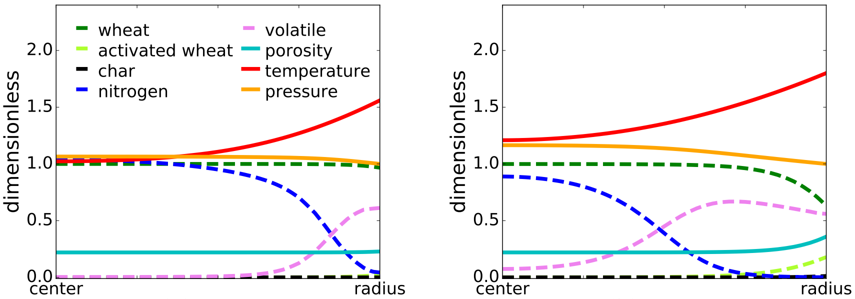

(a) 15 s (b) 30 s

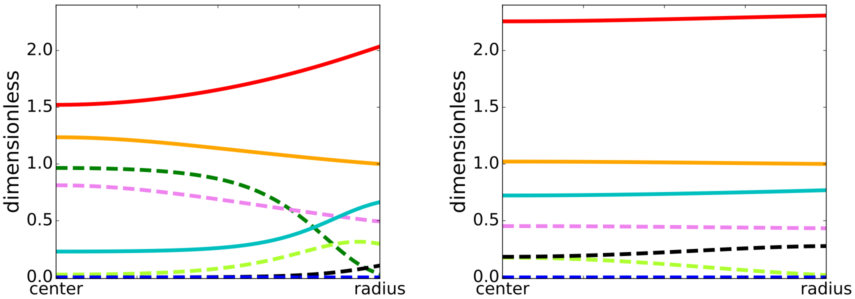

(c) 50 s (d) 100 s

Figure 6.12: Distribution along the particle with a 1D model for $T_\infty = 500°\text{C}$.

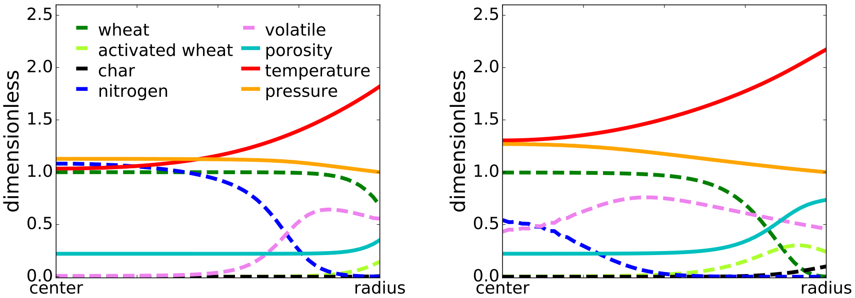

(a) 15 s (b) 30 s

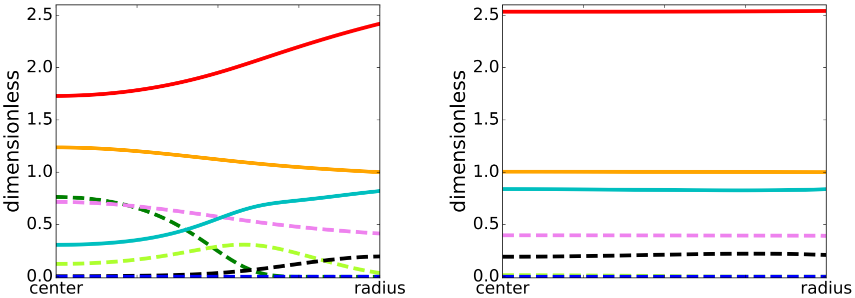

(c) 50 s (d) 86 s

Figure 6.13: Distribution along the particle with a 1D model for $T_\infty = 600°\text{C}$.

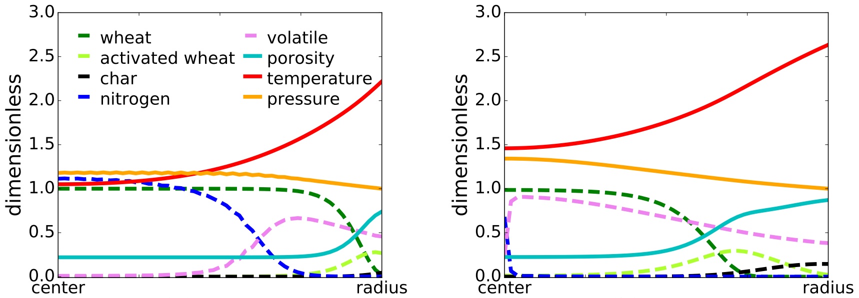

(a) 15 s (b) 30 s

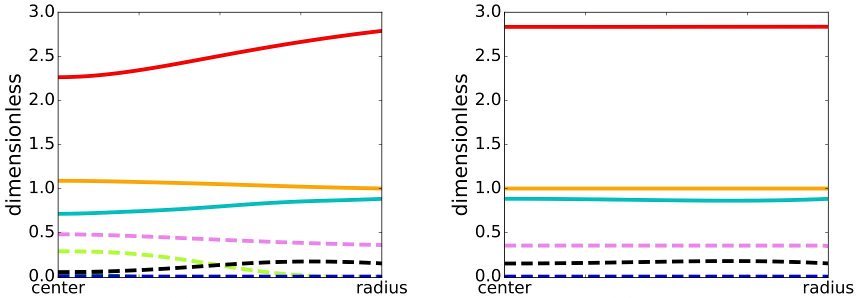

(c) 50 s (d) 84 s

Figure 6.14: Distribution along the particle with a 1D model for $T_\infty = 700°\text{C}$.

ticle cannot be void. The final amount of volatiles should match the initial amount of nitrogen if the porosity was kept constant, but porosity increases with time, and therefore the volatiles density is lower than the initial nitrogen density. The temperature keeps increasing from the surface towards the center till it reaches an horizontal line which matches the surrounding temperature. The activated wheat is being generated at a slighter quicker rate than it is consumed, that is why it is not constantly zero. The nitrogen just leaves the particle. The porosity follows the same trend as the temperature and it stabilizes when the final value of char is stable. And the pressure follows the same trend as the volatiles, it first increases but it is regulated by the release of volatile from the particle so it ends up reaching its initial value of atmospheric pressure.

Figure 6.15a shows the average pellet pressure for different reactor temperatures, the higher the reactor temperature, the more intense is going to be the pyrolysis decomposition and therefore there is a pronounced pressure peak when most of the volatiles are generated and they did not have time to quickly leave the particle, as opposed to the lowest reactor temperature which will not accumulate as many volatiles in the particle because they are slowly generated and they have time to be expelled from the particle.

Figure 6.15b shows the average dimensionless density of the nitrogen and the volatiles inside the particle with time. The nitrogen can only decrease its density because according to the selected boundary conditions, the vapour phase can leave the particle or it can be generated from the reactions, but it cannot be introduced to the particle from the surroundings. The volatiles are generated earlier for higher reactor temperatures, but in the particle they appear to have a lower density because porosity is higher for higher reactor temperatures.

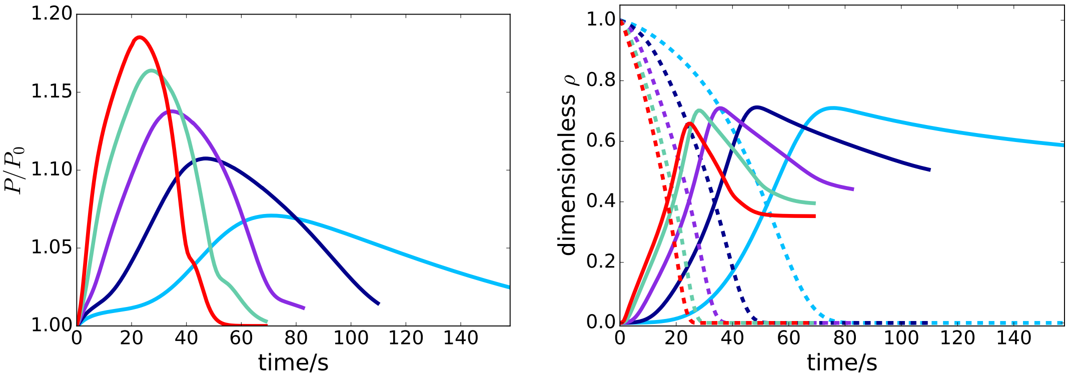

(a) Pressure

(b) Nitrogen (dashed) and volatile (solid)

Figure 6.15: Calculated average pressure and average volatile and nitrogen densities in the particle with time using a one-dimensional model. 300°C (cyan), 400°C (dark blue), 500°C (purple), 600°C (green) and 700°C (red).

The average particle pressure allows to compare the maximum pressure for each reactor temperature and how quickly it increases and decreases, which is linked to the volatiles flux. In the average nitrogen and volatile yield, it can be seen that the dimensionless volatile density does not reach the initial nitrogen density because porosity has increased. If we took into account the effect of convection of the nitrogen carrier gas penetrating the particle, the volatile in the particle would end up being replaced by nitrogen.

6.4 Computational time

A time comparison between this one-dimensional model, excluding the process of mass convection, and a three-dimensional model of the same characteristics has been carried on. Table 6.2 shows a comparison of the time required to run a one-dimensional versus a three-dimensional model of a sphere of the same radius. The computer specifications are Intel® Xeon® Processor E5-1620 v2 and 15GB of RAM. The dimensionless time for the three-dimensional model and reactor temperatures of 600 and 700°C is shorter than the time used in the other instances because at that time the process has already finished, and without any other mechanisms implemented in the model following the volatile release from the particle, the calculations in three-dimensions for those reactor temperatures just slow down and stop. Despite that, it can be observed that the computational time increase is significant.

Table 6.2: Computational time comparison between a one-dimensional and a three-dimensional model of a sphere of radius 0.5 undergoing pyrolysis and without taking into account the gas phase.

T_∞ (°C)	Model	Dimensionless time	Computational time
200	1D/3D	0.1/0.1	11 s/98 min
300	1D/3D	0.1/0.1	11.1 s/133 min
400	1D/3D	0.1/0.1	11.3 s/241 min
500	1D/3D	0.1/0.1	12 s/496 min
600	1D/3D	0.1/0.08	12.6 s/1 week
700	1D/3D	0.1/0.06	13.1 s/1 week

6.5 Conclusions

In this chapter the one-dimensional single particle model was used to explore the process of pyrolysis of a wheat straw pellet, and its suitability has also been discussed. It was found that the optimum reactor temperature to assess the suitability of the chosen thermo-physical properties is around 200°C, or at least below 300°C, when pyrolysis has not yet taken place.

Once the thermo-physical properties have been selected, different kinetic mechanisms can be compared to see which one gives the results of mass loss, internal temperature distribution and product yields more consistent with the experimental data. The choice of a kinetic mechanism can be studied at any reactor temperature above 300°C where pyrolysis takes place, but its application has to be combined with a given choice of heat of reaction, which is not easy because very different enthalpy values have been reported in the literature. The step of comparing or adjusting the kinetic mechanism is not included in this work, but it is a recommendable step and it is proposed as future work. Different values of enthalpy of reaction have been compared, but in general it has been assumed that the decomposition of the raw biomass is endothermic and the remaining reactions are either neutral or exothermic, which makes sense with the experimental data, which shows an increased inner heating rate towards the end of the process.

The process of the vapour phase convection can be solved in a one-dimensional model, but still it entailed numerical instabilities when solving the model equations, which required the application of a stabilization method. All the single particle models of biomass pyrolysis so far, are implemented with a fixed boundary condition with respect to the volatiles release from the particle, which only allows a release of mass from the particle to the surroundings but not the other way around, that is why it would be interesting to apply a different boundary condition to allow input of oxygen from the surroundings towards the particle, and study oxidative pyrolysis and combustion in more detail.

The model developed is flexible in terms of number of reactions, components and order of reaction, that is why this model could be used as a tool to compare different kinetic mechanisms available in the literature, coupled with the single particle model.

In this work, effort has been made in reporting as much information yielded from the single particle model as possible, because in general there is a lack of additional information reported from single particle models, apart from the temperature at the center and perhaps at another inner position, which tends to be the main focus of this type of work. Other single particle models applied to the pyrolysis of wheat straw pellets are not available in the literature. Models on wood particles or wood pellets are available in the literature and they show similar results of heating behaviour at the center of the particle, but most of the remaining model results provided in this work have not been previously reported.

Chapter 7

Three-dimensional pyrolysis simulations of a single biomass particle

In this section the same model equations as previously solved in one-dimension are solved in three-dimensions and compared with experimental data when possible. The heating discrepancies between the one-dimensional and the three-dimensional model were already addressed in Chapter 5, but a further comparison is also given here. The three-dimensional model describes the same processes as the one-dimensional model but in this case, it excludes the process of mass convection because it would be very computationally expensive, and as it has been already discussed in Chapter 5, its contribution to the pellet temperature is not significant unless secondary reactions were involved. The advantage of the three-dimensional model is that more realistic model parameters and heating profiles can be obtained.

In this chapter the single particle model equations are implemented in three-dimensions and a cylindrical shape, excluding the process of convective mass transfer, and the model results are compared with the experimental data from Chapter 4 of the pyrolysis of a dry wheat straw pellet.

7.1 Temperature distribution

This section discusses the temperature distribution inside the pellet. The calculated temperature at the center of the particle with a three-dimensional model is different from the center temperature determined with a one-dimensional model. Figure 7.1 shows the center temperature with the chosen parameters for the one-dimensional model in comparison with the center temperature with the same parameters for the three-dimensional model. It can be noticed that the three-dimensional model heats more quickly than the one-dimensional.

Focusing now on the three-dimensional model, another parameter comparison has been carried out to select the most suitable values with respect to the experimental data. Figure 7.2 shows the experimental center temperature with the calculated center temperatures using different thermophysical values. The calculated solutions show a comparison of the internal temperature profile using different heat capacity correlations for the biomass and the char, and different values of thermal conductivity for the biomass.

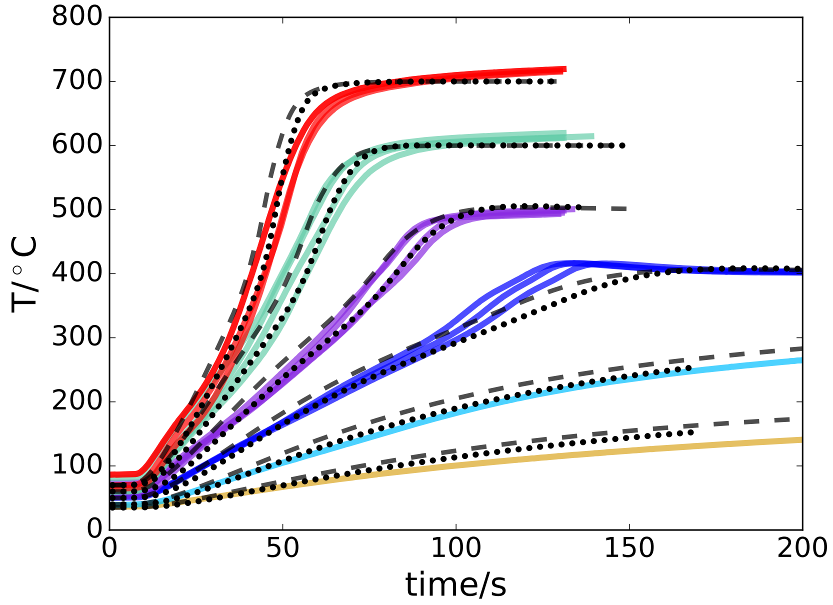

Figure 7.1: Calculated center temperature of a pellet at different reactor temperatures using a 1D spherical (dotted line) and a 3D cylindrical model (dashed line) for a heat capacity from Blondeau et at. [28] and $\lambda_B = 0.15$ W m^{-1} K^{-1}. Each color is for a different reactor temperature: 200°C (yellow), 300°C (cyan), 400°C (dark blue), 500°C (purple), 600°C (green) and 700°C (red).

In Fig. 7.2 it can also be noticed that the effect of a lower heat capacity at the beginning (like in Grønli's correlation), which translates into a higher heating rate, is similar to the effect of having a larger biomass thermal conductivity. The thermal conductivity experimentally determined for a wheat straw pellet is in the order of 0.15 W m^{-1}K^{-1}[183], so it is slightly higher than the biomass thermal conductivity used in Lu et al. [182] of 0.11 W m^{-1}K^{-1} and in this work. Table 6.1 shows the error between the calculated center temperatures using a 3D model and the experimental data. The combination of parameters that best perform with the three-dimensional model is the heat capacity from Blondeau et al. [28] and λ_B = 0.11 W m^{-1} K^{-1}. It can also be observed that the total RMS for the 3D model is lower than the total RMS for the 1D model,

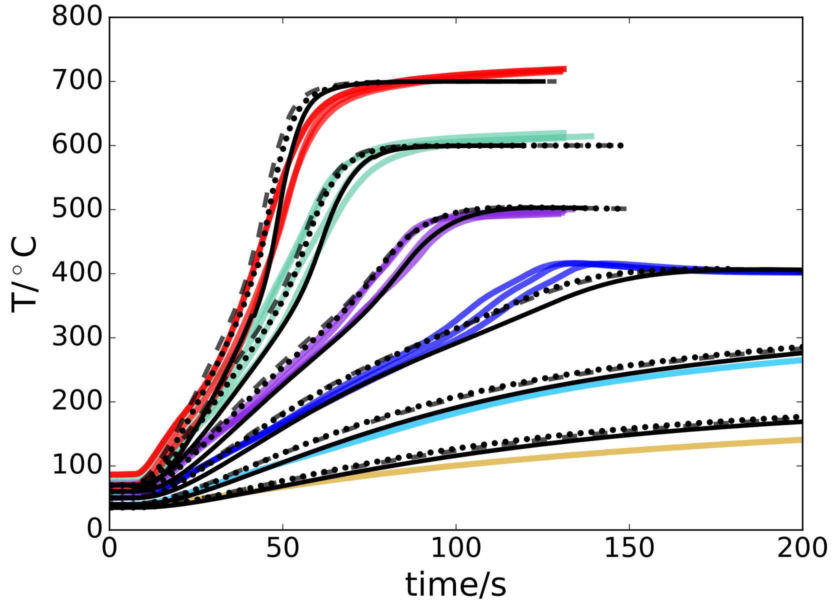

Figure 7.2: Calculated and measured center temperature of a pellet at reactor temperatures of 200°C (yellow), 300°C (cyan), 400°C (dark blue), 500°C (purple), 600°C (green) and 700°C (red), and for different values of biomass and char heat capacity and thermal conductivity of biomass. Predicted data with a three-dimensional model (black lines): λ_B=0.11 W m^{-1} K^{-1} and Blondeau et al. heat capacity (solid line), λ_B=0.15 W m^{-1} K^{-1} and Blondeau et al. heat capacity (dashed line),λ_B=0.11 W m^{-1} K^{-1}, $C_{p,B}$ and and Grønli et al. heat capacity (dotted line).

meaning that the 3D model is closer to the experimental data, but the difference between the respective RMS values is not large.

Figure 7.3 shows the experimental and the calculated center temperature, as well as the temperature at 2 mm from the surface of the particle, and the calculated surface temperature with time for three reactor temperatures. In all the reactor temperatures, a steep rise of the temperature at the 2 mm position could be observed during the first 10 s after the particle starts heating, this steep rise was not seen in the model. This behaviour observed in the experi-

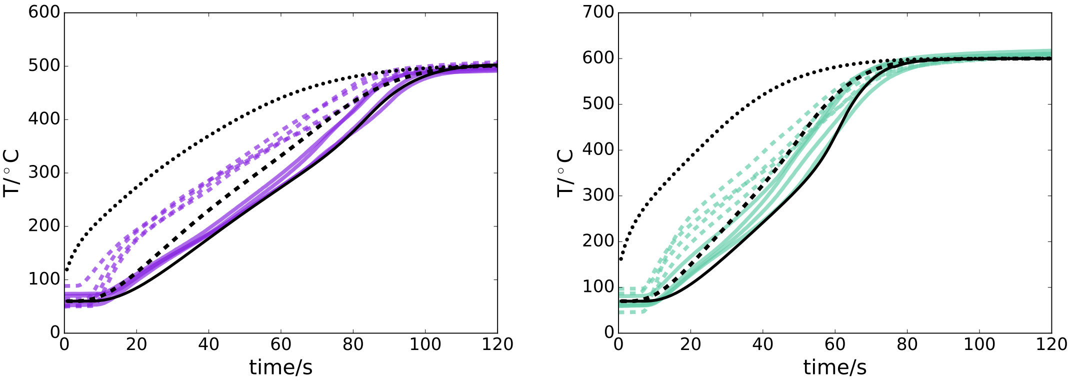

(a) Reactor temperature of 500°C

(b) Reactor temperature of 600°C

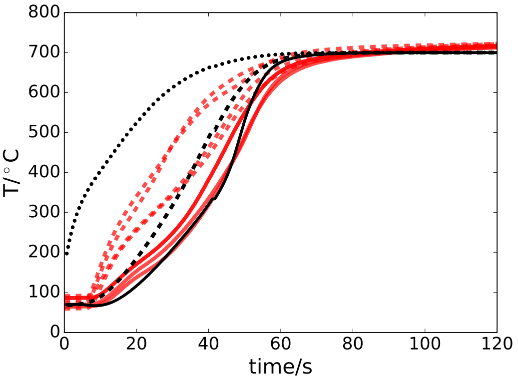

(c) Reactor temperature of 700°C

Figure 7.3: Calculated using a three-dimensional model (black lines) and measured (coloured lines) internal temperature of a pellet at two inner positions. Center temperature (solid lines) and temperature at 2 mm from the surface (dashed lines), plus additional predicted data for the surface temperature (dotted lines).

mental data, is believed to be caused by an increase in heating by convection and thermal radiation due to a damaged pellet surface in the area where the thermocouple was inserted. Otherwise, this behaviour could not be explained by drying reactions because the pellet was dry and the water devolatilization reaction is endothermic, and neither by pyrolysis reactions because the temperature is still too low.

The surface temperature increases earlier than the temperature at the inner positions because the surface receives heat from thermal radiation and thermal convection. Then the heat is transferred to the center by conduction. Heating occurs from the outside to the inside. When the pyrolysis reactions become active on the surface and inside the particle, the enthalpy of the reactions affects the particle temperature.

Figure 7.4 shows the pellet internal temperature distribution for all the reactor temperatures at four given times, the given times are 15 s, 30 s, 50 s and 100 s from when the particle was inserted in the reactor. The temperature range in the legend is the same for all the reactor temperatures to allow a visual comparison across conditions. The pellet at the reactor temperature of 200°C barely changes color before 100 s but the pellets at the reactor temperatures of 400, 500, 600 and 700°C already reached a final homogeneous color by the time of 100 s, meaning that they reached their respective reactor temperature. The pellet starts heating from the surface, particularly from the edges, and the heat spreads inwards. Each of the pellets heats with a different heating rate, which is not constant and might change with time depending on the enthalpy of reaction and on how the material thermophysical properties change with temperature. Higher reactor temperature means a steeper inner temperature gradient in the particle and therefore a larger internal heating rate. The spacial temperature gradient in the particle, in combination with a kinetic mechanism and the volatiles residence time, could be key to predict the specific species in the bio-oil product. Moreover, biomass pyrolysis might comprise endothermic and exothermic reactions, therefore if a desired pyrolysis temperature is to be maintained, information about the internal biomass heating is useful to know how much heat input is required, and avoid a thermal runaway and therefore changing the desired pyrolysis conditions [164].

The product yields characterisation with respect to the pyrolysis conditions have been previously experimentally studied with different types of biomass and with different types of reactors. When fine biomass has been pyrolysed in thermogravimetric analysers, the device heating rate could be compared with a particle internal heating rate, but the species in the product yield would be different because the particle might temporarily trap the volatiles generated and they might decompose further or react with the char or other volatiles species. The studies that link the product yield to the reactor temperature usually use a thermogravimetric analyser or a reactor with large amounts of biomass, as opposed to a reactor that pyrolyses only one particle/pellet, but the product yield trends would be more comparable with results from a pyrolysis reactor than with results from a thermogravimetric analyser. Despite there is plenty of scattered work on the implications of the particle temperature distribution to the pyrolysis behaviour [190, 191, 192, 99], studies that link the inner temperature distribution of a biomass single particle with the species yields in the products have not been found in the literature.

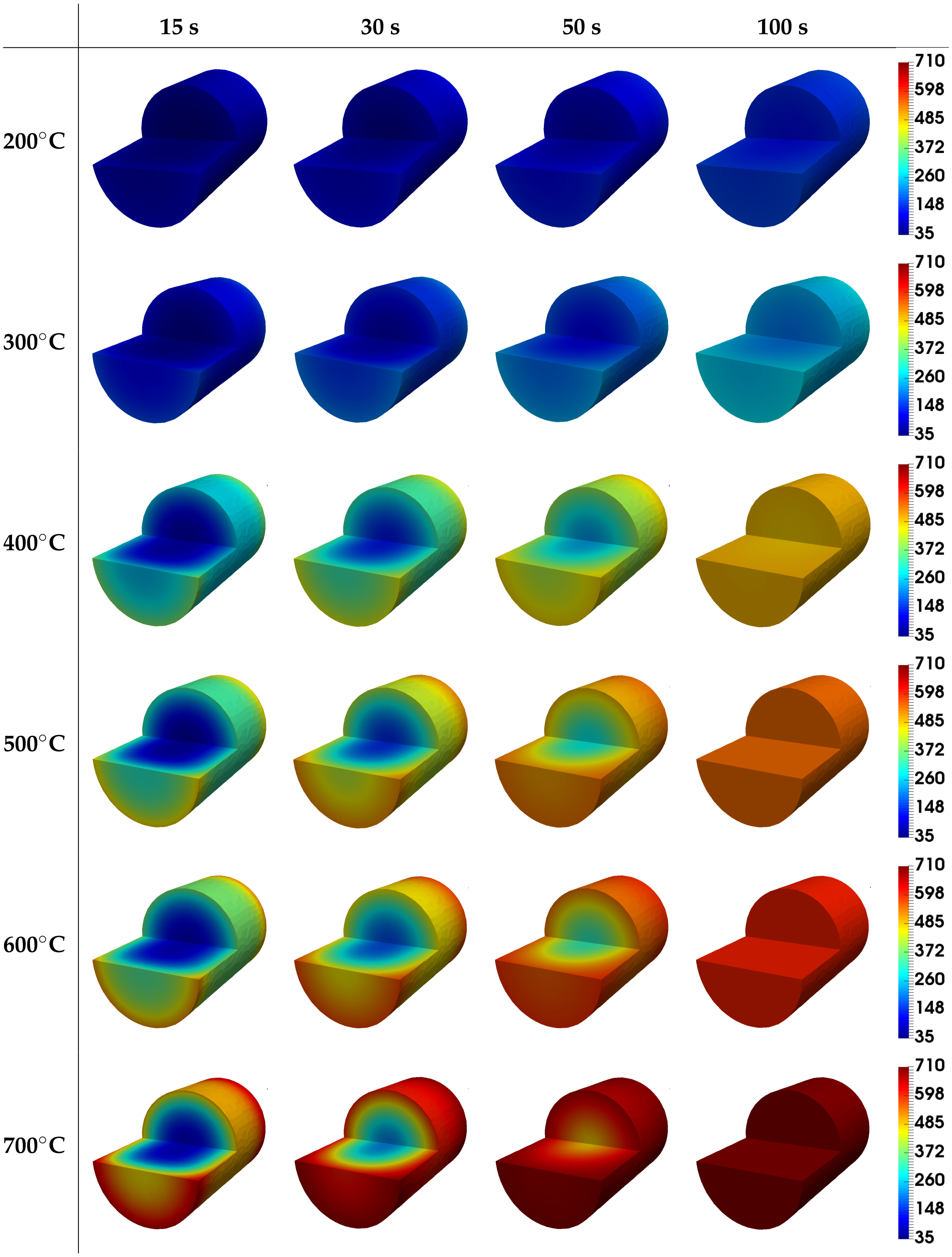

Figure 7.4: Calculated temperature distribution of a pellet for different reactor temperatures at the selected times; the legend is temperature in Celsius degrees.

7.2 Solid phase changes and product yields

This section discusses the pellet mass loss, the evolution with time and space of the porosity, and the evolution with time of the biomass components. Figure 7.5 shows the experimental and calculated mass loss of a pellet at different reactor temperatures. The predicted char yield matches the experimental char yield in the case of the reactor temperature of 500°C, but it should be higher for the reactor temperatures of 600°C and 700°C. For all of the reactor temperatures, the predicted decomposition should be steeper at an earlier time. As already explained in Chapter 4, the char yield is expected to decrease with increasing reactor temperature but only up to a given temperature, after that the decrease should be small. The values of the kinetic parameters used in this work were originally determined for experimental conditions in the range of 400-648 K, therefore they do not account for the stabilization of the char yield at reactor temperatures of 500, 600 and 700 K. To predict higher amounts of char at high reactor temperatures, a char producing reactor could be added to the reaction mechanism. Another possible explanation for the difference in char yields between the experimental data and the model is that in the model the ash content has not been taken into account, and as seen in Tab. 4.1, wheat straw has a high content of ash. To take into account the ash content in the biomass, it could be added as an inert component as part of the raw biomass composition.

Figure 7.6 shows the porosity distribution of the pellet for all the reactor temperatures and at different given times, the scale of the legend is the same for all the reactor temperatures to be able to visually compare the changes across

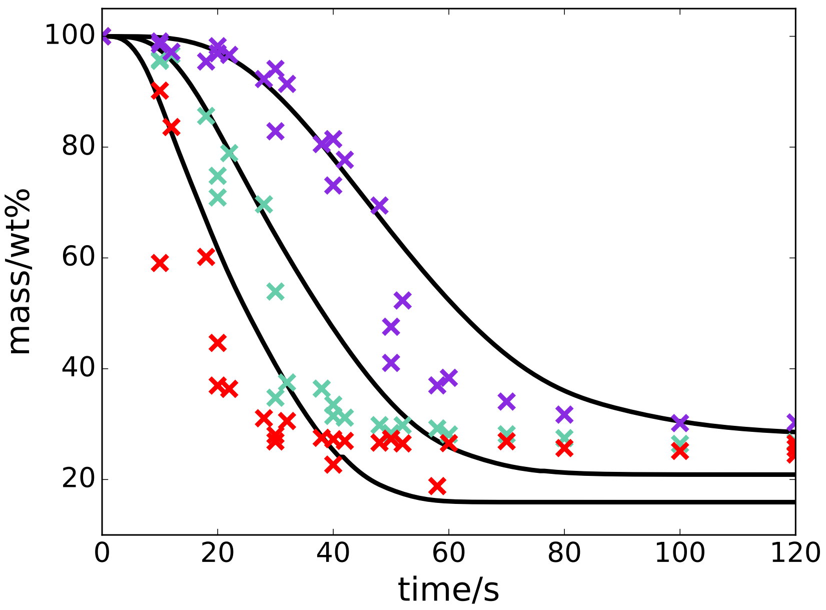

Figure 7.5: Mass loss data of a pellet at different reactor temperatures. Calculated using a three-dimensional model (solid lines) and measured (crosses); Colours as labelled in Fig. 7.2.

the reactor temperatures and across the given times. The figures for the reactor temperatures of 200 and 300°C are not included because below a reactor temperature of 400°C and at 50 s, the porosity has not changed from its original value. The porosity has been calculated with a correlation [134] that depends on the decomposition of the solids in the particle (see Table 5.2). The final porosity has been achieved when the particle color looks homogeneous, that is the case for the pellets at the reactor temperatures of 600 and 700°C at the time of 100 s. The initial porosity is 0.22, and the maximum possible porosity is 1, but the maximum value at which it stabilizes at high temperatures is around 0.8. When the aim of biomass pyrolysis is to produce activated carbon, a feature of interest is the char microporosity volume [193]. In the current model the pore size is not taken into account for the determination of the porosity fraction. Modelling the single particle with a mesh that renders the microporosity would be useful to study the changes in pores size, but it would not be feasible due to its high computational time.

Figure 7.7 shows the evolution of the pellet components with time. The volatile yield corresponds to the total amount of volatiles generated. The higher the reactor temperature, the more quickly the wheat decomposes. The wheat decomposition takes between 50 s and 6.6 min for the reactor temperatures between 700 and 300°C, respectively. At the reactor temperature of 200°C, the wheat decomposition takes more than half an hour because it is a very low pyrolysis temperature that would not normally be used, because the larger the initial raw mass, the longer it will need to decompose, and an operating temperature of 200°C would not be time efficient. At the reactor temperatures of 600 and 700°C, the wheat, activated wheat and volatile display a change in the smoothness of their curves, which is more visible at the reactor temperature of 700°C. These curve inclination changes might be explained by observing the kinetic mechanism already explained in Chapter 5, which consists of two competing reactions that decompose wheat (r1, r2), and two other competing reactions that decompose activated wheat (r3, r4). At higher reactor temperatures, all reactions will tend to a higher degree of overlapping in time.

Figure 7.8 shows the evolution of the calculated porosity with time at three different positions in the pellet and for different reactor temperatures. The positions are the center, at 2 mm from the surface and at the surface. The porosity at the surface for the reactor temperatures of 500, 600 and 700°C displays a shoulder, which could be explained by the behaviour of the activated wheat

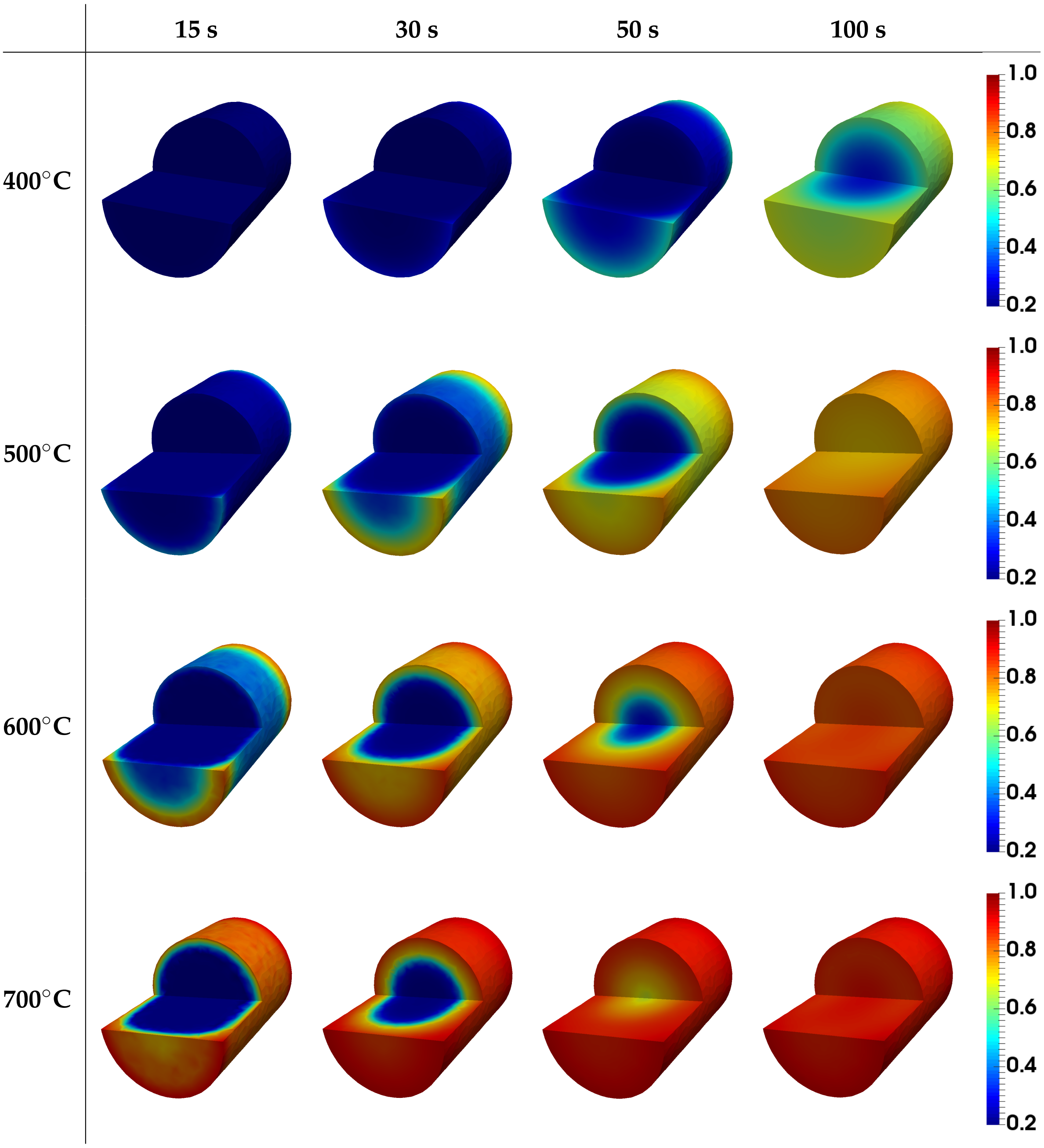

Figure 7.6: Calculated porosity distribution of the pellet for different reactor temperatures at the selected times; the legend is porosity.

straw, which in Fig. 7.7 also features a peak, in which the trend of wheat straw generation is similar to the rate of its consumption for a period of time. For

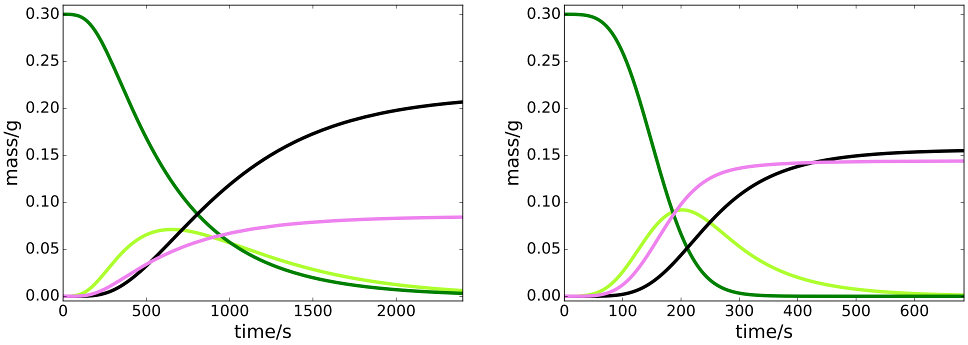

(a) Reactor temperature of 200 °C (b) Reactor temperature of 300 °C

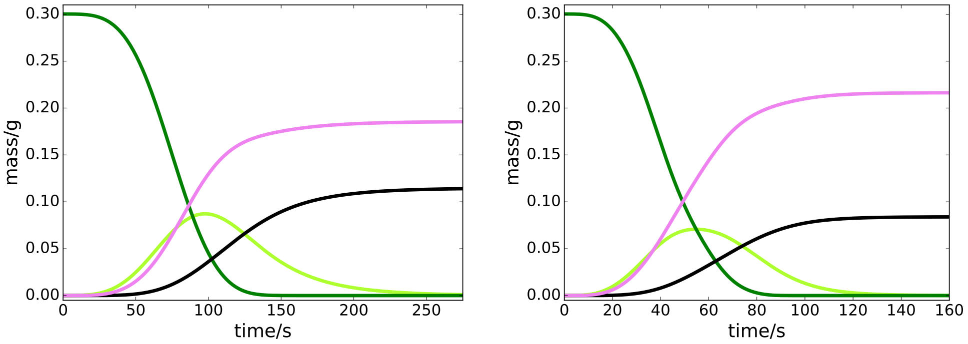

(c) Reactor temperature of 400 °C (d) Reactor temperature of 500 °C

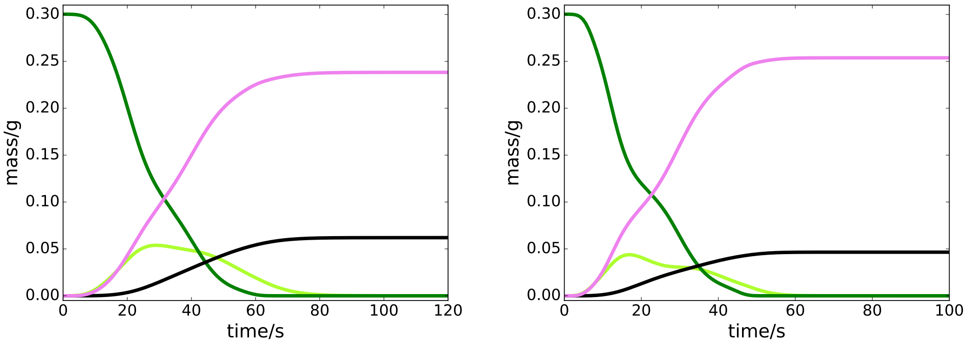

(e) Reactor temperature of 600 °C (f) Reactor temperature of 700 °C

Figure 7.7: Calculated mass change with time of the pellet components for different reactor temperatures: wheat (green), activated wheat (light green), char (black) and volatile (pink).

instance, the surface porosity at a reactor temperature of 700°C increases with a certain inclination for the first 15 s, then it appears stable for about 5 s and then it keeps increasing at a lower porosity rate than at the beginning until it remains constant at its final value. In the beginning the porosity increases sharply because the wheat decomposition starts, but then the generation of char appears to compensate the decomposition of wheat and activated wheat, until there is no more wheat left on the surface and only the decomposition of activated wheat continues to increase the porosity. The same behaviour, but less accentuated can be observed at the center and at the 2 mm positions. The increase of porosity for the reactor temperatures of 200 and 300°C takes a long time, specially for the case of 200°C in which the porosity only increases from 0.22 to about 0.4 after about half an hour, in contrast with the porosity at the reactor temperature of 700°C which only takes about 50 s to reach its maximum porosity value of about 0.9. At the lower reactor temperatures of 200 and 300°C, pyrolysis reactions can still happen, but they require a much longer time.

Figure 7.9 shows the average temperature and the average porosity of the pellet for the different reactor temperatures. The temperature curves are similar to the predicted center temperatures in Fig. 7.2 but without the initial heating delay and without the peak at the reactor temperature of 400°C. The inner heating rates could be approximated by dividing the final pellet temperature by the time that it took to get there. The resulting inner heating rates for each reactor temperature are 10.3 K s^{-1} (700°C), 7.1 K s^{-1} (600°C), 4.5 K s^{-1} (500°C), 2.4 K s^{-1} (400°C), 1.2 K s^{-1} (300°C) and 0.55 K s^{-1} (200°C). The increasing inner heating rate with increasing reactor temperature can also be appreciated from the curves steepness, and it can be observed that the increase in heating rate is less pronounced at higher temperatures because it approaches the ver-

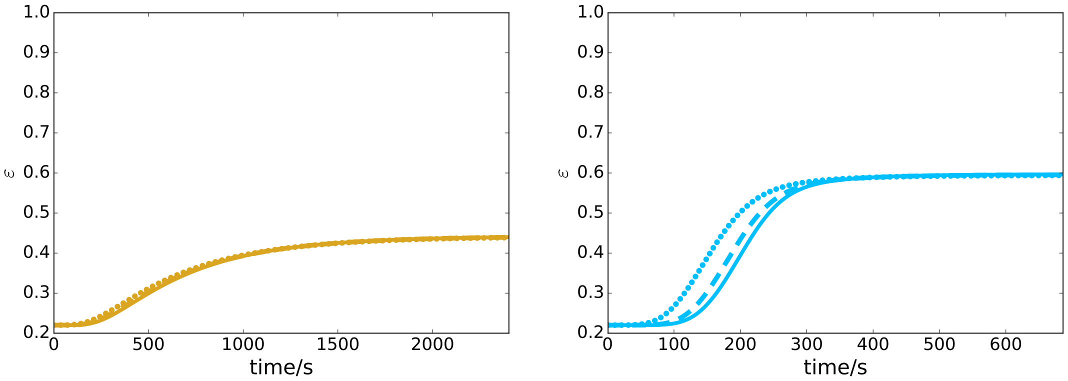

(a) Reactor temperature of 200°C

(b) Reactor temperature of 300°C

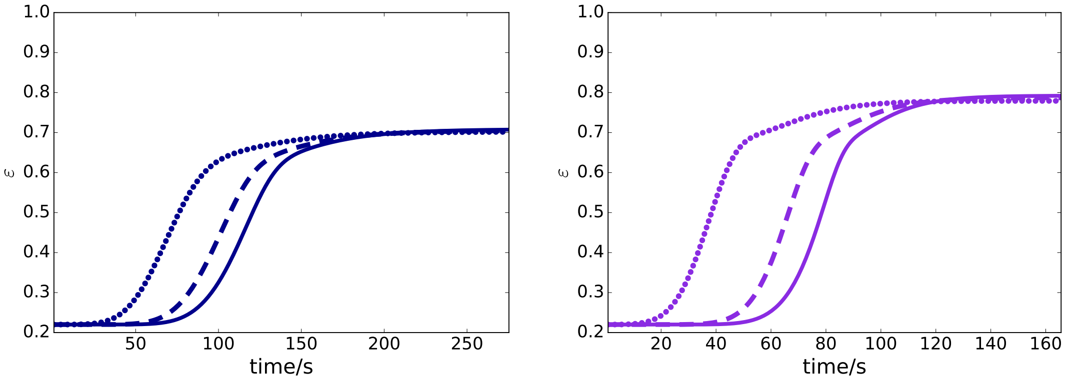

(c) Reactor temperature of 400°C

(d) Reactor temperature of 500°C

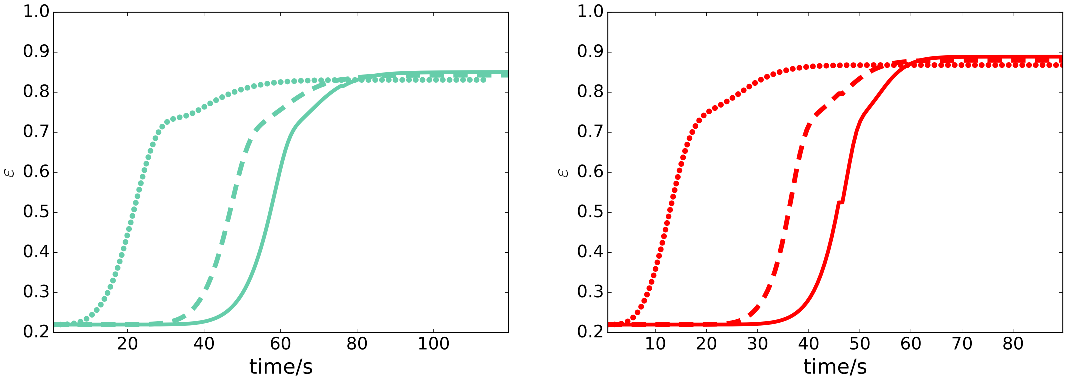

(e) Reactor temperature of 600°C

(f) Reactor temperature of 700°C

Figure 7.8: Calculated porosity evolution with time for different reactor temperatures and at different positions in the pellet: center (solid), at 2 mm from the surface (dashed) and at the surface (dotted).

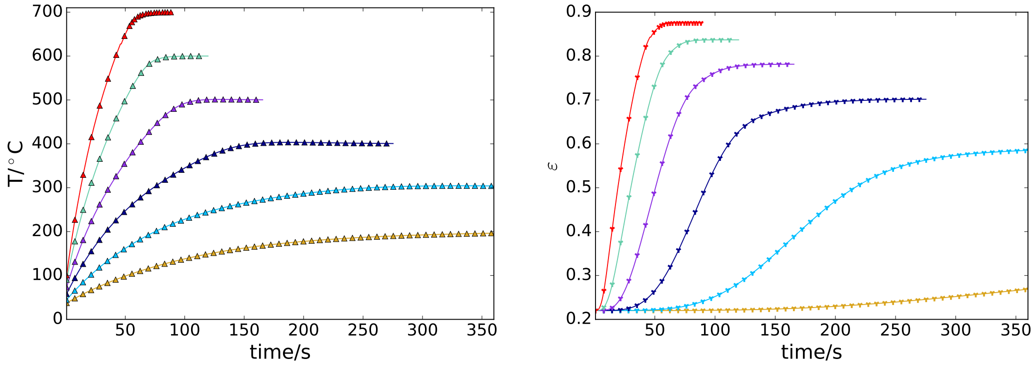

(a) Pellet temperature

(b) Pellet porosity

Figure 7.9: Average pellet temperature and pellet porosity with time for different reactor temperatures, with the same colors as in Fig. 7.2.

tical axis, that would correspond to the instantaneous heating of the particle, characteristic of small biomass particles. The time to reach the final value of average porosity for each reactor temperature is 63 s (700°C), 85 s (600°C), 130 s (500°C), 180 s (400°C), 300 s (300°C), and for the lowest reactor temperatures is 2000 s (200°C), which was not included in the plot because it would make the other curves look too short in comparison. The time at which the porosity reaches a constant value should coincide with the time at which the char yield becomes stable because devolatilization has finalised.

Figure 7.10 shows the char and volatile yields with respect to the original biomass weight. The char amount decreases with an increasing reactor temperature, and the opposite is true for the volatile yield. The pyrolysis time used for each reactor temperature is different, as it can be seen in Fig. 7.7, being shorter for higher reactor temperatures. The product yields obtained experimentally in this work are similar to the reported in the literature, and the calculated yields are also similar to the experimental and literature ones for the

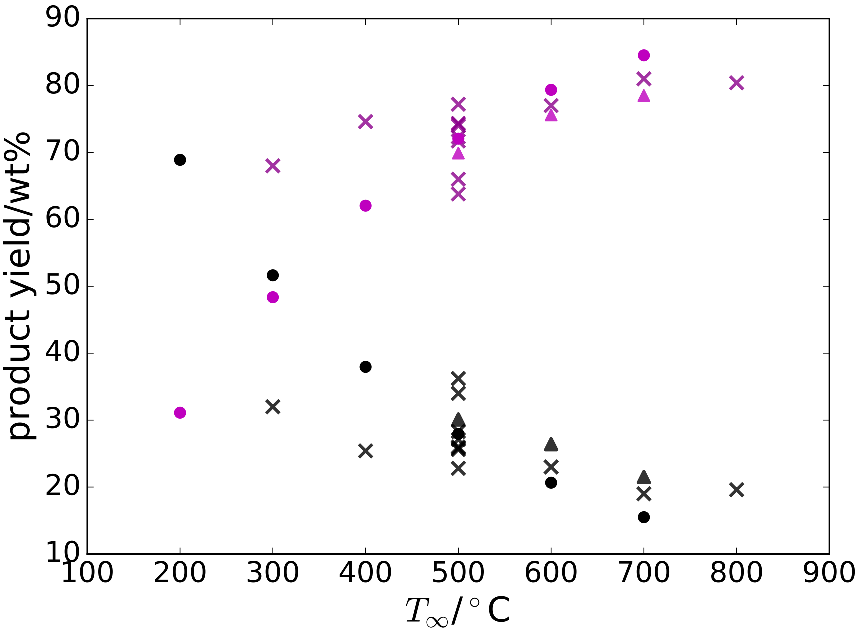

Figure 7.10: Volatile and char yields for different reactor temperatures when the wheat and activated wheat has been completely consumed: calculated (circles), literature data (crosses) [194, 195, 196, 197, 198], experimental (triangles), char (black) and volatile (pink).

reactor temperatures of 500, 600 and 700°C. The product yields calculated for the remaining reactor temperatures are not so similar to the literature values, although for each reactor temperature, except for the reactor temperature of 500°C, there was only one literature value available to compare it with. For the reactor temperature of 500°C the reported product yields are in the range of 20-40% char and 60-80% volatile, this variability of values reflects the impact of the different experimental set-ups or procedures on the final product yield. Each source in the literature might have used a slightly different wheat straw material and a slightly different experimental procedure. For instance, when the experiments are carried out in TGA, an isothermal reactor temperature can be set, but the biomass is in the form of fine particles so it lacks the effect of the volatiles being trapped in the particle pores and the effect of the heat travelling from the surface of the particle to its center. When the experiments are carried out in a pyrolysis reactor, as opposed to the current experiments in a single particle reactor, they use larger amounts of biomass and they introduce the biomass in the reactor before the reactor has already reached the desired pyrolysis temperature.

7.3 Conclusions

In this chapter the three-dimensional single particle model was used to explore the process of pyrolysis of a wheat straw pellet, and its suitability has also been discussed.

The unknown parameters in a single particle model can be investigated experimentally in order to obtain constant values or correlations. However, the results obtained are likely to be more compatible with a three-dimensional model than with a one-dimensional model in the case of large biomass particles of a cylindrical shape, that is because a three-dimensional model would mimic the effect of internal heating with more detail than a simplified one-dimensional model. It has been observed that for the given pellet dimensions the three-dimensional model heats more quickly than the one-dimensional model of any shape, but the gain in model detail might not justify the increase in computational time. The same guidelines for the determination of the model parameters observed in the results from the one-dimensional model also apply to the three-dimensional model.

The experimental measurements of the inner temperature of the pellet have been taken at the center and at 2 mm, it would be very useful in the future to consider taking measurements at more inner positions and also at the surface, to have more basis for model validation. The temperature at 2 mm has been found to be key to confirm the model accuracy, because other parameter combinations could yield a similar center temperature and a similar mass loss curve, but not necessarily a similar temperature at 2 mm. It was also observed that the perforation method of inserting the thermocouple could have damaged the pellet surface, which translates into a shoulder in the temperature data, more visible for the position at 2 mm. Improvement on the perforation technique would be advisable in future work.

The volatile and char prediction matches with experimental and literature trends, but more experimental data about the species in the volatile yield are required for the process of pyrolysis of a pellet, as well as experimental data on the char microporosity. The calculated species in the volatile yield could be obtained by using a detailed kinetic mechanism and validated with the experimental data, and it would be very interesting to match the species yield at each reactor temperature with the corresponding temperature and porosity distribution. The porosity distribution could also be matched with the microporosity distribution if experimental or simulation data are available.

Chapter 8

Overall conclusions

This study consisted on developing and assessing modelling methods that allowed a better understanding of the physico-chemical processes affecting biomass during pyrolysis.

A new method to estimate the parameters of a reaction kinetics model directly from the shape of the derivative thermogravimetric (DTG) curve has been developed. This method is suitable for single or multi-component mechanisms involving single-step reactions. The present work comprehensively encompasses the measurable shape parameters of the DTG curve of biomass pyrolysis and from the study of chromatography peaks reported in the literature, by deriving mathematical expressions that directly link the peak shape with kinetics. The shape parameters reported in this work can be selected and used in any combination, according to the number of required kinetic parameters specific for each reaction model. This gives the flexibility to decide which are the decomposition characteristics that we want to predict with more accuracy, and also to assume different rate constants and reaction models. The accuracy of the method for the determination of biomass composition is as good as the experimental data is representative of the biomass composition of the sample under study. The peak shape method can estimate the contribution of the biomass main chemical components to the volatile yield, but because not all the biomass is converted into volatiles, an accurate composition of the raw biomass cannot be found from thermogravimetric data, but the composition found is still valuable to use as initial composition in a multi-component reaction mechanism.

The pyrolysis behaviour of a wheat straw pellet was experimentally analysed. By comparing the temperature at the center of the pellet with time for the process of pyrolysis and oxidative pyrolysis, it was possible to establish the ignition temperature between 300 and 400°C. The explanation behind that observation is that the center temperature in oxidative pyrolysis is higher than the center temperature in pyrolysis, because in oxidative pyrolysis the volatiles released get in contact with oxygen and partial combustion around the particle occurs, contributing to increase the temperature of the particle.

It was also observed that below 700°C, the process of oxidative pyrolysis generates more carbon monoxide and carbon dioxide than the process of pyrolysis, but at 700°C there is more carbon monoxide in the process of pyrolysis. A possible explanation for this phenomenon is that 700°C is an optimum temperature to generate a large yield of carbon monoxide from biomass decomposition, but when there is oxygen present this carbon monoxide will react with oxygen to form carbon dioxide, that is why at that temperature there is also a large increase of carbon dioxide in the process of oxidative pyrolysis.

A zero-dimensional pyrolysis model, which assumed that the biomass particle is very small, was used to try to describe the mass loss and the center temperature that a wheat straw pellet experiences during pyrolysis, and it was found that the benefit of the model simplicity cannot give accurate results of the inner temperature distribution of a pellet. Instead, a particle model is required to reliably predict the pyrolysis behaviour of thick biomass particles.

The dimensionless form of the governing equations of a single particle model has been analysed to see which are the dominant processes. The value of the dimensionless group referring to the volatile phase in the energy balance is very small, indicating that the contribution of the volatiles to the particle temperature is not significant. The dominant heating mechanism of the particle is the external heating, particularly heat convection. Although mass convection of the volatiles phase is not significant to the inner heating profile of a particle undergoing pyrolysis, it is still an essential mechanism to study the volatiles product yield and their potential secondary reactions. In this work secondary reactions have not been included in the model, but the mechanism of volatiles convection has been studied. To that end, a numerical stabilization method has been successfully implemented in the single particle model solved with the finite element method, to help deal with instabilities in the numerical solution.

The thermo-physical properties of the biomass material such as thermal conductivity and heat capacity are a required input in a single particle model. It is recommendable to obtain experimental data of pyrolysis at low temperatures to first make sure that the selected properties, in combination with the external heat flow and the biomass density, are able to represent the inner heating of a given biomass. Once the selected thermo-physical properties have been found suitable, experimental data of pyrolysis at higher temperatures could be used to find a kinetic mechanism and an enthalpy of reaction that are able to render the experimental heating profile caused by pyrolysis.

Experimental information about the inner temperature distribution of a particle undergoing pyrolysis is paramount in adjusting the parameters of a single particle model. In this work two inner positions have been measured, one at the center and the other at 2 cm from the surface at one end of the pellet. It is recommended to obtain data from as many inner positions as possible. Information about the experimental center temperature and the mass loss is not enough to adjust and validate a single particle model, and it does not ensure an accurate prediction of the process.

The way in which the single particle model is implemented gives flexibility to solve the equations in one-dimension or three-dimensions. A comparison of the one-dimensional and the three-dimensional models was performed in terms of their corresponding heating profiles. From these results it has been shown that the shape of the particle influences the inner heating profile, and that the assumption of a one-dimensional model decreases the model accuracy with respect to the heating profile of the particle. However, the computational time required with the three-dimensional model might not compensate the small increase in the accuracy of the temperature prediction and it certainly makes it unsuitable to study the vapour phase transport phenomena, which requires a high mesh resolution and a very small time-step.

To render the pyrolysis of a pellet that has a shape different from a sphere or a long cylinder, whenever the computational cost allows it, a three-dimensional model should be selected. However, if a reduction of the model complexity is required and a one-dimensional model has to be used, then a particle shape of a sphere is most suitable for a short cylindrical pellet than a one-dimensional cylinder. The values of the thermo-physical properties selected for the single particle model ideally should be based on the three-dimensional model, which renders more realistically the heating of a cylindrical pellet of the size used in this work. However, the same thermo-physical properties might not give satisfactory results when applied to the one-dimensional model, because the particle shape influences the inner heating profile. When using a one-dimensional model, either the thermal conductivity could be increased or the heat capacity decreased with respect to the estimated biomass properties in order to approach the heating profile obtained using a three-dimensional model.

The mass loss calculated with the single particle model for the different reactor temperatures yields a lower char content for higher reactor temperatures by the end of pyrolysis. While this behaviour makes sense, it would also make sense that from a given reactor temperature, the differences in final char yield would tend to stabilize, after all, there is only a maximum weight percentage of biomass that is physically able to be released in the form of volatile. This observation suggests that either the ash content in wheat straw is significant enough to be added as an initial biomass component, or that there should be a char generating reaction added to the kinetic mechanism.

8.1 Future work

Further investigation of biomass pyrolysis linking realistic particle shape and size and typical operating conditions with the characterization of the yielded products is required to optimize the process and increase its commercial applicability.

The modelling work developed in this thesis can be used as a tool for future research on the biomass kinetics and transport phenomena. The peak shape method can be used as a tool to obtain a quick kinetic analysis, therefore it would be interesting to compare the pyrolysis behaviour of different types of biomass. The possibility to use the peak shape method with different single-step mechanisms, and to adapt it to other reaction laws different from the first-order, makes it possible to also study other thermal processes from which a derivative thermogravimetric curve can be obtained, such as a drying process or the decomposition of other polymers or solid fuels.

Relevant experimental data could be obtained from the pyrolysis of a biomass particle by following the suggestions given in this work, which includes obtaining a more detailed temperature profile of the pellet and the determination of the biomass thermo-physical properties from the temperature profile of the particle at low reactor temperatures.

A very attractive simulation study of pyrolysis of a single particle, in addition to including the process of mass convection, would be to allow the gas in the reactor environment to penetrate the particle pores. This model would be very useful to study secondary pyrolysis, and it could also be applied for oxidative pyrolysis, combustion and gasification.

The single particle model developed in this work is very flexible in terms of the kinetic mechanism assumed, therefore a thorough comparison of different kinetic mechanisms available in the literature would be useful to identify the mechanism best suited with respect to the given experimental data and the information required from the model predictions.

A parameter that has not yet been determined for the pyrolysis of a single particle is the residence time of the volatiles inside the particle, which is different from the residence time of the volatiles in the reactor, and more difficult to estimate. The volatiles generated from pyrolysis are more likely to undergo secondary reactions if they are either inside the particle or very close to its surface, therefore the investigation of this parameter would allow its utilization as an operating condition.

The inner temperature distribution and the inner volatiles velocity obtained from the single particle model could potentially be matched with the characterization of the volatile yield, allowing a direct link between the inner heating rate of the particle and species in the product. Another interesting possibility of future work would be to match the inner temperature and porosity distribution with the char quality and microporosity, allowing the determination of the best operating conditions depending on the desired char applications. To that end, it would be beneficial to find a way to define a changing pore size in the model.

At a broader level, the particles interaction inside a reactor as well as the reactor fluid dynamics should also be considered to fully understand and predict the performance of biomass pyrolysis at either small or large scale.

Appendices

Appendix A

Transformation of the energy balance

Transformation of the energy balance from the variable enthalpy to temperature. The original form of the balance is in terms of enthalpy.

$$\frac{\partial}{\partial t}(\rho_s H_s + \varepsilon \rho_v H_v) + \nabla \cdot (\mathbf{u} \sum_i \rho_{v,i} H_{v,i}) = \nabla \cdot (\lambda \nabla T) + \nabla \cdot \left[\sum_i H_{v,i} \varepsilon D \left(\nabla \rho_{v,i} - \frac{\rho_{v,i}}{\rho_v} \nabla \rho_v \right) \right] \tag{A.1}$$

Assuming that

$$\left(\frac{\partial H}{\partial T}\right)_P = C_p \tag{A.2}$$

$$\nabla H = C_p \cdot \nabla T \tag{A.3}$$

the product rule on the first term is applied

$$\frac{\partial}{\partial t}(\rho_s H_s + \varepsilon\rho_v H_v) = \left(\rho_s \frac{\partial H_s}{\partial t} + H_s \frac{\partial \rho_s}{\partial t}\right) + \left(\varepsilon\rho_v \frac{\partial H_v}{\partial t} + H_v \frac{\partial \varepsilon\rho_v}{\partial t}\right) \tag{A.4}$$

$$= \left(\rho_s C_{p,s} \frac{\partial T}{\partial t} + \varepsilon\rho_v C_{p,v} \frac{\partial T}{\partial t}\right) + \left(H_s \frac{\partial \rho_s}{\partial t} + H_v \frac{\partial \varepsilon\rho_v}{\partial_t}\right), \tag{A.5}$$

now the product rule on the second term

$$\nabla \cdot (\mathbf{u} \sum_i \rho_{v,i} H_{v,i}) = \mathbf{u}\rho_{v,i} \cdot \nabla H_{v,i} + H_{v,i} \nabla \cdot (\mathbf{u}\rho_{v,i}) \tag{A.6}$$

$$= \mathbf{u}\rho_{v,i} C_{p,i} \cdot \nabla T + H_{v,i} \nabla \cdot (\mathbf{u}\rho_{v,i}). \tag{A.7}$$

At this point, this is how the energy balance looks

$$
\begin{aligned}
&(\rho_s C_{p,s} + \varepsilon \rho_v C_{p,v})\frac{\partial T}{\partial t} + \mathbf{u}\rho_v C_{p,v} \cdot \nabla T - \nabla \cdot (\lambda \nabla T) \\
&= -\sum_i H_{s,i}\frac{\partial \rho_s}{\partial t} - \sum_i H_{v,i}\left(\frac{\partial}{\partial t}(\varepsilon \rho_{v,i}) + \nabla \cdot \left[(\mathbf{u\ae_{v,i}}) - \varepsilon D\left(\nabla \rho_{v,i} - \frac{\rho_{v,i}}{\rho_v}\nabla \rho_v\right)\right]\right).
\end{aligned}
\tag{A.8}
$$

Next, if we take into account Eq. (5.5) and (5.8), we can modify the terms with enthalpy as follows

$$
\begin{aligned}
&(\rho_s C_{p,s} + \varepsilon \rho_v C_{p,v})\frac{\partial T}{\partial t} + \mathbf{u}\rho_v C_{p,v} \nabla T - \nabla \cdot (\lambda \nabla T) \\
&= -\sum_{r,i} H_{s,i}\nu_{r,i}\frac{\partial \xi_r}{\partial t} - \sum_{r,i} H_{v,i}\nu_{r,i}\frac{\partial \xi_r}{\partial t}
\end{aligned}
\tag{A.9}
$$

$$
\boxed{(\rho_s C_{p,s} + \varepsilon \rho_v C_{p,v})\frac{\partial T}{\partial t} + \mathbf{u}\rho_v C_{p,v} \cdot \nabla T - \nabla \cdot (\lambda \nabla T) = -\sum_r \Delta H_r \frac{\partial \xi_r}{\partial t}}
\tag{A.10}
$$

where

$$
\Delta H_r = \sum_i H_{s,i}\nu^s_{r,i} + \sum_i H_{v,i}\nu^v_{r,i}
\tag{A.11}
$$

and

$$(C_{p,s}\rho_s + \varepsilon C_{p,v}\rho_v)\frac{\partial T}{\partial t} = \sum_i (C_{p,i}\rho_{s,i} + \varepsilon C_{p,i}\rho_{v,i})\frac{\partial T}{\partial t}. \tag{A.12}$$

Appendix B

Finite element formulation of the governing equations

The variational formulation of the governing equations is

$$F_T = \int \frac{\partial T}{\partial t} \psi_T \, dx + \int \mathbf{u} \rho_v C_{p,v} \cdot \nabla T \psi_T dx + \int \lambda \nabla T \cdot \nabla \psi_T \, dx + \int \Delta H_r \frac{\partial \xi_r}{\partial t} \psi_T \, dx$$
$$+ \oint h_T (T - T_\infty) \psi_T \, ds + \oint \epsilon \sigma ((T^n)^4 - T_\infty^4) \psi_T \, ds = 0 \tag{B.1}$$

$$F_{\rho_s} = \sum_i \int \frac{\partial \rho_{s,i}}{\partial t} \psi_{\rho_{s,i}} \, dx - \int \sum_i \sum_r \nu_{r,i} \frac{\partial \xi_r}{\partial t} \psi_{\rho_{v,i}} \, dx = 0 \tag{B.2}$$

$$F_{\rho_v} = \sum_i \int \frac{\partial \rho_{v,i}}{\partial t} \psi_{\rho_{v,i}} \, dx + \int \nabla \cdot (\rho_{v,i} \mathbf{u}) \, \psi_{\rho_{v,i}} \, dx - \int \sum_i \sum_r \nu_{r,i} \frac{\partial \xi_r}{\partial t} \psi_{\rho_{s,i}} \, dx = 0 \tag{B.3}$$

(B.4)

$$F_{\varepsilon} = \int \left[\varepsilon - [1 - (1 - \varepsilon_0)] \frac{\rho_s}{\rho_{s,0}} \right] \psi_{\varepsilon} \, dx = 0 \tag{B.5}$$

$$F_P = \int \left[P - \sum_i \frac{\rho_{v,i}}{MW_{v,i}} R\, T \right] \psi_P \, dx = 0 \tag{B.6}$$

$$F_u = \int \left[v + \frac{\kappa}{\mu} \nabla P \right] \, \psi_v \, dx = 0 \tag{B.7}$$

where T is temperature, included in the energy balance in Eq. 5.12, ρ_s is the density of the solid phase, included in the solid mass balance in Eq. 5.5, ρ_v is the density of the vapour phase, included in the vapour mass balance in Eq. 5.8, P is pressure, included in the ideal gas law from Eq. 5.10, ε is porosity, included in Eq. 5.11, and $\mathbf{u}$ is the velocity of the vapour phase, included in Eq. 5.9.

The variational formulation of the volatiles conservation equation, including the stabilization term is

$$\begin{aligned} F_{\rho_v} = \sum_i \int \frac{\partial \rho_{v,i}}{\partial t} \psi_{\rho_{v,i}} \, dx - \int \sum_i \sum_r \nu_{r,i} \frac{\partial \xi_r}{\partial t} \psi_{\rho_{s,i}} \, dx + \int \left(\mathbf{u} \cdot \nabla \rho_{v,i} \right) \psi_{\rho_{v,i}} \, dx \\ + \int \sum_i \tau_{SUPG} \, \mathbf{u} \cdot \nabla \psi_{\rho_{v,i}} (\mathbf{u} \cdot \nabla \rho_{v,i}) \, dx \end{aligned} \tag{B.8}$$

The corresponding basis functions for each variable are

$$T = \sum_j T_j \psi_{T,j} \tag{B.9}$$

$$\rho_s = \sum_j \rho_{s,j} \psi_{\rho_{s,j}} \tag{B.10}$$

$$\rho_v = \sum_j \rho_{v,j} \psi_{\rho_{v,j}} \tag{B.11}$$

$$\varepsilon = \sum_j \varepsilon_j \psi_{\varepsilon,j} \tag{B.12}$$

$$P = \sum_j P_j \psi_{P,j} \tag{B.13}$$

$$\mathbf{u} = \sum_j u_j \psi_{u,j} \tag{B.14}$$

Appendix C

Supplementary information

The programs used to generate some of the key figures in this thesis are supplied as additional material and can be found in `https://doi.org/10.15129/85fc257c-19ae-4399-a747-70a32084bee9`. The program linked to each selected figure can be used as a tool to study other materials and process conditions. The figures selected are from the chapters where mathematical models have been implemented. Figures 3.7 and 3.9 from Chapter 3 are examples of application of the developed fitting method for thermogravimetric data from pyrolysis of biomass, and Figures 6.2 and 7.2 from Chapters 6 and 7 are the results obtained by numerically solving the single particle model for the pyrolysis of a wheat straw pellet.

Bibliography

[1] M. Höök and X. Tang, “Depletion of fossil fuels and anthropogenic climate changea review,” *Energy Policy*, vol. 52, pp. 797–809, 2013.

[2] I. D’Adamo and P. Rosa, “Current state of renewable energies performances in the european union: A new reference framework,” *Energy Conversion and Management*, vol. 121, pp. 84–92, 2016.

[3] M. Calvin, “Photosynthesis as a resource for energy and materials,” *Photochemistry and Photobiology*, vol. 23, no. 6, pp. 425–444, 1976.

[4] A. Bridgwater, D. Meier, and D. Radlein, “An overview of fast pyrolysis of biomass,” *Organic Geochemistry*, vol. 30, no. 12, pp. 1479–1493, 1999.

[5] A. Faaij, “Modern biomass conversion technologies,” *Mitigation and Adaptation Strategies for Global Change*, vol. 11, no. 2, pp. 343–375, 2006.

[6] M. Sharifzadeh, M. Sadeqzadeh, M. Guo, T. N. Borhani, N. M. Konda, M. C. Garcia, L. Wang, J. Hallett, and N. Shah, “The multi-scale challenges of biomass fast pyrolysis and bio-oil upgrading: Review of the state of art and future research directions,” *Progress in Energy and Combustion Science*, vol. 71, pp. 1–80, 2019.

[7] N. Z. Atashbar, N. Labadie, and C. Prins, “Modeling and optimization of biomass supply chains: A review and a critical look,” *IFAC-PapersOnLine*, vol. 49, no. 12, pp. 604–615, 2016.

[8] D. L. Klass, “Biomass for renewable energy and fuels,” *Encyclopedia of Energy*, vol. 1, no. 1, pp. 193–212, 2004.

[9] M. T. Halbouty, *Giant oil and gas fields of the decade, 1990-1999*, vol. 78. American Association of Petroleum Geologists, 2003.

[10] E. Johnson, "Goodbye to carbon neutral: Getting biomass footprints right," *Environmental Impact Assessment Review*, vol. 29, no. 3, pp. 165–168, 2009.

[11] A. T. Jonas Bervoets, Olivier Dubois, "Building resilience through safe access to fuel and energy (SAFE)," tech. rep., FAO, Rome, Italy, 2018.

[12] REN21 community, "Renewables 2018 global status report," tech. rep., REN21, Paris, France, 2018.

[13] M. A. Arbex, J. E. D. Cançado, L. A. A. Pereira, A. L. F. Braga, and P. H. d. N. Saldiva, "Queima de biomassa e efeitos sobre a sáude," *Jornal Brasileiro de Pneumologia*, vol. 30, pp. 158–175, 2004.

[14] K. Kaygusuz and T. Sekerci, "Biomass for efficiency and sustainability energy utilization in turkey," *Journal of Engineering Research and Applied Science*, vol. 5, no. 1, pp. 332–341, 2016.

[15] A. A. Rentizelas, A. J. Tolis, and I. P. Tatsiopoulos, "Logistics issues of biomass: The storage problem and the multi-biomass supply chain," *Renewable and Sustainable Energy Reviews*, vol. 13, no. 4, pp. 887–894, 2009.

[16] J. Müllerová, "Health and safety hazards of biomass storage," vol. 1, 06 2014.

[17] D. Ilic, K. Williams, R. Farnish, E. Webb, and G. Liu, "On the challenges facing the handling of solid biomass feedstocks," *Biofuels, Bioproducts and Biorefining*, vol. 12, 2018.

[18] A. Giuliano, M. Poletto, and D. Barletta, "Process optimization of a multi-product biorefinery: The effect of biomass seasonality," *Chemical Engineering Research and Design*, vol. 107, pp. 236–252, 2016.

[19] D. Yue, F. You, and S. W. Snyder, "Biomass-to-bioenergy and biofuel supply chain optimization: Overview, key issues and challenges," *Computers & Chemical Engineering*, vol. 66, pp. 36–56, 2014.

[20] J. Singh, B. Panesar, and S. Sharma, "Energy potential through agricultural biomass using geographical information system - a case study of Punjab," *Biomass and Bioenergy*, vol. 32, no. 4, pp. 301–307, 2008.

[21] R. Ahorsu, F. Medina, and M. Constanti, "Significance and challenges of biomass as a suitable feedstock for bioenergy and biochemical production: A review," *Energies*, vol. 11, p. 3366, 2018.

[22] B. Jiang, R. Tsao, Y. Li, and M. Miao, "Food safety: Food analysis technologies/techniques," in *Encyclopedia of Agriculture and Food Systems* (Neal K. Van Alfen, ed.), pp. 273–288, Oxford: Academic Press, 2014.

[23] Şebnem Yilmaz Balaman, "Chapter 1 - introduction to biomass-resources, production, harvesting, collection, and storage," in *Decision-Making for Biomass-Based Production Chains* (Şebnem Yilmaz Balaman, ed.), pp. 1–23, Academic Press, 2019.

[24] S. Deboosere, P. Van Meenen, D. Boetin, R. Sudrajat, and W. Verstroete, "Solid waste fermentation with particular emphasis on potentials for developing countries," *MIRCEN journal of applied microbiology and biotechnology*, vol. 4, no. 1, pp. 29–36, 1988.

[25] A. Juneja, D. Kumar, J. Williams, D. Wysocki, and G. Murthy, "Potential for ethanol production from conservation reserve program lands in oregon," *Journal of Renewable and Sustainable Energy*, vol. 3, 2011.

[26] W. Jin, K. Singh, J. Zondlo, J. Wang, and J. Singh Brar, "Pyrolysis kinetics of physical components of wood and wood-polymers using isoconversion method," vol. 3, 2012.

[27] P. Basu, *Biomass Gasification, Pyrolysis and Torrefaction: Practical Design and Theory*. Academic Press; Second edition, 2013.

[28] J. Blondeau and H. Jeanmart, "Biomass pyrolysis at high temperatures: Prediction of gaseous species yields from an anisotropic particle," *Biomass Bioenergy*, vol. 41, pp. 107–121, 2012.

[29] T. Faravelli, A. Frassoldati, G. Migliavacca, and E. Ranzi, "Detailed kinetic modeling of the thermal degradation of lignins," *Biomass and Bioenergy*, vol. 34, no. 3, pp. 290–301, 2010.

[30] M. Ioelovich, “Methods for determination of chemical composition of plant biomass,” *SITA*, vol. 17, pp. 208–214, 2015.

[31] K. Radotić and M. Micic, “Methods for extraction and purification of lignin and cellulose from plant tissues,” pp. 365–376, 2016.

[32] C. Heitner, D. Dimmel, and J. Schmidt, eds., *Lignin and Lignans*. Boca Raton: CRC Press, 2010.

[33] M. Z. H. Kazmi, A. Karmakar, V. K. Michaelis, and F. J. Williams, “Separation of cellulose/hemicellulose from lignin in white pine sawdust using boron trihalide reagents,” *Tetrahedron*, vol. 75, no. 11, pp. 1465 – 1470, 2019.

[34] A. Molino, V. Larocca, S. Chianese, and D. Musmarra, “Biofuels production by biomass gasification: A review,” *Energies*, vol. 11, no. 4, p. 811, 2018.

[35] R. M. Rowell, *Handbook of wood chemistry and wood composites*. CRC Press, Second edition, 2012.

[36] European Commission, “Phyllis database.” Available at https://phyllis.nl/, accessed on the 2019/10/08.

[37] A. Demirbas, “Effects of moisture and hydrogen content on the heating value of fuels,” *Energy Sources, Part A: Recovery, Utilization, and Environmental Effects*, vol. 29, no. 7, pp. 649–655, 2007.

[38] P. D. Osborn, “Section a - data charts and tables,” in *Handbook of Energy Data and Calculations* (P. D. Osborn, ed.), pp. 1–67, Butterworth-Heinemann, 1985.

[39] M. Hasan, Y. Haseli, and E. Karadogan, “Correlations to predict elemental compositions and heating value of torrefied biomass,” *Energies*, vol. 11, p. 2443, 2018.

[40] J. Shen, S. Zhu, X. Liu, H. Zhang, and J. Tan, “The prediction of elemental composition of biomass based on proximate analysis,” *Energy Conversion and Management*, vol. 51, no. 5, pp. 983–987, 2010.

[41] J. Parikh, S. Channiwala, and G. Ghosal, “A correlation for calculating elemental composition from proximate analysis of biomass materials,” *Fuel*, vol. 86, no. 12, pp. 1710–1719, 2007.

[42] D. Nhuchhen and P. Abdul Salam, "Estimation of higher heating value of biomass from proximate analysis: A new approach," *Fuel*, vol. 99, p. 5563, 2012.

[43] A. Demirbas, "Calculation of higher heating values of biomass fuels," *Fuel*, vol. 76, no. 5, pp. 431–434, 1997.

[44] A. K. Sharma, M. Ravi, and S. Kohli, "Modelling product composition in slow pyrolysis of wood," *SESI Journal*, vol. 16, no. 1, pp. 1–11, 2006.

[45] S. Chundawat, V. Balan, L. D. costa Sousa, and B. Dale, "2 - thermochemical pretreatment of lignocellulosic biomass," in *Bioalcohol Production* (K. Waldron, ed.), Woodhead Publishing Series in Energy, pp. 24–72, Woodhead Publishing, 2010.

[46] L. J. R. Nunes, J. C. D. O. Matias, and J. P. D. S. Catalo, "Chapter 2 - physical pretreatment of biomass," in *Torrefaction of Biomass for Energy Applications* (L. J. R. Nunes, J. C. D. O. Matias, and J. P. D. S. Catalo, eds.), pp. 45–88, Academic Press, 2018.

[47] A. Rentizelas, "Biomass storage," in *Biomass Supply Chains for Bioenergy and Biorefining* (J. B. Holm-Nielsen and E. A. Ehimen, eds.), pp. 127–146, Woodhead Publishing, 2016.

[48] J. D. McMillan, "Pretreatment of lignocellulosic biomass," ACS Publications, 1994.

[49] M. Alhwayzee, "Experimental investigation of the effects of some significant parameters on the pyrolysis of solid biomass materials," *IOP Conference Series: Materials Science and Engineering*, vol. 433, p. 012066, 2018.

[50] J. S. Tumuluru, "Effect of pellet diameter on density and durability of pellets made from high moisture woody and herbaceous biomass," *Carbon Resources Conversion*, vol. 1, no. 1, pp. 44–54, 2018.

[51] H. Chen and L. Wang, "Chapter 1 - introduction," in *Technologies for Biochemical Conversion of Biomass* (H. Chen and L. Wang, eds.), pp. 1–10, Oxford: Academic Press, 2017.

[52] J. C. E. Palacio, J. J. C. S. Santos, M. L. G. Renó, J. C. F. Júnior, M. Carvalho, A. M. M. Reyes, and D. J. R. Orozco, "Municipal solid waste management and energy recovery," in *Energy Conversion-Current Technologies and Future Trends*, IntechOpen, 2018.

[53] A. Papafilippaki, N. Paranychianakis, and N. P. Nikolaidis, "Effects of soil type and municipal solid waste compost as soil amendment on cichorium spinosum (spiny chicory) growth," *Scientia Horticulturae*, vol. 195, pp. 195–205, 2015.

[54] G. Fitzgerald, "Pre-processing and treatment of municipal solid waste (msw) prior to incineration," in *Waste to Energy Conversion Technology* (N. B. Klinghoffer and M. J. Castaldi, eds.), Woodhead Publishing Series in Energy, pp. 55–71, Woodhead Publishing, 2013.

[55] P. Manzanares, "8 - integrated hydrolysis, fermentation and co-fermentation of lignocellulosic biomass," in *Bioalcohol Production* (K. Waldron, ed.), Woodhead Publishing Series in Energy, pp. 205–223, Woodhead Publishing, 2010.

[56] A. Gollakota, N. Kishore, and S. Gu, "A review on hydrothermal liquefaction of biomass," *Renewable and Sustainable Energy Reviews*, vol. 81, pp. 1378–1392, 2018.

[57] A. Sharma, V. Pareek, and D. Zhang, "Biomass pyrolysisa review of modelling, process parameters and catalytic studies," *Renewable Sustainable Energy Rev.*, vol. 50, no. Supplement C, pp. 1081–1096, 2015.

[58] A. Bridgwater and G. Peacocke, "Fast pyrolysis processes for biomass," *Renewable and Sustainable Energy Reviews*, vol. 4, no. 1, pp. 1–73, 2000.

[59] T. Bridgwater, "Biomass pyrolysis, IEA bioenergy," tech. rep., Bioenergy research group, Aston University, UK, 2007.

[60] C. Guizani, M. Jeguirim, S. Valin, L. Limousy, and S. Salvador, "Biomass chars: The effects of pyrolysis conditions on their morphology, structure, chemical properties and reactivity," *Energies*, vol. 10, no. 6, 2017.

[61] Z. Wang, D. Shen, C. Wu, and S. Gu, "State-of-the-art on the production and application of carbon nanomaterials from biomass," *Green Chemistry*, vol. 20, pp. 5031–5057, 2018.

[62] J. W. Lee, B. Hawkins, D. M. Day, and D. C. Reicosky, "Sustainability: the capacity of smokeless biomass pyrolysis for energy production, global carbon capture and sequestration," *Energy Environ. Sci.*, vol. 3, pp. 1695–1705, 2010.

[63] T. Rizwan, A. Nahida, and A. Md. Shafiul, "Chapter 10 - biochars and biochar composites: Low-cost adsorbents for environmental remediation," *Biochar from Biomass and Waste*, pp. 169–209, 2019.

[64] Z. Chowdhury, K. Pal, W. Yehye, S. Suresh, S. T. Shah, A. Adebisi, E. Marliana, R. Rafique, and R. Johan, *Pyrolysis: A Sustainable Way to Generate Energy from Waste*. 2017.

[65] M. Jeguirim, A. A. Zorpas, J. N. Pedreno, L. Limousy, P. Loizia, M. Stylianou, and A. Agapiou, "Sustainability assessment for biomass-derived char production and applications," in *Char and Carbon Materials Derived from Biomass* (M. Jeguirim and L. Limousy, eds.), pp. 447–479, Elsevier, 2019.

[66] J. Deng, M. Li, and Y. Wang, "Biomass-derived carbon: synthesis and applications in energy storage and conversion," *Green Chemistry*, vol. 18, pp. 4824–4854, 2016.

[67] R. Khanna, K. Li, Z. Wang, M. Sun, J. Zhang, and P. S. Mukherjee, "11 - biochars in iron and steel industries," in *Char and Carbon Materials Derived from Biomass* (M. Jeguirim and L. Limousy, eds.), pp. 429–446, Elsevier, 2019.

[68] M. Zahid, E. Pervaiz, A. Hussain, M. Shahzad, and M. Niazi, "Synthesis of carbon nanomaterials from different pyrolysis techniques: A review," *Materials Research Express*, vol. 5, 2018.

[69] M. Jahirul, M. Rasul, A. Chowdhury, and N. Ashwath, "Biofuels production through biomass pyrolysis a technological review," *Energies*, vol. 5, pp. 4952–5001, 2012.

[70] S. Valin, J. Cances, P. Castelli, S. Thiery, A. Dufour, G. Boissonnet, and B. Spindler, "Upgrading biomass pyrolysis gas by conversion of methane at high temperature: Experiments and modelling," *Fuel*, vol. 88, no. 5, pp. 834–842, 2009.

[71] H. Lu, E. Ip, J. Scott, P. Foster, M. Vickers, and L. L. Baxter, "Effects of particle shape and size on devolatilization of biomass particle," *Fuel*, vol. 89, no. 5, pp. 1156–1168, 2010.

[72] G. M. Simmons and M. Gentry, "Particle size limitations due to heat transfer in determining pyrolysis kinetics of biomass," *Journal of Analytical and Applied Pyrolysis*, vol. 10, no. 2, pp. 117–127, 1986.

[73] A. Bridgwater, "Review of fast pyrolysis of biomass and product upgrading," *Biomass and Bioenergy*, vol. 38, pp. 68–94, 2012.

[74] P. Ahuja, S. Kumar, and P. C. Singh, "A model for primary and heterogeneous secondary reactions of wood pyrolysis," *Chemical Engineering & Technology*, vol. 19, no. 3, pp. 272–282, 1996.

[75] A. Demirbas and G. Arin, "An overview of biomass pyrolysis," *Energy Sources*, vol. 24, no. 5, pp. 471–482, 2002.

[76] O. Onay, "Influence of pyrolysis temperature and heating rate on the production of bio-oil and char from safflower seed by pyrolysis, using a well-swept fixed-bed reactor," *Fuel Processing Technology*, vol. 88, no. 5, pp. 523–531, 2007.

[77] A. Demirbas, "Effect of temperature on pyrolysis products from biomass," *Energy Sources*, vol. Part A, pp. 329–336, 2007.

[78] P. Fu, S. Hu, J. Xinag, L. Sun, T. Yang, A. Zhang, Y. Wang, and G. Chen, "Effects of pyrolysis temperature on characteristics of porosity in biomass chars," in *2009 International Conference on Energy and Environment Technology*, vol. 1, pp. 109–112, 2009.

[79] C. Koufopanos, A. Lucchesi, and G. Maschio, "Kinetic modelling of the pyrolysis of biomass and biomass components," *Can. J. Chem. Eng.*, vol. 67, no. 1, p. 9, 1989.

[80] S. Wang, X. Guo, K. Wang, and Z. Luo, "Influence of the interaction of components on the pyrolysis behavior of biomass," *Journal of Analytical and Applied Pyrolysis*, vol. 91, no. 1, pp. 183–189, 2011.

[81] P. Giudicianni, G. Cardone, G. Sorrentino, and R. Ragucci, "Hemicellulose, cellulose and lignin interactions on arundo donax steam assisted pyrolysis," *Journal of Analytical and Applied Pyrolysis*, vol. 110, no. Supplement C, pp. 138–146, 2014.

[82] J. Yu, N. Paterson, J. Blamey, and M. Millan, "Cellulose, xylan and lignin interactions during pyrolysis of lignocellulosic biomass," *Fuel*, vol. 191, no. Supplement C, pp. 140–149, 2017.

[83] A. Demirbas, "Effect of initial moisture content on the yields of oily products from pyrolysis of biomass," *Journal of Analytical and Applied Pyrolysis*, vol. 71, no. 2, pp. 803–815, 2004.

[84] C. Roy, H. Pakdel, and D. Brouillard, "The role of extractives during vacuum pyrolysis of wood," *Journal of Applied Polymer Science*, vol. 41, no. 12, pp. 337–348, 1990.

[85] C. Di Blasi, C. Branca, A. Santoro, and R. A. P. Bermudez, "Weight loss dynamics of wood chips under fast radiative heating," *Journal of Analytical and Applied Pyrolysis*, vol. 57, no. 1, pp. 77–90, 2001.

[86] T. Bridgwater, "Challenges and opportunities in fast pyrolysis of biomass: part I," *Johnson Matthey Technology Review*, vol. 62, no. 1, pp. 118–130, 2018.

[87] R. Karuppiah, A. Ganesh, and K. C. Khilart, "Influence of mineral matter on biomass pyrolysis characteristics," *Fuel*, vol. 74, pp. 1812–1822, 1995.

[88] Y. Cengel, "Heat transfer : A practical approach," 2003.

[89] A. Janse, R. Westerhout, and W. Prins, "Modelling of flash pyrolysis of a single wood particle," *Chemical Engineering and Processing: Process Intensification*, vol. 39, no. 3, pp. 239–252, 2000.

[90] A. Bridgwater, "Principles and practice of biomass fast pyrolysis processes for liquids," *Journal of Analytical and Applied Pyrolysis*, vol. 51, no. 1, pp. 3–22, 1999.

[91] A. Atreya, P. Olszewski, Y. Chen, and H. Baum, "The effect of size, shape and pyrolysis conditions on the thermal decomposition of wood particles and firebrands," *International Journal of Heat and Mass Transfer*, vol. 107, pp. 319–328, 2017.

[92] B. Babu and A. Chaurasia, "Heat transfer and kinetics in the pyrolysis of shrinking biomass particle," *Chemical Engineering Science*, vol. 59, no. 10, pp. 1999–2012, 2004.

[93] W. C. Park, A. Atreya, and H. Baum, "Experimental and theoretical investigation of heat and mass transfer processes during wood pyrolysis," *Combustion and Flame*, vol. 157, pp. 481–494, 2010.

[94] A. Khawam and D. R. Flanagan, "Solid-state kinetic models: basics and mathematical fundamentals," *J. Phys. Chem. B*, vol. 110, no. 35, pp. 17315–17328, 2006.

[95] R. Miller and J. Bellan, "A generalized biomass pyrolysis model based on superimposed cellulose, hemicellulose and lignin kinetics.," *Combustion Science and Technology*, vol. 126, no. 1, p. 40, 1997.

[96] G. Várhegyi, "Aims and methods in non-isothermal reaction kinetics," *Journal of Analytical and Applied Pyrolysis*, vol. 79, no. 1, pp. 278–288, 2007.

[97] M. M. Wright, D. E. Daugaard, J. A. Satrio, and R. C. Brown, "Techno-economic analysis of biomass fast pyrolysis to transportation fuels," *Fuel*, vol. 89, pp. S2 – S10, 2010.

[98] D. Carpenter, T. L. Westover, S. Czernik, and W. Jablonski, "Biomass feedstocks for renewable fuel production: a review of the impacts of feedstock and pretreatment on the yield and product distribution of fast pyrolysis bio-oils and vapors," *Green Chemistry*, vol. 16, pp. 384–406, 2014.

[99] G. Lyu, S. Wu, and H. Zhang, "Estimation and comparison of bio-oil components from different pyrolysis conditions," *Frontiers in Energy Research*, vol. 3, 2015.

[100] P. S. W. Lam, S. Sokhansanj, X. Bi, J. Lim, L. Naimi, M. Hoque, S. Mani, A. Ray Womac, X. Philip Ye, and S. Narayan, "Bulk density of wet and dry wheat straw and switchgrass particles," *Applied engineering in agriculture*, vol. 24, pp. 351–358, 2008.

[101] M. Amutio, G. Lopez, R. Aguado, J. Bilbao, and M. Olazar, "Biomass oxidative flash pyrolysis: Autothermal operation, yields and product properties," *Energy & Fuels*, vol. 26, no. 2, pp. 1353–1362, 2012.

[102] T. Martí-Rosselló, J. Li, and L. Lue, "Kinetic models for biomass pyrolysis.," *Archives of Industrial Biotechnology*, vol. 1, no. 1, 2016.

[103] C. Di Blasi, "Modeling chemical and physical processes of wood and biomass pyrolysis," *Prog. Energy Combust. Sci.*, vol. 34, no. 1, pp. 47–90, 2008.

[104] A. G. Bradbury, Y. Sakai, and F. Shafizadeh, "A kinetic model for pyrolysis of cellulose," *Journal of Applied Polymer Science*, vol. 23, no. 11, p. 9, 1979.

[105] T. Hosoya, H. Kawamoto, and S. Saka, "Cellulosehemicellulose and celluloselignin interactions in wood pyrolysis at gasification temperature," *Journal of Analytical and Applied Pyrolysis*, vol. 80, pp. 118–125, 2007.

[106] R. S. Miller, J. Bellan, I. I. Kinetics, J. B. An, J. Iyqmlsion, and G. Syqbols, "A generalized biomass pyrolysis model based on superimposed cellulose, hemicellulose and lignin kinetics," 1997.

[107] E. Ranzi, A. Cuoci, T. Faravelli, A. Frassoldati, G. Migliavacca, S. Pierucci, and S. Sommariva, "Chemical kinetics of biomass pyrolysis," *Energy Fuels*, vol. 22, no. 6, pp. 4292–4300, 2008.

[108] E. Ranzi, P. E. A. Debiagi, and A. Frassoldati, "Mathematical modeling of fast biomass pyrolysis and bio-oil formation. note i: Kinetic mechanism of biomass pyrolysis," *ACS Sustainable Chemistry & Engineering*, vol. 5, no. 4, pp. 2867–2881, 2017.

[109] X. Li, C. Sun, B. Zhou, and Y. He, "Determination of hemicellulose, cellulose and lignin in moso bamboo by near infrared spectroscopy," *Scientific Reports*, vol. 5, p. 17210, 2015.

[110] L. Burhenne, J. Messmer, T. Aicher, and M.-P. Laborie, "The effect of the biomass components lignin, cellulose and hemicellulose on {TGA} and fixed bed pyrolysis," *Journal of Analytical and Applied Pyrolysis*, vol. 101, pp. 177–184, 2013.

[111] M. Carrier, A. Loppinet-Serani, D. Denux, J.-M. Lasnier, F. Ham-Pichavant, F. Cansell, and C. Aymonier, "Thermogravimetric analysis as a new method to determine the lignocellulosic composition of biomass," *Biomass Bioenergy*, vol. 35, no. 1, pp. 298–307, 2010.

[112] V. Cozzani, A. Lucchesi, G. Stoppato, and G. Maschio, "A new method to determine the composition of biomass by thermogravimetric analysis.," *The Canadian Journal of Chemical Engineering*, vol. 75, no. 1, pp. 127–133, 1997.

[113] K. Singh, M. Risse, K. C. Das, and J. Worley, "Determination of composition of cellulose and lignin mixtures using thermogravimetric analysis," *Journal of Energy Resources Technology*, vol. 131, no. 2, 2007.

[114] T. Reed and A. Das, "Handbook of biomass downdraft gasifier engine system," tech. rep., 1987.

[115] T. Martí-Rosselló, J. Li, and L. Lue, "Quantitatively modelling kinetics through a visual analysis of the derivative thermogravimetric curves: Application to biomass pyrolysis," *Energy Conversion and Management*, vol. 172, pp. 296–305, 2018.

[116] S. Vyazovkin and D. Dollimore, "Linear and nonlinear procedures in isoconversional computations of the activation energy of nonisothermal reactions in solids," *Journal of Chemical Information and Computer Sciences*, vol. 36, no. 1, pp. 42–45, 1996.

[117] H. L. Friedman, "Kinetics of thermal degradation of char-forming plastics from thermogravimetry. application to a phenolic plastic," *Journal of Polymer Science Part C: Polymer Symposia*, vol. 6, no. 1, pp. 183–195, 1964.

[118] T. Ozawa, "A new method of analyzing thermogravimetric data," *Bulletin of the Chemical Society of Japan*, vol. 38, no. 11, pp. 1881–1886, 1965.

[119] J. H. Flynn and L. A. Wall, "A quick, direct method for the determination of activation energy from thermogravimetric data," *Journal of Polymer Science Part B: Polymer Letters*, vol. 4, no. 5, pp. 323–328, 1966.

[120] H. E. Kissinger, "Reaction kinetics in differential thermal analysis," *Analytical Chemistry*, vol. 29, no. 11, pp. 1702–1706, 1957.

[121] T. Akahira and T. Sunose, "Joint convention of four electrical institutes," *Materials Science and Applications*, vol. 16, 1971.

[122] A. W. Coats and J. P. Redfern, "Kinetic parameters from thermogravimetric data. ii.," *Journal of Polymer Science Part B: Polymer Letters*, vol. 3, no. 11, pp. 917–920, 1964.

[123] A. I. Ferreiro, M. Rabaal, and M. Costa, "A combined genetic algorithm and least squares fitting procedure for the estimation of the kinetic parameters of the pyrolysis of agricultural residues," *Energy Conversion and Management*, vol. 125, pp. 290–300, 2016.

[124] L. Xu, Y. Jiang, and L. Wang, "Thermal decomposition of rape straw: Pyrolysis modeling and kinetic study via particle swarm optimization," *Energy Conversion and Management*, vol. 146, pp. 124–133, 2017.

[125] D. W. Van Krevelen and K. Te Nijenhuis, *Properties of polymers: their correlation with chemical structure; their numerical estimation and prediction from additive group contributions*. Elsevier, 2009.

[126] H. E. Kissinger, "Variation of peak temperature with heating rate in differential thermal analysis," *Journal of Research of the National Bureau of Standards*, vol. 57, no. 4, pp. 217–221, 1956.

[127] S. Kim and J. K. Park, "Characterization of thermal reaction by peak temperature and height of dtg curves," *Thermochimica Acta*, vol. 264, pp. 137–156, 1995.

[128] S. Kim, E.-S. Jang, D.-H. Shin, and K.-H. Lee, "Using peak properties of a dtg curve to estimate the kinetic parameters of the pyrolysis reaction: application to high density polyethylene," *Polymer Degradation and Stability*, vol. 85, no. 2, pp. 799–805, 2004.

[129] D. Dollimore, T. Evans, Y. Lee, and F. Wilburn, "Correlation between the shape of a TG/DTG curve and the form of the kinetic mechanism which is applying," *Thermochimica Acta*, vol. 198, no. 2, pp. 249–257, 1992.

[130] J. Farjas and P. Roura, "Simple approximate analytical solution for nonisothermal singlestep transformations: Kinetic analysis," *AIChE Journal*, vol. 54, pp. 2145–2154, 2008.

[131] M. G. Grønli, G. Várhegyi, and C. Di Blasi, "Thermogravimetric analysis and devolatilization kinetics of wood," *Industrial & Engineering Chemistry Research*, vol. 41, no. 17, pp. 4201–4208, 2002.

[132] C. Branca, A. Albano, and C. Di Blasi, "Critical evaluation of global mechanisms of wood devolatilization," *Thermochim Acta*, vol. 429, no. 2, pp. 133–141, 2005.

[133] S. Vyazovkin, A. K. Burnham, J. M. Criado, L. A. Pérez-Maqueda, C. Popescu, and N. Sbirrazzuoli, "ICTAC kinetics committee recommendations for performing kinetic computations on thermal analysis data," *Thermochimica Acta*, vol. 520, no. 1, pp. 1–19, 2011.

[134] Y. Haseli, J. van Oijen, and L. de Goey, "Modeling biomass particle pyrolysis with temperature-dependent heat of reactions," *Journal of Analytical and Applied Pyrolysis*, vol. 90, no. 2, pp. 140–154, 2011.

[135] M. Corbetta, A. Frassoldati, H. Bennadji, K. Smith, M. J. Serapiglia, G. Gauthier, T. Melkior, E. Ranzi, and E. M. Fisher, "Pyrolysis of centimeter-scale woody biomass

particles: Kinetic modeling and experimental validation," *Energy & Fuels*, vol. 28, no. 6, pp. 3884–3898, 2014.

[136] A. Anca-Couce and N. Zobel, "Numerical analysis of a biomass pyrolysis particle model: Solution method optimized for the coupling to reactor models," *Fuel*, vol. 97, pp. 80–88, 2012.

[137] P. Nolan Ciesielski, M. Crowley, M. Nimlos, A. Sanders, G. M. Wiggins, D. J Robichaud, B. Donohoe, and T. Foust, "Biomass particle models with realistic morphology and resolved microstructure for simulations of intra-particle transport phenomena," *Energy & Fuels*, vol. 29, 2014.

[138] C. Ghabi, H. Benticha, and M. Sassi, "Two-dimensional computational modeling and simulation of wood particles pyrolysis in a fixed bed reactor," *Combustion Science and Technology*, vol. 180, no. 5, pp. 833–853, 2008.

[139] W. Wickramaarachchi and M. Narayana, "Pyrolysis of single biomass particle using three-dimensional computational fluid dynamics modelling," *Renewable Energy*, vol. 146, pp. 1153–1165, 2020.

[140] C. D. Blasi, "Modelling the fast pyrolysis of cellulosic particles in fluid-bed reactors," *Chemical Engineering Science*, vol. 55, no. 24, pp. 5999–6013, 2000.

[141] H. Bennadji, K. Smith, S. Shabangu, and E. Fisher, "Low-temperature pyrolysis of woody biomass in the thermally thick regime," *Energy & Fuels*, vol. 27, pp. 1453–1459, 2013.

[142] M. Newville, T. Stensitzki, D. B. Allen, and A. Ingargiola, "Lmfit: Non-linear least-square minimization and curve-fitting for python," 2014.

[143] K. Lan and J. W. Jorgenson, "A hybrid of exponential and gaussian functions as a simple model of asymmetric chromatographic peaks," *Journal of Chromatography A*, vol. 915, no. 1, pp. 1–13, 2001.

[144] M. J. Antal, G. Varhegyi, and E. Jakab, "Cellulose pyrolysis kinetics: revisited," *Industrial & Engineering Chemistry Research*, vol. 37, no. 4, pp. 1267–1275, 1998.

[145] J. López-Beceiro, A. Álvarez-García, T. Sebio-Puñal, S. Zaragoza-Fernández, B. Álvarez-García, A. Díaz-Díaz, J. Janeiro, and R. Artiaga, "Kinetics of thermal degradation of cellulose: Analysis based on isothermal and linear heating data," *BioResources*, vol. 11, no. 3, 2016.

[146] C. Haixiang, L. Naian, and Z. Weitao, "Critical study on the identification of reaction mechanism by the shape of TG/DTG curves," *Solid State Sciences*, vol. 12, no. 4, pp. 455–460, 2010.

[147] R. L. Blaine and H. E. Kissinger, "Homer Kissinger and the Kissinger equation," *Thermochimica Acta*, vol. 540, pp. 1–6, 2012.

[148] B. Cagnon, X. Py, A. Guillot, F. Stoeckli, and G. Chambat, "Contributions of hemicellulose, cellulose and lignin to the mass and the porous properties of chars and steam activated carbons from various lignocellulosic precursors," *Bioresource Technology*, vol. 100, no. 1, pp. 292–298, 2009.

[149] H. Zhou, Y. Long, A. Meng, S. Chen, Q. Li, and Y. Zhang, "A novel method for kinetics analysis of pyrolysis of hemicellulose, cellulose, and lignin in TGA and macro-TGA," *RSC Advances*, vol. 5, no. 34, pp. 26509–26516, 2015.

[150] Y.-C. Lin, J. Cho, G. A. Tompsett, P. R. Westmoreland, and G. W. Huber, "Kinetics and mechanism of cellulose pyrolysis," *Journal of Physical Chemistry C*, vol. 113, no. 46, pp. 20097–20107, 2009.

[151] S. Wang, Q. Liu, K. Wang, X. Guo, Z. Luo, K. Cen, and T. Fransson, "Study on catalytic pyrolysis of manchurian ash for production of bio-oil," *International Journal of Green Energy*, vol. 7, no. 3, pp. 300–309, 2010.

[152] K. M. Isa, S. Daud, N. Hamidin, K. Ismail, S. A. Saad, and F. H. Kasim, "Thermogravimetric analysis and the optimisation of bio-oil yield from fixed-bed pyrolysis of rice husk using response surface methodology (rsm)," *Industrial Crops and Products*, vol. 33, no. 2, pp. 481–487, 2011.

[153] S. Wang, Q. Liu, Z. Luo, L. Wen, and K. Cen, "Mechanism study on cellulose pyrolysis using thermogravimetric analysis coupled with infrared spectroscopy," *Frontiers of Energy and Power Engineering in China*, vol. 1, no. 4, pp. 413–419, 2007.

[154] T. Xavier, T. Lira, M. Schettino Jr, and M. Barrozo, "A study of pyrolysis of macadamia nut shell: Parametric sensitivity analysis of the ipr model," *Brazilian Journal of Chemical Engineering*, vol. 33, no. 1, pp. 115–122, 2016.

[155] M. Antal, S. G. Allen, X. Dai, B. Shimizu, M. S. Tam, and M. Grønli, "Attainment of the theoretical yield of carbon from biomass," *Industrial and Engineering Chemistry Research*, vol. 39, pp. 4024–4031, 2000.

[156] Agripellets Ltd. Minerva Mill, Station Road, Alcester, B495ET.

[157] I. Barmina, R. Valdmanis, and M. Zake, "The effects of biomass co-gasification and co-firing on the development of combustion dynamics," *Energy*, vol. 146, pp. 4–12, 2018.

[158] S. A. El-Sayed and M. Khairy, "An experimental study of combustion and emissions of wheat straw pellets in high-temperature air flows," *Combustion Science and Technology*, vol. 190, no. 2, pp. 222–251, 2018.

[159] G. Várhegyi, Z. Sebestyén, Z. Czégény, F. Lezsovits, and S. Könczöl, "Combustion kinetics of biomass materials in the kinetic regime," *Energy & Fuels*, vol. 26, no. 2, pp. 1323–1335, 2012.

[160] M. Bains and L. Robinson, "Material comparators for end-of-waste decisions," tech. rep., Environment Agency, 2016.

[161] O. Karlström, A. Brink, and M. Hupa, "Biomass char nitrogen oxidation - single particle model," *Energy & Fuels*, vol. 27, pp. 1410–1418, 2013.

[162] O. Karlström, A. Brink, and M. Hupa, "Desorption kinetics of CO in char oxidation and gasification in O_2, CO_2 and H_2O," *Combustion and Flame*, vol. 162, 2014.

[163] M. Bellais, *Modelling of the pyrolysis of large wood particles*. PhD thesis, KTH, Chemical Engineering and Technology, 2007.

[164] B. Babu and A. Chaurasia, "Modeling & simulation of pyrolysis: influence of particle size and temperature," in *Proceedings of International Conference on Multimedia and Design*, vol. 4, pp. 103–128, Citeseer, 2002.

[165] N. Liu, W. Fan, R. Dobashi, and L. Huang, “Kinetic modeling of thermal decomposition of natural cellulosic materials in air atmosphere,” *Journal of Analytical and Applied Pyrolysis*, vol. 63, no. 2, pp. 303–325, 2002.

[166] M. Momeni, C. Yin, S. Kr, T. Hansen, P. Jensen, and P. Glarborg, “Experimental study on effects of particle shape and operating conditions on combustion characteristics of single biomass particles,” *Energy & Fuels*, vol. 27, pp. 507–514, 2013.

[167] S. Zhao, Y. Luo, Y. Su, Y. Zhang, and Y. Long, “Experimental investigation of the oxidative pyrolysis mechanism of pinewood on a fixed-bed reactor,” *Energy & Fuels*, vol. 28, pp. 5049–5056, 2014.

[168] D. Shen, J. Ye, R. Xiao, and h. zhang, “Tg-ms analysis for thermal decomposition of cellulose under different atmospheres,” *Carbohydrate polymers*, vol. 98, pp. 514–21, 2013.

[169] D. Shen, L. Zhang, J. Xue, S. Guan, Q. Liu, and R. Xiao, “Thermal degradation of xylan-based hemicellulose under oxidative atmosphere,” *Carbohydrate Polymers*, vol. 127, pp. 363–371, 2015.

[170] M. Amutio, G. Lopez, R. Aguado, M. Artetxe, J. Bilbao, and M. Olazar, “Kinetic study of lignocellulosic biomass oxidative pyrolysis,” *Fuel*, vol. 95, pp. 305–311, 2012.

[171] H. Watanabe, Y. Morinaga, T. Okada, and K. Okazaki, “Experimental and numerical investigation of biomass pyrolysis process focusing on intra-particle heat transfer,” *14th International Heat Transfer Conference*, vol. 3, no. 49385, pp. 161–168, 2010.

[172] C. Gómez, F. Barontini, V. Cozzani, and E. Velo, “Influence of secondary reactions on the heat of pyrolysis of biomass,” *Industrial & Engineering Chemistry Research*, vol. 48, pp. 10222–10233, 2009.

[173] Q. Chen, R. Yang, B. Zhao, Y. Li, S. Wang, H. Wu, Y. Zhuo, and C. Chen, “Investigation of heat of biomass pyrolysis and secondary reactions by simultaneous thermogravimetry and differential scanning calorimetry,” *Fuel*, vol. 134, pp. 467–476, 2014.

[174] L. Duan, C. Zhao, W. Zhou, C. Qu, and X. Chen, “Investigation on coal pyrolysis in co2 atmosphere,” *Energy and Fuels*, vol. 23, pp. 3823–3830, 2009.

[175] E. E. Kwon, Y. J. Jeon, and H. Yi, "New candidate for biofuel feedstock beyond terrestrial biomass for thermo-chemical process (pyrolysis/gasification) enhanced by carbon dioxide (co2)," *Bioresource Technology*, vol. 123, pp. 673–677, 2012.

[176] J. Hunt, A. Ferrari, A. Lita, M. Crosswhite, B. Ashley, and A. E. Stiegman, "Microwave-specific enhancement of the carboncarbon dioxide (boudouard) reaction," *The Journal of Physical Chemistry C*, vol. 117, no. 51, pp. 26871–26880, 2013.

[177] M. Lanzetta and C. D. Blasi, "Pyrolysis kinetics of wheat and corn straw," *Journal of Analytical and Applied Pyrolysis*, vol. 44, no. 2, pp. 181–192, 1998.

[178] M. G. Grønli and M. C. Melaaen, "Mathematical model for wood pyrolysis comparison of experimental measurements with model predictions," *Energy & Fuels*, vol. 14, no. 4, pp. 791–800, 2000.

[179] S. Churchill and M. Bernstein, "A correlating equation for forced convection from gases and liquids to a circular cylinder in crossflow," *Journal of Heat Transfer*, vol. 99, no. 2, pp. 300–306, 1977.

[180] E. J. Kansa, H. E. Perlee, and R. F. Chaiken, "Mathematical model of wood pyrolysis including internal forced convection," *Combustion and Flame*, vol. 29, pp. 311–324, 1977.

[181] C. K. Lee, R. F. Chaiken, and J. M. Singer, "Charring pyrolysis of wood in fires by laser simulation," *Symposium (International) on Combustion*, vol. 16, no. 1, pp. 1459–1470, 1977.

[182] D. Lu, L. Tabil, D. Wang, and G. Wang, "Manufacturing wheat straw pellet with wood waste and binders," *CSBE/SCGAB Annual Conference*, 2013.

[183] P. Mason, L. Darvell, J. Jones, and A. Williams, "Comparative study of the thermal conductivity of solid biomass fuels," *Energy & Fuels*, vol. 30, pp. 2158–2163, 2016.

[184] R. Bilbao, A. Millera, and M. B. Murillo, "Temperature profiles and weight loss in the thermal decomposition of large spherical wood particles," *Industrial & Engineering Chemistry Research*, vol. 32, no. 9, pp. 1811–1817, 1993.

[185] W. F. Ramirez in *Computational Methods in Process Simulation (Second Edition)*, p. iv, Oxford: Butterworth-Heinemann, second edition ed., 1997.

[186] M. S. Alnæs, J. Blechta, J. Hake, A. Johansson, B. Kehlet, A. Logg, C. Richardson, J. Ring, M. E. Rognes, and G. N. Wells, "The FEniCS project version 1.5," *Archive of Numerical Software*, vol. 3, no. 100, 2015.

[187] R. Bird, Byron, W. E. Stewart, and E. N. Lightfoot, *Transport Phenomena*. John Wiley & Sons, 1960.

[188] A. N. Brooks and T. J. Hughes, "Streamline upwind/petrov-galerkin formulations for convection dominated flows with particular emphasis on the incompressible navier-stokes equations," *Computer Methods in Applied Mechanics and Engineering*, vol. 32, no. 1, pp. 199–259, 1982.

[189] T. Tezduyar, "Stabilization parameters and local length scales in SUPG and PSPG formulations," *Proceedings of the Fifth World Congress on Computational Mechanics*, pp. 1–17, 2002.

[190] M. M. Faris, P. S. Jensen, K. Dam-Johansen, R. R. Ali, and R. M. Kasmani, "Influence of reaction temperature and water content on wheat straw pyrolysis," in *International Journal of Chemical, Molecular, Nuclear, Materials and Metallurgical Engineering*, vol. 6, pp. 919–925, 2012.

[191] C. Di Blasi and C. Branca, "Kinetics of primary product formation from wood pyrolysis," *Industrial & Engineering Chemistry Research*, vol. 40, no. 23, pp. 5547–5556, 2001.

[192] M. Calonaci, R. Grana, E. Barker Hemings, G. Bozzano, M. Dente, and E. Ranzi, "Comprehensive kinetic modeling study of bio−oil formation from fast pyrolysis of biomass," *Energy Fuels*, vol. 24, no. 10, pp. 5727–5734, 2010.

[193] A. Vyas, T. Chellappa, and J. L. Goldfarb, "Porosity development and reactivity changes of coalbiomass blends during co-pyrolysis at various temperatures," *Journal of Analytical and Applied Pyrolysis*, vol. 124, pp. 79–88, 2017.

[194] P. Fu, X. Bai, W. Yi, Z. Li, and Y. Li, "Fast pyrolysis of wheat straw in a dual concentric rotary cylinder reactor with ceramic balls as recirculated heat carrier," *Energy Conversion and Management*, vol. 171, pp. 855–862, 2018.

[195] F. Ates, S. Tophanecioglu, and A. E. Putun, "The evaluation of mesoporous materials as catalyst in fast pyrolysis of wheat straw," *International Journal of Green Energy*, vol. 12, no. 1, pp. 57–64, 2015.

[196] M. Z. Farooq, M. Zeeshan, S. Iqbal, N. Ahmed, and S. Asfand Yar Shah, "Influence of waste tire addition on wheat straw pyrolysis yield and oil quality," *Energy*, vol. 144, pp. 200–206, 2017.

[197] A. Aqsha, M. Tijani, B. Moghtaderi, and N. Mahinpey, "Catalytic pyrolysis of straw biomasses (wheat, flax, oat and barley) and the comparison of their product yields," *Journal of Analytical and Applied Pyrolysis*, vol. 125, pp. 201–208, 2017.

[198] S. Cheng, L. Wei, X. Zhao, Y. Huang, D. Raynie, C. Qiu, J. Kiratu, and Y. Yu, "Directly catalytic upgrading bio-oil vapor produced by prairie cordgrass pyrolysis over ni/hzsm-5 using a two stage reactor," *AIMS Energy*, vol. 3, pp. 227–240, 2015.